6-1-2014

Biophysical Characterization of the vOTU Proteases from the CCHF and Dugbe Nairoviruses

Glenn C. Capodagli
University of Denver

BIOPHYSICAL CHARACTERIZATION OF THE vOTU PROTEASES FROM THE CCHF AND DUGBE NAIROVIRUSES

A Dissertation

Presented to

the Faculty of Natural Sciences and Mathematics

University of Denver

In Partial Fulfillment

of the Requirements for the Degree

Doctor of Philosophy

by

Glenn C. Capodagli

June 2014

Advisor: Scott D. Pegan

Author: Glenn C. Capodagli
Title: BIOPHYSICAL CHARACTERIZATION OF THE vOTU PROTEASES FROM THE CCHF AND DUGBE NAIROVIRUSES
Advisor: Scott D. Pegan
Degree Date: June 2014

Abstract

My research focuses on understanding the substrate specificity of the viral homolog of the ovarian tumor domain protease superfamily (vOTU) from nairoviruses, and the structural reasons for their specificities. The vOTU from the Crimean-Congo Hemorrhagic Fever Virus (CCHFV) has been implicated in the down-regulation of the innate immune response through its ability to cleave post-translational modifications via Ubiquitin (Ub) as well as the Ub-like interferon-stimulated gene 15 (ISG15). vOTU homologs have been found in numerous viruses across several families. Moreover, the effects of these viruses range in severity from mild flu-like symptoms to mortality depending on the species of the infected host. As such, several nairovirus vOTUs including those from the Dugbe Virus (DUGV), Erve Virus (ERVEV), and CCHFV were subjected to enzymological studies to gain insight into substrate specificity. These studies revealed that even vOTUs from the same viral family have differing specificities for Ub and ISG15. Furthermore, these preferences extend to include the different polymeric moieties of Ub. In order to gain insight into any structural reasoning for these substrate predilections, the X-ray crystal structures of the vOTUs from both CCHFV and DUGV were each solved covalently bound with Ub. These structures exposed unique secondary structure elements compared to other members of the OTU superfamily that offer understanding into why certain vOTUs, such as that from CCHFV, can possess robust activity for Ub and ISG15. Likewise, the crystallographic data point to the primary

structure of the vOTUs as the main driving force for divergence between nairovirus vOTU specificity.

Acknowledgements

First, I would like to thank Dr. Scott Pegan for his guidance and support of both my research and my well being over the years. Without him I would not have been a part of the inaugural class for the University of Denver's Molecular and Cellular Biophysics PhD program. I would also like to thank all of the undergraduate researchers who have worked with me over the last four years. Their efforts often went above and beyond what was expected, as demonstrated by their co-authorships on each of my papers. Also, I would like to thank all of my fellow graduate students for their support and camaraderie through the trials and tribulations that come with pursuing a PhD. In particular my labmate Michelle Deaton, who has been a great sounding board for both my experiments and frustrations.

Beyond those at the University of Denver I would like to thank my friends and family for believing in me and encouraging me throughout the years. Especially my mother and father Janet and Philip who have sustained every endeavor of mine with love and guidance. I would also like to thank Drs. Aimee Eggler and Andrew Mesecar without whom I would not have gained the preliminary experience in research necessary for my success as a graduate student.

Table of Contents

List Of Figures

List of Abbreviations

ALS – Advanced Light Source

AMC – 7-amino-4-methylcourmarin

APBS – Adaptive Poisson-Boltzmann Solver

ASLV – Avian sarcoma leucosis virus

BSA – Bovine Serum Albumin

CCD – Charge-Coupled Device

CCHF – Crimean-Congo Hemorrhagic Fever

CCHF vOTU – the viral Ovarian Tumor Domain Protease from the Crimean-Congo Hemorrhagic Fever Virus

CCHF vOTU-Ub – the viral Ovarian Tumor Domain Protease from the Crimean-Congo Hemorrhagic Fever Virus bound to Ub

CCHFV – Crimean-Congo Hemorrhagic Fever Virus

CCP4 – Collaborative Computational Project No. 4

DHAP – Dihydroxyacetone Phosphate

DMSO – Dimethyl Sulfoxide

DOTS – Directly Observed Therapy, Short Course

DSSP – Defined Secondary Structure of Proteins

DTT - Dithiothreitol

DUB – Deubiquitinating Enzyme

DUG – Dugbe

DUG vOTU – the viral Ovarian Tumor Domain Protease from the DugbeVirus

DUG vOTU-Ub - the viral Ovarian Tumor Domain Protease from the Dugbe Virus bound to Ub

DUGV – Dugbe Virus

E. coli – Escherichia coli

E1 – Ubiquitin Activating Enzyme

E2 – Ubiquitin Conjugating Enzyme

E3 – Ubiquitin Ligating Enzyme

EcFBA – Escherichia coli class II fructose 1,6-bisphosphate aldolase

ERVEV – Erve Virus

FBA – fructose 1,6-bisphosphate aldolase

FBP – Fructose 1,6-bisphosphate

FRET – Förster Resonance Energy Transfer

G3P – Glyceraldehyde 3-phosphate

GANV – Ganjam Virus

GAPDH – Glyceraldehyde 3-phosphate Dehydrogenase

H – Hydrogen

HCA – 8-hydroxyquinoline-2-carboxylic acid

HEPES - 4-(2-hydroxyethyl)-1-piperazineethanesulfonic acid

hISG15 – human Interferon Stimulated Gene product 15

Holo-MtFBA – Mycobacterium tuberculosis class II fructose 1,6-bisphosphate aldolase with zinc (II)-bound but substrate-less

hOTUB2 – human Otubain 2

HySS – Hybrid Substructure Search

IFA – Immunofluorescence Assay

IFN – interferon

IFN-α/β – alpha/beta interferon

IPTG – isopropyl-β-D-thiogalactopyranoside

ISG – Interferon Stimulated Gene

ISG15 – Interferon-stimulated gene product 15

ITC – Isothermal Titration Calorimetry

JAK1-Stat1/2 – Janus-activated kinase 1–signal transducer and activator of transcription 1/2

JAMM – JAB1/MPN/MOV34

K – Lysine

L – Large

LB – Luria-Bertani

M – Medium

MDR-TB – Multidrug-resistant Tuberculosis

MEK1 – MAP kinase kinase 1

MESNA – sodium 2-mercaptoethansulfonate

MIC – Minimal Inhibitory Concentration

MRSA – Methicillin-Resistant Staphylococcus aureus

MtFBA – Mycobacterium tuberculosis class II fructose 1,6-bisphosphate aldolase

MtFBA-HCA – Mycobacterium tuberculosis class II fructose 1,6-bisphosphate aldolase with HCA bound

MtTPI – Mycobacterium tuberculosis Triosephosphate Isomerase

MW – Molecular Weight

MxA – Myxovirus-resistant protein A

NAD+ – Nicotinamide Adenine Dinucleotide

NADH – Reduced Nicotinamide Adenine Dinucleotide

NEDD8 – Neural precursor cell Expressed, Developmentally Downregulated 8)

NSDV – Nairobi Sheep Disease Virus

NTA – Ni-nitrilotriacetic Acid

OTU – Ovarian Tumor domain protease

OTUB1/2 – Otubain 1/2

PCR – Polymerase Chain Reaction

PDB – Protein Databank

PEG I – Polyethylene glycol 1

PGH – Phosphoglycolohydroxamate

PKR – Protein Kinase Receptor

PLpro – Papain-Like protease

Poly-Ub – Polymeric Ubiquitin

PRRSV – Porcine Reproductive and Respiratory Virus

RdRp – RNA-dependent RNA polymerase

RIG-I – Retinoic acid-Inducible Gene 1

RSV – Rice Stripe Virus

S – Small

SAD – Single-wavelength Anomalous Dispersion

SaFBA – Staphylococcus aureus class II fructose 1,6-bisphosphate aldolase

SARS – Severe Acute Respiratory Syndrome

SDS-PAGE – sodium dodecyl sulfate-polyacrylamide gel electrophoresis

Se-Met – Selenomethionyl

ssRNA (-) – negative-sense, single-stranded RNA Virus

ssRNA (+) – positive-sense, single-stranded RNA Virus

TB – Tuberculosis

TRAF – Tumor necrosis factor Receptor Associated Factor

TYM vOTU – the viral Ovarian Tumor Domain Protease from the Turnip Yellow Mosaic Virus

TYMV – Turnip Yellow Mosaic Virus

Ub – Ubiquitin

UBL – Ubiquitin-Like

UCH – C-terminal hydrolase

USP – Ubiquitin-Specific Protease

vOTU – viral Ovarian Tumor domain protease

WHO – World Health Organization

wt – wild-type

XDR-TB – Extensively drug-resistant Tuberculosis

yOTU1 – yeast Ovarian Tumor 1

Z-loop – Zinc Binding Loop

SECTION I

Chapter One: Introduction

Deubiquitinating enzymes (DUBs) are responsible for the removal of Ubiquitin (Ub), an important post-translational modifying protein, from its substrate. Ub is a small protein, 76 residues in length, which acts as a cellular signal through post-translational attachment to a target protein, and is responsible for a range of activity from trafficking and cell division to upregulation and degradation. DUBs can not only edit and remove Ub but also Ub-like molecules; those that assume a similar fold to that of Ub and can also act as cellular signals. In this chapter I will give a brief overview of: the known functions of Ub and a few Ub-like proteins, the five superfamilies of DUBs and what is known of their roles in the Ub cycle, a synopsis of the DUB subclass known as the viral ovarian tumor domain proteases (vOTUs), and a brief background of viruses from several different families that have been found to possess a vOTU.

Roles of Ubiquitin.

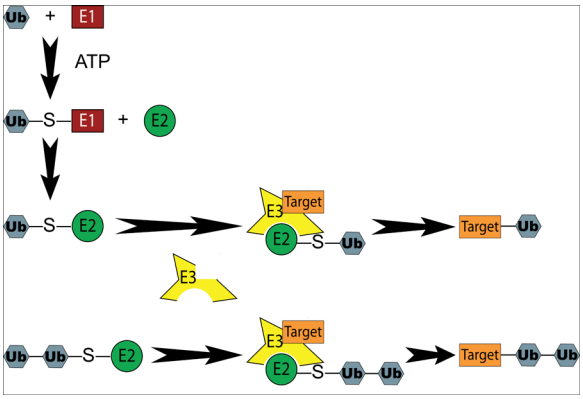

Figure 1.1. Ubiquitin Conjugation Cascade.

Ubiquitin (Ub) is a small, highly conserved, 76 amino acid protein. Ub is attached as a post-translational modification through a three-step enzymatic process. Ubiquitination relies on a cascade of enzymes by which Ub is activated (E1),

conjugated (E2), and finally ligated (E3) to its intended target (Figure 1.1)[8-10]. During activation the E1 enzyme utilizes ATP to create a thioester bond between the C-terminus of the Ub and a cysteine on the E1. From there the Ub is transferred to the active site cysteine of the E2. After that the Ub is attached to the ε-amino group of a lysine residue (K) located on the target protein via the E3. In humans there are over 600 E3 enzymes, 38 E2 enzymes, and 2 E1 enzymes.

Ubiquitination is further complicated by the fact that Ub itself can be ubiquitinated at its N-terminus (linear) or at one of its seven lysines (6, 11, 27, 29, 33, 48, or 63). Furthermore, chains consisting of more than one type of linkage (mixed) also exist (Figure 1.2). Modification with a single Ub moiety (Mono-Ub; Figure 1.2a) has been linked to DNA repair, gene expression, and endocytosis[11-14]. Attachment of several mono-Ub proteins to the same target is known as multimonomeric Ub (multimono-Ub; Figure 1.2b) and has also been implicated in endocytosis[15]. In the case of polymeric-Ub chains (poly-Ub), the protein's fate is determined by the type of Ub-linkage present (Figure 1.2 c-e). A poly-Ub chain is designated by the lysine residue that is the site of attachment for each subsequent Ub protein. For example, K63-linked poly-Ub indicates that each Ub is attached to lysine 63 of the Ub molecule before it. These chains can be homogenous or mixed, containing linkages at several different lysine residues. Each unique

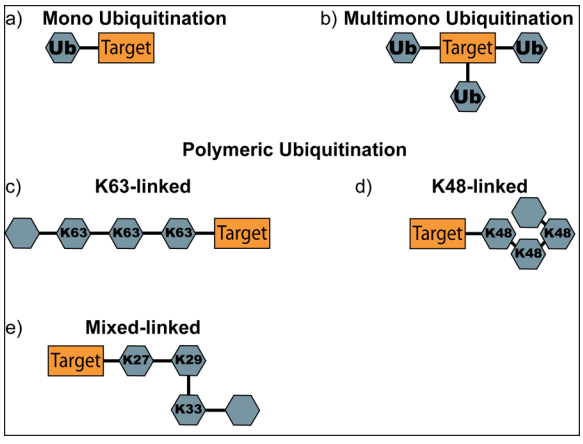

Figure 1.2. Different conformations of Ub modification.

linkage type results in its own unique conformation, which in turn exposes different residues and areas for proteins such as DUBs to interact[16].

Noncanonical forms of poly-Ub—linear and K6, -11, -27, -29, and -33—comprise over half of all poly-Ub-conjugated yeast proteins and have been implicated in immune system regulation and other key cellular functions[17]. Specifically, K29-linked poly-Ub is known to facilitate trafficking proteins to the lysosome, whereas K11-linked poly-Ub has been implicated in regulating cell division[18]. Although their functions have been less studied, K6, K27, and K33 appear to possibly act as modulators of immunologically relevant signaling pathways[19-21]. Unlike the noncanonical linked poly-Ub, the effects of K48-linked and K63-linked poly-Ub modifications are better studied. Modification of host proteins by K48-linked poly-Ub typically leads to proteasomal degradation, whereas K63-linked poly-Ub modifications are implicated in the induction of the type I interferon (IFN) response involved in the innate immune response[22, 23]. Upon entry into host cells, viruses need to outpace innate immunity before the adaptive immune system clears them from the organism. The type I IFN-α/β are critical orchestrators of innate immunity[24]. Previously, a phosphorylation cascade was proposed to singularly instigate the production of type I IFNs and proinflammatory cytokines (NF-κB) and the type I IFN upregulation of several IFN-stimulated gene with antipathogenic properties through JAK1-STAT1/2 signaling (Janus-activated kinase 1–signal transducer and activator of transcription 1/2)[25]. However, regulation of the IFNI response and activation of NF-κB has been shown to go beyond phosphorylation events and also relies on post-translational modification by Ub and Ub-like IFN-stimulated gene product 15 (ISG15)[26]. In

particular, JAK1, STAT1/2, TRAF (Tumor necrosis factor Receptor-Associated Factor), and RIG-I (retinoic acid-inducible gene 1), among other IFNI signaling and effector proteins, have been observed to undergo ubiquitination or ISGylation[27].

Ub-Like Proteins

Ub-like (UBL) proteins are proteins that have a similar fold to that of Ub and also act as post-translational modifiers typically through attachment via lysines. Two examples of UBL proteins are ISG15 and neural precursor cell expressed, developmentally downregulated 8 (NEDD8). ISG15 is a UBL protein almost twice as large as Ub and as such adopts a secondary structure comprised of two domains that each shares roughly 30% structural homology to that of Ub. Unlike Ub, ISG15 is not as well conserved throughout eukaryotes[28]. Beyond the previously mentioned role of ISG15 in the IFNI response, ISG15 has been shown to be critical for antiviral activity through several means including acting as a Ub antagonist in HIV-1 and Ebola to prevent budding, and disruption of the endosomal sorting complexes required for transport (ESCRT) pathway in the Avian sarcoma leucosis virus (ASLV)[28]. Similarly, NEDD8 is a UBL protein involved in the activity of the cullin-RING ligase family of E3 ligases, impairment of which has been tied to cancer[29]. NEDD 8 is more similar to Ub than ISG15 being 81 amino acids in length in its proform and sharing ~80% sequence homology[30]. Just as Ub conjugation involves a cascade of E1-E2-E3 enzymes, so too does UBL conjugation with each UBL requiring their own specific set of enzymes.

DUB Superfamilies.

DUBs can be classified into five families: Ubiquitin-specific proteases (USPs), Josephins, JAB1/MPN/MOV34 metalloenzymes (JAMMs), C-terminal hydrolases (UCHs), and ovarian tumor proteases (OTUs). Each DUB has their own substrate

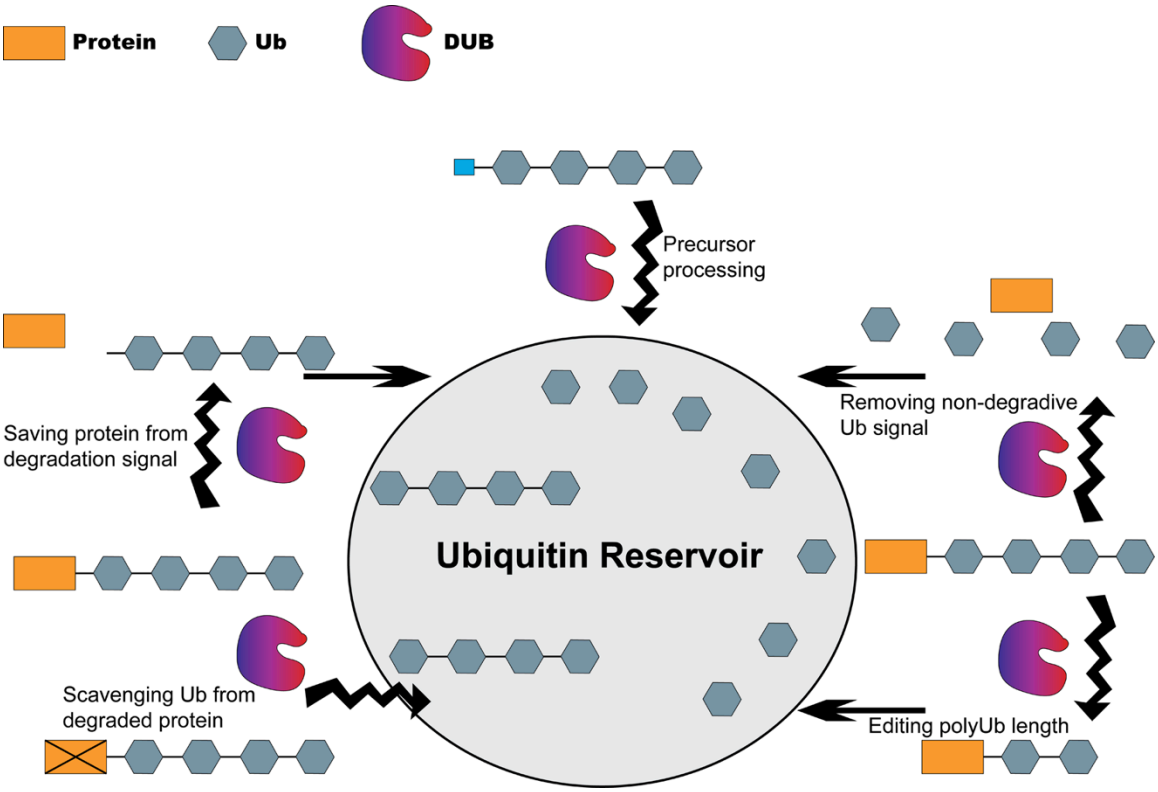

Figure 1.3. Functions of DUBs

preference and their role can be separated into three major categories: 1.) Generation of free Ub from a transcribed linear fusion of multiple Ub molecules, 2.) Removal of Ub from post-translationally modified proteins, or 3.) Editing the length of poly-Ub chains (Figure 1.3)[16].

Members of the UCH superfamily, such as UCH-L1 and L3, have shown the ability to only cleave mono-Ub, however, other members such as UCH37 can also cleave

poly-Ub[31]. USPs make up the largest family of DUBs with over 50 found in humans and have previously been shown to preferentially cleave Ub-modified substrates, with each member having their own linkage preferences. However, recently USP18 has shown to preferentially cleave ISG15-conjugated substrates over Ub[32-34]. ATAXIN-3, a Josephin DUB, has been shown to effectively trim Ub from K63-linked poly-Ub when the chain length was greater than five Ub molecules suggesting a dependence on length, and demonstrates increased cleavge of shorter, mixed chains for K63 linkages in both homogenous and mixed chains[35]. Most JAMM domain DUBs are specific for K63-linked poly-Ub and can cleave complete poly-Ub chains from their substrate[36]. The OTU superfamily members can be divided into three subclasses according to their sequence homology, otubains, A20-like OTUs, and ubiquitin thioesterase ZRANB1[16]. Otubain1/2 (OTUB1/2) plays a key role in T cell response and prefers K48-linked poly-Ub or NEDD8 as a substrate[37]. A20 and A20-like Cezanne OTU proteases are negative regulators of the NF-κB-mediated inflammation response, selectively cleaving K63-linked poly-Ub targets. DUBA also shows preference for K63-linked poly-Ub[38]. Predominantly, OTU proteases have been linked to Ub removal and/or remodeling of Ub-conjugated proteins, placing them among five protease superfamilies that facilitate signal transduction cascades and play key roles in protein stability[16].

Viral Ovarian Tumor Domain (vOTU) Proteases.

The most recent protease to be identified as an OTU was the viral ovarian tumor domain (vOTU) protease, co-located with the RNA-dependent RNA polymerase (RdRp) in the large (L) protein of the Crimean-Congo Hemorrhagic Fever (CCHF) virus[39].

Interestingly, as CCHF is a negative-sense, single-stranded RNA virus [ssRNA (-)], no protease is required to cleave a viral polypeptide to facilitate viral replication, as is the case in positive-sense ssRNA [ssRNA (+)] viruses. Furthermore, recent reports have observed that vOTU is not required for RdRp activity and that vOTU protease activity has been linked to impairment of the type I IFN response through its deubiquitinating and deISGylating activity[39, 40]. Additional studies have also tentatively identified the presence of vOTU homologs in ssRNA (+) viruses such as the *Arterivirus* genus of the *Arteriviridae* family, suggesting that they too may facilitate impairment of the type I IFN response. vOTUs are unique in that they are the only OTU to have shown both deubiquitinating and deISGylating activity[39]. In attempts to better understand the OTU superfamily, structures of OTUB and A20-like OTU domains have been elucidated[37, 41, 42]. An X-ray structure of the yeast ovarian tumor 1 (yOTU1) domain, which interacts with Cdc48 and has a preference for K48-linked poly-Ub, was achieved in complex with mono-Ub[43]. However, since yOTU1 has a preference for K48-linked Ub and possesses low sequence identity to vOTU and other OTU domain proteases, only limited information on vOTU could be inferred from the yOTU1 structure. In addition to vOTU, several other viral proteases, such as papain-like protease (PLpro) from the severe acute respiratory syndrome (SARS) coronavirus, have also shown deubiquitinating and deISGylating activity to evade the innate immune system[25, 40, 44, 45].

Overview of the Coming Chapters.

Prior to this work, no vOTUs that are known to possess deISGylating activity have been structurally solved bound to Ub or UBL substrates. To address this issue and

elucidate the atomic-level structure of a member from the vOTU superfamily subclass, we have obtained the X-ray crystal structure of CCHF vOTU bound with Ub (CCHF vOTU-Ub). We also have characterized the CCHF vOTU substrate specificity for mono-Ub, ISG15, and NEDD8 and compared the results with those from human OTUB2 (hOTUB2). Additionally, we assessed CCHF vOTU's deubiquitinating activity toward K48- and K63-linked poly-Ub. Furthermore, the increasing number of vOTUs being identified in ssRNA (-) and ssRNA (+) viral genomes has spurred speculation of whether their vOTUs' specificity and subsequent role is conserved[39, 46, 47]. To gain insight into the variability of deubiquitinating and deISGylating activity, the specificity among vOTUs from nairoviruses, and how they may compare to non-nairovirus vOTUs, the enzymatic parameters and specificity of vOTUs from the CCHF, Dugbe (DUG), and Erve nairoviruses, as well as the tenuivirus Turnip Yellow Mosaic Virus in regard to Ub, poly-Ub, and ISG15 moieties were determined. Furthermore, the X-ray crystal structure of the vOTU from DUGV bound with Ub was obtained and compared to that of CCHF vOTU-Ub to assess the potential origins of any detected variability among nairovirus vOTUs. The results of the structural analysis implicated the primary structure as the main source of substrate specificity fluctuations. By comparing the structure of vOTUs from DUGV and CCHFV bound to Ub, key amino acid positions within nairovirus vOTUs that influence activity were identified.

Chapter Two: Analysis of a vOTU from the CCHF Virus in Complex with Covalently Bonded Ub

Abstract

Crimean-Congo hemorrhagic fever (CCHF) virus is a tick-borne, negative-sense, single-stranded RNA [ssRNA (-)] nairovirus that produces fever, prostration, and severe hemorrhages in humans. With fatality rates for CCHF ranging up to 70% based on several factors, CCHF is considered a dangerous emerging disease. Originally identified in the former Soviet Union and the Congo, CCHF has rapidly spread across large sections of Europe, Asia, and Africa. Recent reports have identified a viral homolog of the ovarian tumor protease superfamily (vOTU) within its large (L) protein. This protease has subsequently been implicated in downregulation of the type I interferon (IFN) immune response through cleavage of post-translational modifying proteins ubiquitin (Ub) and the Ub-like interferon-simulated gene 15 (ISG15). Additionally, homologs of CCHF vOTU have been suggested to perform similar roles in the positive-sense, single-stranded RNA [ssRNA (+)] arteriviruses. By utilizing X-ray crystallographic techniques, the structure of CCHF vOTU covalently bound to ubiquitin propylamine, a suicide substrate of the enzyme, was elucidated to 1.7 Å, revealing unique structural elements that define this new subclass of the OTU superfamily. In addition, kinetic studies were carried out with aminomethylcoumarin (AMC) conjugates of monomeric Ub, ISG15, and NEDD8 (neural precursor cell expressed, developmentally downregulated 8) substrates in order to

provide quantitative insights into CCHF vOTU's preference for Ub and Ub-like substrates.

Introduction

Crimean-Congo hemorrhagic fever (CCHF) is characterized in humans by the sudden onset of fever, myalgia, headache, dizziness, sore eyes, photophobia, and hyperanemia as well as severe hemorrhages[25, 48, 49]. The causative agent of CCHF is the CCHF virus, which is a tick-borne, negative-sense, single-stranded RNA [ssRNA (-)] virus of the genus *Nairovirus*, belonging to the viral family *Bunyaviridae*. Originally named after outbreaks in the former Soviet Union and in the Congo during the mid-20th century, the affected area of this disease has rapidly spread to large areas of sub-Saharan Africa, the Balkans, Northern Greece, European Russia, Pakistan, the Arabian Peninsula, Iran, Afghanistan, Iraq, Turkey, and recently, the Xinjiang province of China[25, 49]. The CCHF viral genome, as well as those of the closely related Dugbe and Nairobi Sheep Disease viruses, consists of three negative-sense RNA segments: small (S), medium (M), and large (L). Incubation of CCHF is 5 to 6 days, with fatalities occurring less than 7 days after signs of infection. Fatality rates for patients infected with the CCHF virus ranged from 5% to 70%, depending on phylogenetic variation of the virus, transmission route, treatment facility, and the reporting and confirmation of the case statistics[25, 50-52].

The innate immune system serves as the human's first line of defense from invading pathogens, including the CCHF virus. The type I interferon (IFN) response comprises a key component of this system by upregulating more than 300 IFN-stimulated genes (ISGs) whose products detect viral molecules, promote amplification of the type I

IFN response, modulate other signaling pathways, and directly provide antiviral activity[53]. Regulation of the type I IFN response has been shown to rely on post-translational modification by ubiquitin (Ub) and the Ub-like interferon-simulated gene 15 (ISG15)[39, 54]. Both Ub and ISG15 are expressed in a proform and cleaved to leave a double-glycine C terminus that forms an isopeptide bond with predominantly the ε-NH_2 of lysine (K) residues of a target protein through a three step enzymatic process. In addition to forming isopeptide bonds with target proteins, Ub, which contains seven lysine residues, has been observed to form polymeric ubiquitin (poly-Ub) chains. The most studied of these moieties are K29-linked, K48-linked, and K63-linked poly-Ub. While K29-linked and K48-linked polyubiquitination of proteins leads to their degradation in the lysosome and proteasome, respectively, conjugation of K63-linked poly-Ub to proteins has an activating effect, resulting in an enhanced type I IFN response[22, 23, 55-57]. Currently, more than 150 proteins have been identified as forming conjugates with ISG15, with the number of proteins forming Ub conjugates far exceeding that[37, 45]. A subset of type I IFN signaling and effector proteins that Ub and ISG15 have been shown to stabilize includes JAK1, STAT1/2, double-stranded RNA-dependent protein kinase (PKR), myxovirus-resistant protein A (MxA), and retinoic acid-inducible gene 1 (RIG-I)[27]. MxA has particularly shown to be important in type I IFN response to CCHF infection. RIG-I and several other proteins have also been shown to be targets for K63-linked poly-Ub[58].

Recently, investigators have identified a cysteine viral ovarian tumor domain (vOTU) protease colocated with the RNA-dependent RNA polymerase (RdRp) in the L

protein of the CCHF virus[39]. Interestingly, as CCHF is an ssRNA (-) virus, no protease is required to cleave a viral polypeptide to facilitate viral replication as in positive-sense ssRNA [ssRNA (+)] viruses. Furthermore, recent reports have observed that vOTU is not required for RdRp activity and for vOTU protease activity linked to impairment of the type I IFN response through its deubiquitinating and deISGylating activity[39, 40]. Since the discovery of the first ovarian tumor domain (OTU) protease in *Drosophila* oogenesis and prior to the identification of vOTU, OTU superfamily members could be divided into three subclasses according to their sequence homology, otubains, A20-like OTUs, and ubiquitin thioesterase ZRANB1[16]. With the addition of the viral OTU subclass, OTU superfamily members in more than 100 eukaryotic, bacterial, and viral proteins have now been identified[40, 43]. However, CCHF vOTU is unique in that it is the only OTU to have shown both deubiquitinating and deISGylating activity[39]. Although an X-ray structure of the yeast ovarian tumor 1 (yOTU1) domain was achieved in complex with mono-Ub, only limited information on vOTUs could be obtained by comparison since yOTU1 possesses low sequence identity to CCHF vOTU and other OTU domain proteases [43]. Still, no viral proteases that are known to possess deISGylating activity have been visualized as being bound to Ub or Ub-like substrates. To address this issue and elucidate the atomic-level structure of a member from the viral OTU superfamily subclass, we have obtained the X-ray crystal structure of CCHF vOTU bound with Ub (CCHF vOTU-Ub). We also have characterized the CCHF vOTU substrate specificity for mono-Ub, ISG15, and NEDD8 and compared the results with those from human OTUB2 (hOTUB2).

Additionally, we assessed vOTU's deubiquitinating activity toward K48- and K63-linked poly-Ub.

Methods

This research was supported in part by grants from the Partners in Scholarship of the University of Denver. Data sets were collected at the Life Sciences Collaborative Access Team (LS-CAT) 21-ID-D and 21-ID-F beamlines at the Advanced Photon Source, Argonne National Laboratory. Use of the Advanced Photon Source was supported by the U.S. Department of Energy, Office of Science, Office of Basic Energy Sciences, under contract DE-AC02-06CH11357. Use of the LS-CAT Sector 21 was supported by the Michigan Economic Development Corporation and the Michigan Technology Tri-Corridor for the support of this research program (grant 085P1000817).

Furthermore, I thank Keith Wilkinson and Maxim Balakirev for their gifts of Ub and hOTUB2 expression plasmids, respectively, as well as Stephan Ray for assistance in performing static light scattering.

Structural and sequence alignment.

The alignment of OTUs in Figure 2.1a was generated using two Protein3Dfit alignments, vOTU (3PRP) to yOTU1 (3BY4) and vOTU (3PRP) to OTUB2 (1TFF)[(59)]. These structural alignments and the amino acid sequence of the NSP2 from porcine reproductive and respiratory syndrome virus (PRRSV) were assembled using CLUSTALWPROF and TEXSHADE (http://workbench.sdsc.edu/) with the following settings: matrix, gonnet; gap-opening penalty, 11; gap extension penalty, 1; and lambda ratio, 0.85. Amino acids are color coded according to their being nonconserved (white

background), similar (lime green background), conserved (green background), or completely conserved (dark-green background, orange lettering) across the four sequences. The Ub and Ub-like alignment in Figure 2.1b was generated using CLUSTALW and TEXSHADE with the same settings used for alignment of the OTUs.

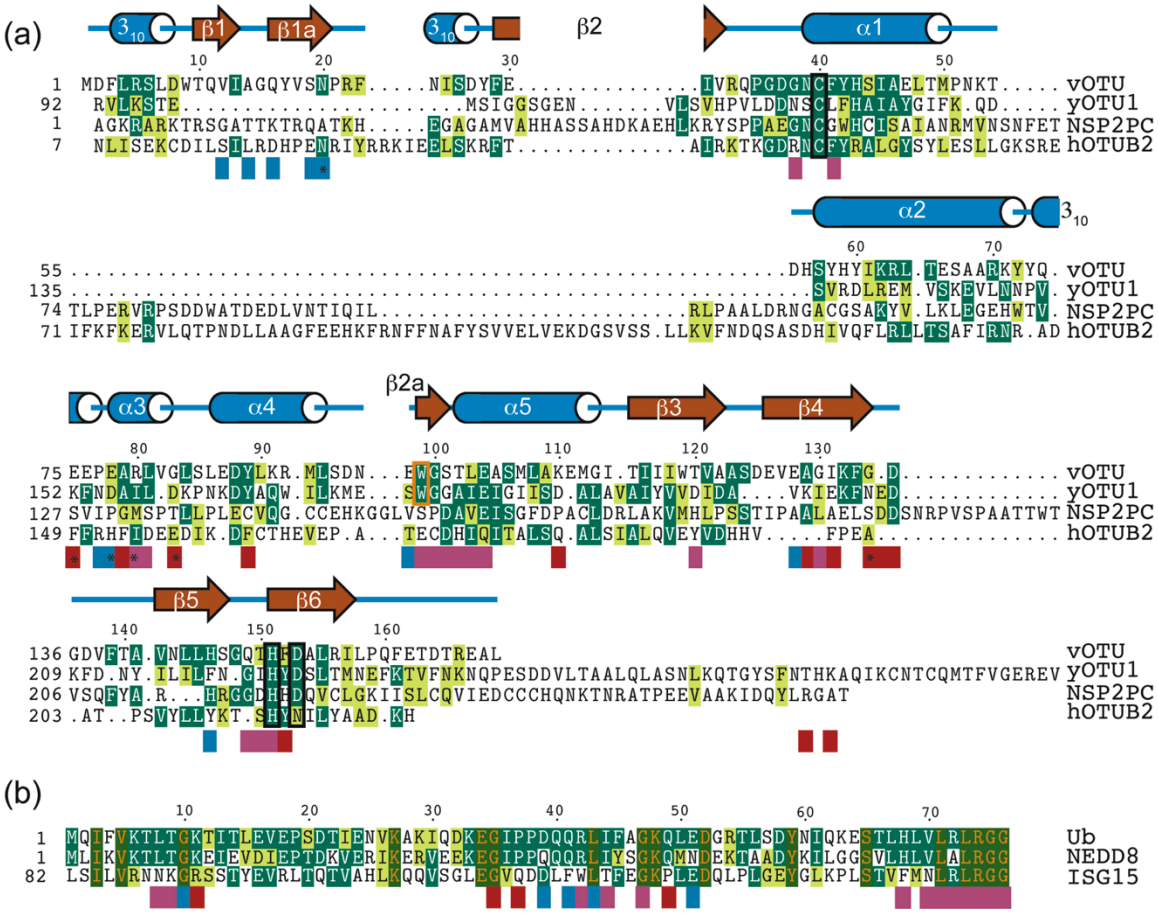

Figure 2.1. Sequence alignments of various OTU proteases and of Ub and Ub-like proteins. (a) OTUs are from CCHF virus (vOTU; GenBank accession no. AAQ98866.2), *Saccharomyces cerevisiae* (yOTU1; PDB accession no. 3BY4_A), PRRSV (NSP2PC; GenBank accession no. ACO06904.1), and *Homo sapiens* Otubain2 (PDB accession no. 1TFF_A). Secondary structure of vOTU according to the defined secondary structure of proteins (DSSP) algorithm is represented by blue cylinders (helical regions), brown arrows (β-sheet regions), and blue lines (loops). Breaks denote regions where vOTU does not have residues. Residues involved in vOTU's catalytic triad are outlined in black boxes. Residues outlined in orange boxes represent those involved in oxyanion hole formation. Colored bars below the sequence alignment indicate vOTU and yOTU1 positions within 4 Å of Ub as determined by the Contact program of the CCP4 suite[5]. Bars under vOTU unique positions are colored light blue with bars under unique yOTU1 positions in red. Equivalent positions in both vOTU and yOTU1 are shown in purple. Positions that form significant salt bridge and H-bond interactions are highlighted by an asterisk. (b) Ub and Ub-like proteins from *H. sapiens* (PDB accession no. 1UBQ_A), NEDD8 (GenBank accession no. CAG28590), and ISG15 (PDB accession no. 1Z2M_A). Colored bars below the sequence alignment indicate Ub positions within 4 Å of either vOTU and yOTU1 as determined by the Contact program of the CCP4 suite[5]. Bars colored light blue and red indicate Ub positions that interact solely with vOTU and yOTU1, respectively. Purple bars indicate Ub residues within 4 Å of both vOTU and yOTU1. Amino acids are color coded according to their being nonconserved (white background), similar (lime green background), conserved (green background), or completely conserved (dark-green background, orange lettering) across the four sequences.

Construction of CCHF vOTU and substrate proteins.

A CCHF vOTU expression construct was obtained by use of an *Escherichia coli* (*E. coli*) BL21 codon-optimized synthesis of the first 169 amino acids from the L protein in CCHFV (GenBank accession no. AAQ98866.2) by Biobasic, Inc. Along with the vOTU portion of the L protein, six histidine codons and a stop codon were added to the genes in order to provide for a C terminus histidine tag. The resulting gene was incorporated into a pET11a plasmid using NdeI and BamHI restriction sites. The construct was introduced into *E. coli* BL21 (DE3) competent cells optimized for expression by heat shock transformation. The resulting plasmid was then purified, restriction analyzed, and sequenced to verify the construct. Constructs of expression plasmids for OTUB2 as well as truncated Ub to be C-terminally modified with 3-bromopropylamine were designed according to previously established studies[42, 43, 60].

Expression and production of CCHF vOTU and Ub-Br3.

For vOTU enzymatic studies, *E. coli* harboring CCHFV vOTU was grown at 37°C in 6 liters of Luria-Bertani (LB) broth containing 100 μg of ampicillin/mL until the optical density at 600 nm reached 0.6. Expression of the vOTU gene was induced by the addition of IPTG (isopropyl-β-D-thiogalactopyranoside) to a final concentration of 0.8 mM. The culture was further grown for 4 h at 37°C and then centrifuged at 6,000*g* for 10 min. For incorporation of selenomethionyl (Se-Met) into CCHF vOTU for crystal growth, the BL21 (DE3*) E. coli* harboring vOTU was grown in minimal medium supplemented with 19 amino acids (all except methionine). L-Selenomethionine (100 mg per liter; EMD Chemicals) was added immediately before overnight induction at 25°C.

OTUB2 was expressed using previously established protocols[42]. Cells were collected and stored at -80°C until use. CCHF vOTU- and OTUB2-containing cell pellets were lysed by the addition of buffer A (500 mM NaCl, 50 mM Tris-HCl [pH 8.0]) containing 5 mg of lysozyme. The solutions were then sonicated using a Fisher Scientific series 150 sonicator on ice at 30% power with 5-s pulses for 5 min. Insoluble debris was removed by centrifugation at 26,000*g* for 45 min. The clarified extracts were filtered with a 45-μm filter and loaded directly onto Ni-nitrilotriacetic acid (NTA) agarose resin (Qiagen) pre-equilibrated in buffer A. The column was then washed with two column volumes of buffer A followed by five column volumes of a buffer A supplemented with 10 mM imidazole solution. The protein was eluted using five column volumes of a buffer A supplemented with 250 mM imidazole solution. The elution was applied to a Superdex-200 Hiload 26/60 FPLC column pre-equilibrated with buffer B (100mM NaCl, 5 mM HEPES [pH 7.4], 2 mM dithiothreitol [DTT]) and eluted at a flow rate of 1.5 mL/min. Fractions were pooled according to the chromatogram, concentrated to 10 mg/mL in a GE Vivaspin centrifuge concentrator with a 10-kDa molecular mass cutoff and filtered through a 0.65-μm Amicon spin filter. Purity of OTUB2 and CCHF vOTU was assessed by use of sodium dodecyl sulfate-polyacrylamide gel electrophoresis (SDS-PAGE).

Truncated Ub (residues 1 to 75) was expressed according to previously established protocols with the exception that after the IPTG induction, the culture was grown overnight at 25°C[43, 60]. *E. coli* BL21-CodonPlus pellets containing Ub (1 to 75) were lysed with buffer C (25 mM HEPES [pH 6.8], 50 mM sodium acetate, and 75 mM NaCl), which was augmented with 0.16% Triton X-100. As with the CCHF vOTU and

OTUB2 preparations, the solution was then sonicated on ice at 30% power with 5-s pulses for 5 min. Insoluble debris was removed by centrifugation at 30,000*g* for 45 min. The clarified extract was filtered with a 45-μm filter and then poured over a chitin column pre-equilibrated with buffer C. The column was washed with three column volumes of buffer C, followed by resuspension in two column volumes of a solution of buffer C supplemented with 100 mM sodium 2-mercaptoethanesulfonate (MESNA). The resuspension was rocked gently overnight at 4°C and eluted by filtering through a XK 26/40 GE column. The resulting Ub thioester was then derivatized with 3-bromopropylamine (Ub-Br3) according to previously described methods[43, 60]. Purity of Ub-Br3 was assessed by use of 10 to 20% Ready Gel Tris-Tricine gels (Bio-Rad, CA). All final protein concentrations were determined by absorbance at 280 nm using an experimentally determined extinction coefficient[61].

Site-directed mutagenesis of the CCHF vOTU gene.

CCHF vOTU C40A, W99A, H151A, and D153A were created by using QuikChange site-directed mutagenesis according to the manufacturer's protocol (Agilent Technologies, Inc.). The resulting mutant plasmids were introduced into *E. coli* XL1-Blue Supercompetent cells by heat shock transformation and were then propagated, purified for sequence verification, and transformed into *E. coli* BL21 (DE3) cells for enzyme expression. The complete coding regions for all mutant enzymes were sequenced by GenScript, Inc.

Fluorescent deubiquitination and deISGylation assay.

All assays were performed with 100 mM NaCl, 50 mM HEPES [pH 7.5], 0.01 mg/mL bovine serum albumin (BSA), and 5 mM DTT, by using a Corning Costar half-volume 96-well plate with a final volume of 50 μL in duplicate. The rates of the reactions for comparison of CCHF vOTU and OTUB2 were observed using a Synergy HTTR multimode plate reader (Bio-Tek) thermostated at 23°C. Specifically, the increase in fluorescence (excitation λ, 360 nm; emission, 460 nm) of 7-amino-4-methylcourmarin (AMC) upon cleavage from human Ub-AMC, ISG15-AMC, and NEDD8-AMC substrates obtained from Boston Biochem, MA, was monitored. The extinction coefficients for all three substrates were determined by adding excess CCHF vOTU to various concentrations of each substrate and allowing the reaction to run until completion. The resulting maximum fluorescence values were plotted to determine the slope and subsequently the extinction coefficients.

To determine vOTU's K_M values for Ub-AMC, ISG15-AMC, and NEDD8-AMC, the substrate concentration was varied from 0 to 50 μM. The initial rates were fitted to the Michaelis-Menten equation, $\nu = V_{max} / (1 / (K_M / [S]))$, using the enzyme kinetics (v. 1.3) module of SigmaPlot (v. 10.0; SPSS, Inc.) in order to calculate K_M and V_{max}. OTUB2 was only assessed using a substrate concentration of 2 μM for each of the three substrates.

Deubiquitinating gel shift assay.

For K63-linked and K48-linked poly-Ub deubiquitinating assays, tetra- and di-Ub linked by either K48 or K63 isopeptide bonds were purchased from Boston Biochem and

Enzo Life Sciences. These poly-Ub substrates (10 μM) were incubated with CCHF vOTU (10 nM) in a reaction buffer (100 mM NaCl, 50 mM HEPES [pH 7.5], and 2 mM DTT) at 37°C. Reactions were stopped at various times over 1 h by mixing 9 μL of each reaction with 2× SDS-Tricine sample buffer and boiling for 2 min.

CCHF vOTU and CCHF vOTU-Ub static light scattering.

CCHF vOTU and CCHF vOTU-Ub were loaded onto a Wyatt Technology Corp. size exclusion column with a pore size of 300 Å pre-equilibrated in buffer D (100 mM NaCl, 5 mM HEPES (pH 7.4), 1 mM TCEP-HCl) and attached to a mini Dawn Treos (Wyatt, CA). Molecular weights (MW) were calculated using ASTRA (v. 5.3.4.16) software and the experimentally determined extinction coefficients for CCHF vOTU and CCHF vOTU-Ub[(61)].

CCHF vOTU-Ub complex formation and crystallization.

CCHF vOTU was combined with Ub-Br3 in equal molar ratios, incubated at 37°C for 2 h and left overnight at 4°C. Complex formation was monitored using 10 to 20% Ready Gel Tris-Tricine gels (Bio-Rad). The CCHF vOTU-Ub complex was purified using a GE mono-Q column with buffer E (50 mM Tris-HCl, pH 8.0) and buffer F (50 mM Tris-HCl [pH 8.0], 1 M NaCl). Fractions were pooled according to the chromatogram and loaded onto an AP-1 (Waters) column packed with Superdex-75 pre-equilibrated with buffer D and eluted at a flow rate of 1.0 mL/min. The resulting CCHF vOTU-Ub complex was concentrated in a GE Vivaspin 6 concentrator with a 10-kDa molecular mass cutoff and filtered in a 0.65-μm Amicon spin filter. Initial crystal conditions for CCHF vOTU-Ub were determined from high-throughput screening of

Qiagen Classics and polyethylene glycol I (PEG I) screens in a 96-well sitting drop format using an Art Robbins Phoenix robot. Drops contained 0.4 µL of protein solution and 0.4 µL of precipitate with a 100 µL reservoir volume. Initial screening resulted in several hits; however, a solution containing 100 mM Sodium cacodylate (pH 6.5), 200 mM magnesium acetate, and 24% PEG 8000 produced the most viable crystals. These crystals were optimized using Additive HT Screen from Hampton Research. Final native and Se-Met CCHF vOTU-Ub crystals were obtained through vapor diffusion using a 500 µL reservoir with 4 µL hanging drops mixed 1:1 with protein solution and using a precipitant gradient of 22 to 28% PEG 8000, 100 mM Sodium cacodylate (pH 6.5), 100 to 250 mM magnesium acetate, and 2% n-octyl-β-D-glucoside.

Data collection and X-ray structural determination of CCHF vOTU-Ub complexes.

All X-ray data sets were collected using crystals mounted on nylon loops and flash frozen in liquid nitrogen. For CCHF vOTU-Ub, crystals were submerged in a 5 µL cryosolution of 28% PEG 8000, 100 mM Sodium cacodylate (pH 6.5), and 200 mM magnesium acetate. Frozen crystals were mounted under a stream of dry N_2 at 100 K. A single-wavelength anomalous dispersion (SAD) data set with a resolution to 2.3 Å and a native data set with a resolution to 1.7 Å were collected at the 21-ID-D and 21-ID-F Life Science-Collaborative Access Team beamlines, respectively, at the Advanced Photon Source Synchrotron, Argonne National Laboratory. For the SAD data collected, a single crystal of the Se-MET containing CCHF vOTU-Ub protein was collected at 0.9789 Å with a MarMosaic300 charge-coupled-device (CCD) detector (Rayonix) with the native

data collected at 0.97872 Å with a MarMosaic225 CCD detector (Rayonix). All data were subsequently processed and scaled using Denzo and Scalepack[62]. The heavy atom sites from the SAD data were determined using the program HySS from Phenix, subsequent phases were determined and refined with Phaser, Resolve was used for density modification, and an initial model was autobuilt with Resolve[63-65]. The entire path was administered via the AutoSol procedure within Phenix[66]. Once an initial model was constructed utilizing winCoot with the initial phases, the CCHF vOTU-Ub model was used to create a molecular replacement solution for the native data using Phaser and further refined using iterative cycles of model building and structure refinement using Coot and REFMAC, respectively[64, 67, 68]. Water molecules were added to $2F_o$-F_c density peaks that were >1σ using the "Find Water" winCoot program function. The final model was checked for structural quality utilizing the CCP4 suite programs Procheck and Sfcheck. Structure factors and coordinates have been deposited in the Protein Data Bank (PDB), and data processing and refinement statistics are shown in Table 2.1.

Protein structure accession numbers. Structure factors and coordinates have been assigned PDB codes 3PRM (Se-Met) and 3PRP (native).

	Se-Met	Native
Data Collection		
Space Group	$P2_12_12_1$	I 2 2 2
Wavelength (Å)	0.978	0.978
Unit Cell Dimensions		
a, b, c (Å)	60.5, 65.7, 133.13	79.3, 105.8, 113.0
α=β=γ (degrees)	90.0	90.0
Resolution (Å)	30.0 – 2.3	50.0 – 1.7
No. Reflections Observed	175,494	319,461
No. Unique Reflections	23,928	50,853
R_{merge} (%)[a]	7.2 (32.2)*	5.5 (18.6)*
I/σI	39.5 (7.3)*	22.7 (2.8)*
% Completeness	98.7 (100)*	96.5 (74.2)*
Phasing Statistics		
Number of Se-Met Sites Found	8	--
Phasing FOM	36.4	--
Resolve FOM	65	--
Refinement		
Resolution Range	30.0 – 2.3	50.0 – 1.7
No. Reflections in Working Set	22,660	48,272
No. Reflections in Test Set	1,212	2,581
R_{work} (%)[b]	20.4	17.1
R_{free} (%)[b]	26.7	21.2
Average B-factor (Å^2)	34.8	25.5
RMS deviation:		
Bond Lengths (Å)	0.02	0.01
Bond Angles (degrees)	1.64	1.35
Protein / Water Atoms	3948 / 220	4013 / 492

* The last resolution shell is shown in parentheses. [a] $R_{merge}=\Sigma_h\Sigma_I |I_I(h) - \langle I(h)\rangle| / \Sigma_h\Sigma_i I_I(h)$, where $I_I(h)$ is the i^{th} measurement and $\langle I(h)\rangle$ is the weighted mean of all measurements of $I(h)$. [b] R_{work} and $R_{free} = h(|F(h)_{obs}| - |F(h)_{calc}|) / h|F(h)_{obs}|$ for reflections in the working and test sets, respectively. R.m.s., root mean square.

Table 2.1. Data collection and refinement statistics for CCHF vOTU-Ub

Results

Kinetic characterization of CCHF vOTU using Ub-AMC and Ub-like-AMC substrates

Initial reports outlining the domain boundaries of vOTU to the first 169 residues of the CCHF viral L protein qualitatively illustrated its ability to cleave both Ub and ISG15 conjugates[39]. To gain a quantitative understanding of CCHF vOTU's order of preference for Ub and some Ub-like substrates, the cleavage of C-terminally linked 7-amino-4-methylcourmarin (AMC) conjugates of Ub, ISG15, and NEDD8 by CCHF vOTU was monitored. Using initial velocities, the K_M and V_{max} were determined for each substrate (Figure 2.2 a and c). Interestingly, CCHF vOTU possesses 6-fold higher activity for Ub than for ISG15. Furthermore, its affinities for NEDD8 are 200-fold and 30-fold less than those for Ub and ISG15, respectively. To gain a snapshot of how CCHF vOTU compares to other known OTU family members, human OTUB2 (hOTUB2) was also assessed using Ub-AMC, ISG15-AMC, and NEDD8-AMC at a fixed substrate concentration of 2 μM. Beyond the overall higher deubiquitinating/deISGylating activity of CCHF vOTU over hOTUB2 at this concentration and the mutual preference of the proteases for Ub-AMC, the proteases differ in their activity toward ISG15-AMC and NEDD8-AMC. Similar to results of previous qualitative studies utilizing band shifts by SDS-PAGE, hOTUB2 shows minimal deISGylating activity[39] (Figure 2.2b). However, it does possess the ability to cleave NEDD8-AMC, reversing the order of CCHF vOTU's preference for ISG15-AMC and NEDD8-AMC.

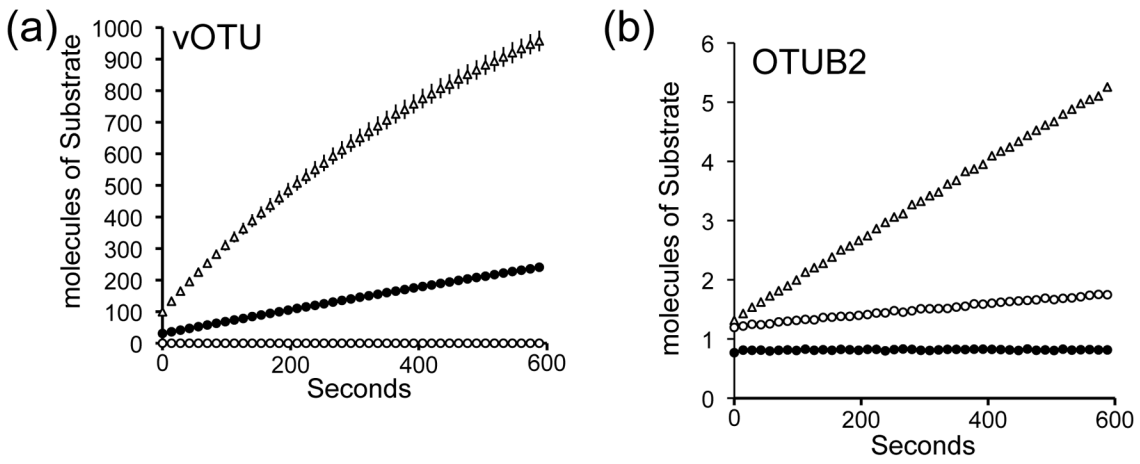

(c)

Substrate	k_{cat} (min^{-1})	K_M (μM)
ISG15-AMC	32.5 ± 3.0	2.2 ± 0.5
Ub-AMC	208 ± 15	3.8 ± 0.8
NEDD8-AMC	1.33 ± 0.25	26.6 ± 6.8

Figure 2.2. CCHF vOTU Ub and Ub-like cleavage activity. (a) 4 nM CCHF vOTU cleavage activity for Ub-AMC (Δ), ISG15-AMC (•), and NEDD8-AMC (o). The initial substrate concentration was 2 μM. Error bars represent the average errors. (b) 4 nM hOTUB2 cleavage activity for Ub-AMC (Δ), ISG15-AMC (•), and NEDD8-AMC (o). Error bars represent the average errors. (c) CCHF vOTU K_M and V_{max} constants for substrates in panel a.

X-ray structure elucidation of CCHF vOTU-Ub

To gain a more complete understanding of CCHF vOTU's mechanism for specificity of Ub and Ub-like substrates, Ub with its 76th residue replaced by bromopropylamine was used as a CCHF vOTU substrate in order to form the covalent complex CCHF vOTU-Ub. Screening CCHF vOTU-Ub against commercial crystal precipitant screens, and using an additive screen for optimization, yielded single diffracting crystals obtained in a mixture of PEG 8000, sodium cacodylate (pH 6.5), magnesium acetate, and n-octyl-β-D-glucoside. A native data set was subsequently obtained to 1.7 Å in an I222 space group, but molecular replacement employing composite models generated from yOTU1-Ub, OTUB1, and OTUB2 failed to elucidate a solution[37, 42, 43]. However, using selenomethionyl (Se-Met)-substituted CCHF vOTU-Ub, phases were obtained using SAD to 2.3 Å in the space group of $P2_12_12_1$ (Table 2.1).

The resulting solution was two CCHF vOTU-Ub molecules in the asymmetric unit. Once an initial model was constructed, a molecular replacement solution also containing two CCHF vOTU-Ub molecules in the asymmetric unit was readily obtained from the native data set (Figure 2.3a; Table 2.1). In the final model, all of the Ub residues and CCHF vOTU residues 1 to 165 per CCHF vOTU-Ub were visualized. Although Se-Met and native crystals were obtained under similar conditions and resulted in solutions containing two CCHF vOTU-Ub molecules in the asymmetric unit, their differing space group symmetries underline the fact that the molecular arrangement of the dimer and the crystal lattice differ radically.

Static Light Scattering of CCHF vOTU and CCHF vOTU-Ub Complex

To further investigate the oligomeric state of CCHF vOTU-Ub and CCHF vOTU, static light scattering was performed. For vOTU, 95.7% of the sample's molecular mass was calculated at 18.7 kDa with a 2% error, confirming that CCHF vOTU is a monomer in solution. As for CCHF vOTU-Ub, 72.5% of the sample possessed a monomeric complex molecular mass of 27.5 kDa with a 1% error. The remaining 25% of the sample was found to possess a molecular weight of 54.2 kDa with a 1% error (data not shown). Overall, the results coupled with the differences in lattice arrangement suggest that the most probable biologic assembly is that of one CCHF vOTU interacting with one Ub.

Comparison of CCHF vOTU to other OTU superfamily members

The overall structure of the Ub in CCHF vOTU-Ub is consistent with previous Ub structures; however, despite CCHF vOTU's structure sharing many tertiary elements with other structurally elucidated OTUs, several divergent regions are readily apparent[43, 69]. In keeping with the OTU superfamily, CCHF vOTU's core is composed of a β-sheet surrounded by helices. In CCHF vOTU's case, five α helices and a 3_{10} helix flank the core β-sheet on one side, with three 3_{10} helices on the other (Figure 2.3b). Although CCHF vOTU possesses a β-sheet core with surrounding helices, similarities with other OTU superfamily members end there. Unlike previous yOTU1 and OTUB1/2 structures that possessed a core formed from only five to six β-strands, CCHF vOTU's β-sheet is comprised of seven β-strands arranged as follows: ↓ β2,↑ β6, ↑ β5, ↑ β3, ↓ β4, ↑ β1a,

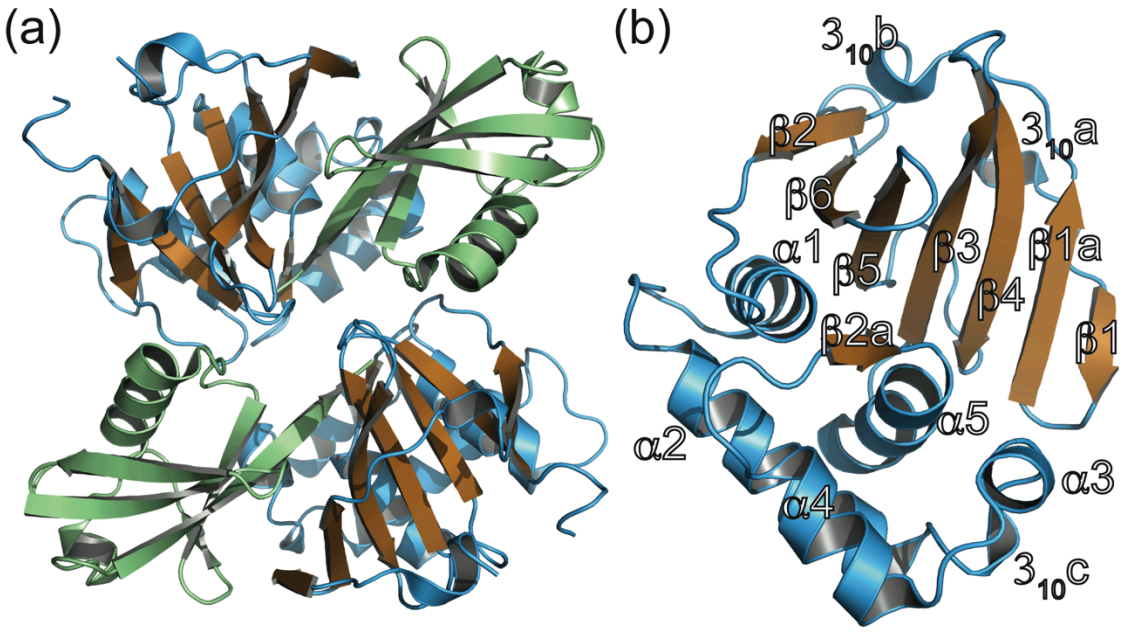

Figure 2.3. I222 asymmetric unit of CCHF vOTU-Ub crystal and CCHF vOTU monomer alone. (a) Cartoon representation of the I222 asymmetric unit of CCHF vOTU-Ub. Ub is rendered in light green, with CCHF vOTU rendered according to its secondary structures: helices in light blue, β-strands in orange, and loops in blue. (b) CCHF vOTU monomer labeled according to secondary structure.

and ↑ β1 (Figure 2.3b)[37, 42, 43]. An additional β-strand, β2a, forming an anti-parallel β-sheet with a β-strand formed from Ub residues 73 to 75, was also observed (Figure 2.3b).

A comparison of CCHF vOTU directly to two other OTUs, yOTU1 and OTUB2, highlights the structural uniqueness of CCHF vOTU. By employing secondary structure matching to align the structures of yOTU1, OTUB2, and CCHF vOTU, four significant structurally divergent regions can be identified (Figure 2.4a and b). Region 1 concerns the arrangements of β-strands that form the core of each structure. Within that region, CCHF vOTU has a two-β-strand extension of its β-sheet formed from the presence of β1 and β1a. There is no equivalent to CCHF vOTU's β4, β1, and β1a in OTUB2, whereas yOTU1 does have a β1, but this β1 forms against β2 on the other end of the β-sheet core. The existence of these extra β-strands in CCHF vOTU requires that CCHF vOTU's polypeptide pass behind the β-sheet, forming a 3_{10} helix prior to forming β2. This loop fills in region 2, which is normally occupied by a conserved α6 helix in all known OTU superfamily members. The presence of β1 and β1a also sterically forbids CCHF vOTU from binding Ub in the same orientation as yOTU1 does (Figure 2.4c and d). The result is a 30° twist of CCHF vOTU's bound Ub in comparison to that of the yOTU-Ub structure. These differences in orientation of Ub or its absence in relationship to the core β-sheet of CCHF vOTU, yOTU1, and OTUB2 result in differences in the orientation of α3, which comprises region 3 and is a component of the Ub binding interface. Last, region 4 highlights the absence of α helices present in OTUB1/2 but absent in yOTU1 and CCHF vOTU.

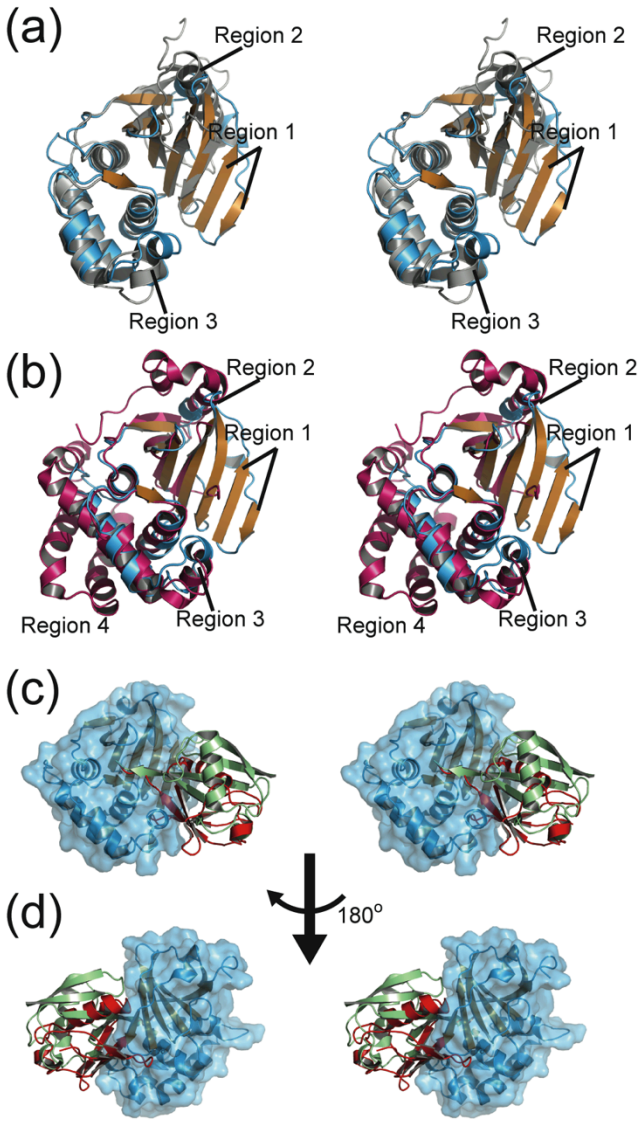

<u>Figure 2.4</u>. CCHF vOTU and CCHF vOTU-Ub comparison to OTUB2, yOTU1, and yOTU1-Ub. (a) Divergent-eyed stereo view of CCHF vOTU (orange and blue) aligned with yOTU1 (gray) using secondary structure matching though COOT. (b) Divergent-eyed stereo view of CCHF vOTU colored as in panel a aligned with hOTUB2 (magenta). (c) Divergent-eyed stereo view of CCHF vOTU-Ub with Ub sourced from a secondary structure alignment of CCHF vOTU-Ub and yOTU1-Ub. CCHF vOTU is rendered as a cartoon and colored according to secondary structure, with helices in light blue, β-strands in orange, and loops in blue. Ub of the CCHF vOTU-Ub complex is also rendered as a cartoon and colored light green. Ub from a yOTU1-Ub that was aligned with CCHF vOTU-Ub using the secondary structure matching of CCHF vOTU and yOTU1 is rendered as a cartoon in red. (d) Shown is a 180° y-axis rotation of panel c.

CCHF vOTU binding interface with Ub

The 1,065 $Å^2$ of buried surface area between CCHF vOTU and Ub can be optimally described by its classification into three areas (Figure 2.5a). One of the two most prominent areas of interaction, area I, is comprised of the interface between Ub residues 72 to 75, including the propylamine adduct of Ub and numerous residues of CCHF vOTU (Figure 2.5b). Four major factors drive the formation of this interface. The first of these is the formation of hydrogen (H) bonds between the main chain atoms of Ub residues 72 to 75, including the amine in the propylamine adduct, and the main chain atoms of CCHF vOTU's W99, G100, S101, and T150. The overall result of these H bonds is the creation of a β-sheet joining CCHF vOTU and Ub. In addition to H-bond formation, a network of polar bonds and salt bridges is formed between Ub's R72 and R74 and CCHF vOTU's E98, E78, and S101. Beyond electrostatic interactions and despite the distinctly negative electropotential of area I, a row of CCHF vOTU residues, I118, I131, V18, and V12, form a hydrophobic trough deep in CCHF vOTU's binding surface. Part of this trough resides in area I and facilitates a favorable interaction with Ub's L73. The hydrophobic trough continues into another prominent area of interaction, area II, with the accommodation of Ub's V70 and I44. Similar to area I, a network of polar bonds and salt bridges is formed between Ub's E51, Q49, and R42 and CCHF vOTU's R80, E78, P77, and Q16 (Figure 2.5c) in area II. Just as the CCHF vOTU hydrophobic trough creates favorable interactions in areas I and II, area III also benefits from Ub's L8 being buried in this trough between CCHF vOTU's V18 and I131. Also, a polar interaction is observed in area III by Ub's K6 interacting with CCHF vOTU's N20

through a water molecule. Overall, 25 residues from CCHF vOTU and 18 residues from Ub are involved in the formation of the interface. Not surprisingly, the 18 residues of Ub involved are isolated to one side of the Ub. However, a comparison to Ub bound to yOTU1 illustrates that the Ub surface that CCHF vOTU interacts with is not the same as that of yOTU1.

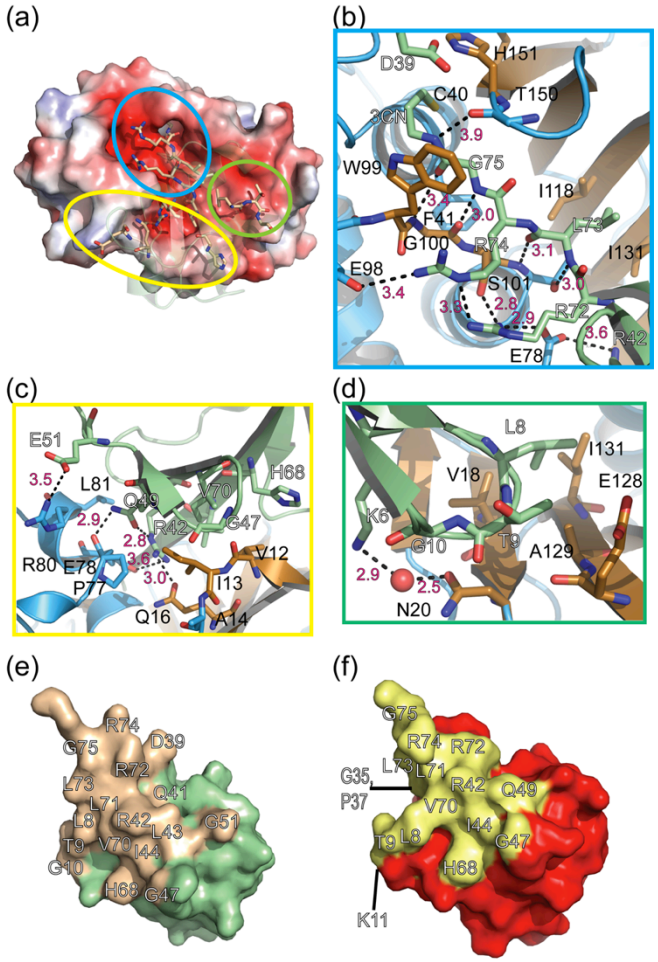

Figure 2.5. CCHF vOTU-Ub binding interface. (a) Electropotential surface rendering of CCHF vOTU generated with the adaptive Poisson-Boltzmann solver (APBS) plug-in of Pymol software[1-4]. APBS settings were -4 for the negative maximum and 4 for the positive maximum. Ub is illustrated as a light-green transparent cartoon. Ub residues that reside within 4 Å of vOTU as determined by the use of the Contact program part of the CCP4 suite are colored tan[5]. Three colored ovals highlight the three regions of interactions between CCHF vOTU and Ub: area I (cyan), area II (yellow), and area III (green). (b) Close-up of area I with CCHF vOTU rendered in cartoon and stick format with color according to the secondary structure: helices in light blue, β-strands in orange, and loops in blue. Ub is also rendered in cartoon and stick format but is colored in green. A cartoon view of the secondary structure of residues 70 to 75 in Ub has been hidden for clarity. White labels indicate Ub residues, black labels indicate CCHF vOTU, and pink labels and dashes indicate distances. All distance numbers are in angstroms. (c and d) Close-up of area II and area III, respectively, with CCHF vOTU and Ub colored as in panel b. (e) Surface rendering of a 180° x/y-axis rotation of the Ub bound in panel a. In general, Ub is colored light green, with the regions colored tan in panel a colored the same in panel b. (f) Surface rendering of Ub from yOTU1-Ub in a similar orientation as Ub in panel b. Ub is colored in red, with residues within 4 Å of yOTU1, as determined by the use of the Contact program from the CCP4 suite, colored yellow[5].

CCHF vOTU's catalytic triad

As CCHF vOTU was predicted to be a cysteine protease and only possesses one cysteine (C40), research groups were quick to identify it as critical to CCHF vOTU's protease activity. However, identification of the remaining two residues involved in CCHF vOTU's catalytic triad has remained elusive. Recent studies have proposed H151 of CCHF vOTU as a member of the CCHF vOTU catalytic triad but have only reported on activity of the C40/H151 double mutant[39]. Additionally, the presence of a histidine at the equivalent position of CCHF vOTU's E98 in the proposed viral OTU subclass arterivirus member's NSP2 proteases has also spurred speculation on the location of the catalytic histidine within the viral OTU subclass [39, 70]. As for the aspartic acid component of the catalytic triad, D37 and D153 have been suggested as candidates[71]. To clarify the identity of the complete catalytic triad, the active site of CCHF vOTU was inspected. Although several CCHF vOTU histidine and aspartic acid residues, including H43 and D37, were within the general area of that catalytic cysteine, only H151 and D153 were in close enough proximity and in the correct orientation to assist in the deprotonation of CCHF vOTU's C40 (Figure 2.6a). To confirm the essentiality of these amino acids, they were mutated to alanine, and the activity of the resulting protein containing CCHF vOTU was assessed. CCHF vOTU mutants C40A and W99A exhibited an ~1,000-fold loss of V_{max} compared to that for wild-type (wt) CCHF vOTU. The CCHF vOTU mutant H151A possessed only a slightly higher V_{max} than that of CCHF vOTU mutants C40A and W99A, with ~350-fold loss of activity compared to that of the wt. The most active CCHF vOTU mutant, D153A, was still ~40- fold less active than wt CCHF

vOTU. All of the CCHF vOTU mutants exhibited a K_M of ~4-fold more than that for wt CCHF vOTU (Figure 2.6b).

(a)

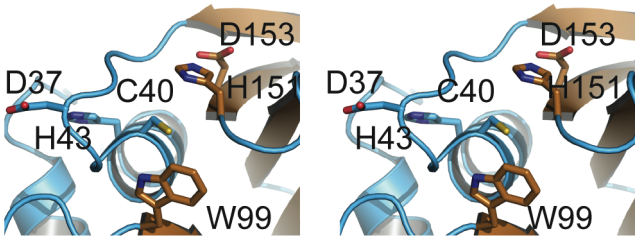

(b)

Mutation	V_{max} (min^{-1})	K_M (μM)
C40A	0.18 ± 1.0 x 10^{-2}	13.7 ± 1.7
W99A	0.21 ± 1.0 x 10^{-2}	12.6 ± 1.5
H151A	0.59 ± 2.0 x 10^{-2}	10.5 ± 0.8
D153A	5.5 ± 2.0 x 10^{-1}	15.8 ± 1.3
wt	208 ± 15	3.8 ± 0.8

Figure 2.6. Active site of CCHF vOTU. (a) Cartoon and stick rendering of CCHF vOTU's active site. CCHF vOTU is colored according to its secondary structures, with helices in light blue, β-strands in orange, and loops in blue. (b) Ub K_M and V_{max} constants for catalytic triad CCHF vOTU mutants.

CCHF vOTU's K63- and K48-linked deubiquitinating activity

To investigate CCHF vOTU's activity toward both K63- and K48-linked di-Ub species, both K63- and K48-linked species of di-Ub were acquired. Cleavage of 10 μM di-Ub species by 10 nM CCHF vOTU was monitored over the course of 1 h by their products being resolved on a 10 to 20% Ready Gel Tris-Tricine gel and visualized by staining with Coomassie blue (Figure 2.7a). Interestingly, there is no difference in CCHF vOTU's activity toward the two di-Ub substrates. To assess whether larger poly-Ub species could also be cleaved by CCHF vOTU, K48- and K63-linked tetra-Ub was obtained. These tetra-Ub species were cleaved in the same manner as their di-Ub counterparts. Unlike the comparable activity between K48- and K63-linked di-Ub species, CCHF vOTU appears to have a slight preference for the two tetra-Ub substrates.

For K63-linked tetra-Ub, almost no poly-Ub species are visible after 10 min, whereas several poly-Ub species appear at this time frame, and faint bands can also be seen at the 60-min time frame in the K48-linked tetra-Ub reactions (Figure 2.7a).

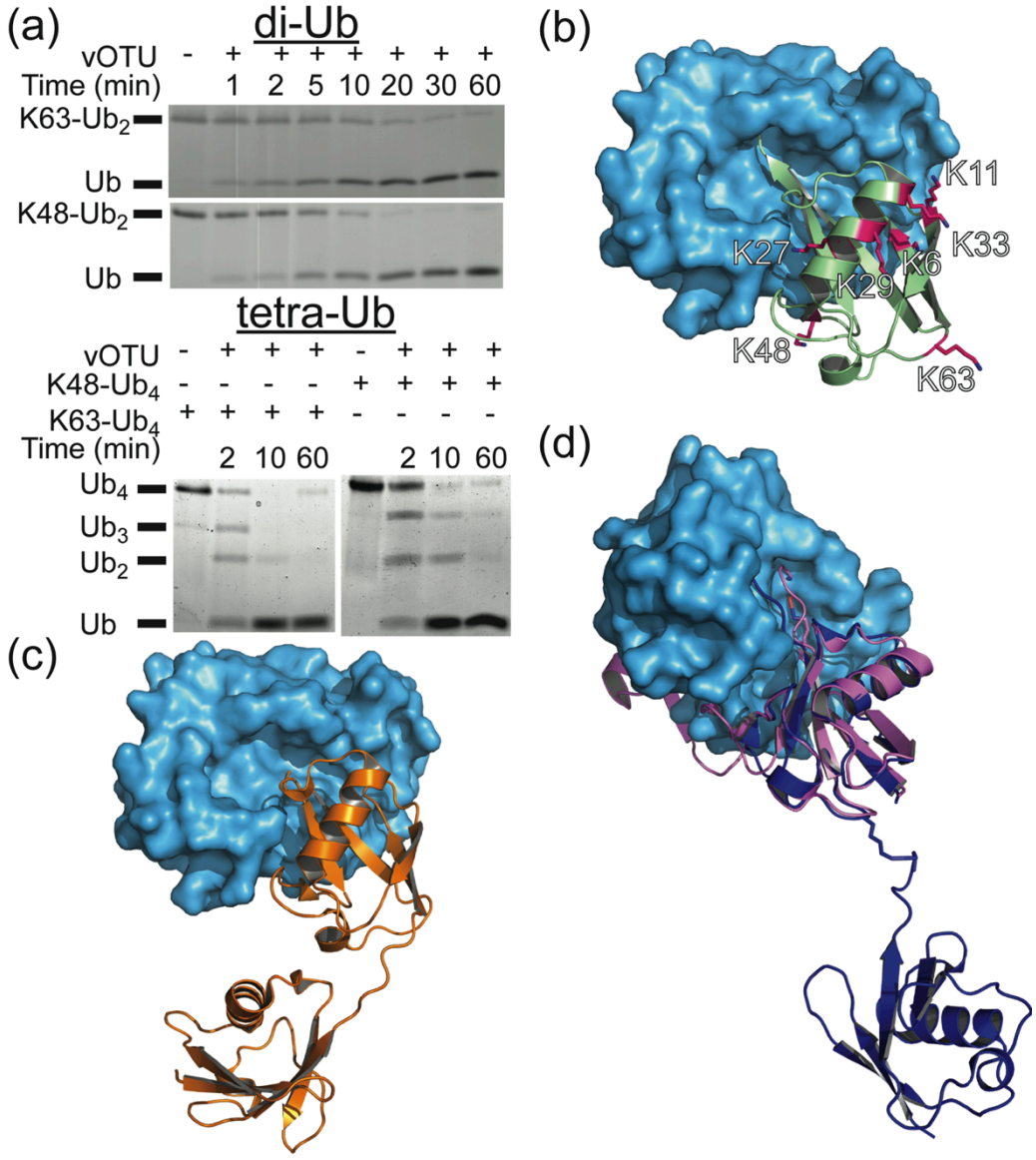

Figure 2.7 Polydeubiquitination as well as Poly-Ub and CCHF vOTU-ISG15 models. (a) CCHF vOTU's cleavage of K48-linked di-Ub and K63-linked di-Ub (top panel) and K48-linked tetra-Ub and K63-linked tetra-Ub (bottom panel). (b) Location of lysine residues on CCHF vOTU-bound Ub. The surface of CCHF vOTU is colored blue, with Ub shown as a cartoon in light green. Lysine residues located in Ub are colored magenta and labeled accordingly. (c) ISG15 (2JF5) aligned using a secondary structure-matching tool in Coot to the Ub bound to CCHF vOTU[5]. ISG15 is rendered as a cartoon in orange. (d) K63-linked di-Ub (3H7P) and K48-linked di-Ub (2BGF) aligned using a secondary structure-matching tool in Coot to the Ub bound to CCHF vOTU[5]. K63-linked di-Ub rendered as a cartoon in dark blue, with K48-linked di-Ub in purple[6, 7].

Discussion

CCHF vOTU and other viral OTU superfamily members

In general, viral genomes undergo a higher rate of mutation and recombination than their eukaryotic and prokaryotic counterparts. The CCHF virus is no different. Interestingly, the L protein tends to be the most conserved among those in the three-segmented genome, suggesting an evolutionary need to minimize substantive changes in the L protein[72]. For the L protein itself, the RdRp's variable region (amino acids 752 to 851) tends to be the source of most L-protein diversity[73]. Intriguingly, this leaves the vOTU containing region of the L protein only a few mutations between GenBank entries from strains from Kosovo (ABW17160), Turkey (ACT88368), and China (ADD64466) (see entry for CCHF vOTU, AAQ98866.2). Of the 16 polymorphic sites in vOTUs from different CCHF strains, only three are located at the vOTU-Ub interface: A14D, R80K, and E128G. As CCHF vOTU's R80 is involved in a salt bridge with Ub's D98, the change of arginine to a shorter lysine residue may impact binding (Figure 2.5b). Unlike the case for the R80K polymorphism, any impact of A14D and E128G on protease activity and its effects on virulence are hard to predict, as these residues have no readily apparent side chain interactions in CCHF vOTU-Ub (Figure 2.5c and d). Nairovirus homologs of Dugbe and Nairobi Sheep Disease viruses are also very similar, 72 to 76%, respectively, to the CCHF virus vOTU. Most of the differences between the nairoviruses lay outside the binding interfaces. However, as with other strains of CCHF vOTU, differences found at R80 and E128 might suggest that even closely related nairovirus homologs might not have the exact same protease specificity or catalytic capacity.

Although CCHF vOTU and its nairovirus homologs are highly conserved, other vOTU homologs from the arterivirus genus, including PRRSV, show only less than 40% similarity with CCHF vOTU. Despite the low sequence similarity in general, the elucidation of the CCHF vOTU structure coupled with the analysis of an arterivirus PRRSV amino acid sequence allows some insight into possible tertiary features of arterivirus vOTUs. One striking example is that regions of higher conservation between CCHF vOTU and the PRRSV vOTU homologs are at the same amino acid positions as those involved in substrate binding. This suggests that arterivirus vOTUs may possess a substrate-binding interface similar to that of PRRSV (Figure 2.1a). In addition, arterivirus vOTUs have a high degree of sequence similarity with the region containing the catalytically relevant cysteine as well as a shared amino acid motif among OTU superfamily members HXD/N, where X is a 5- to 6-member side chain ring containing residues. Since this motif now contains the catalytically relevant histidine and aspartic acids in a vOTU superfamily member, there is a strong likelihood that the arterivirus vOTUs catalytic triad residues also reside in this motif.

Potential vOTU primary and tertiary structural determinates for substrate recognition

yOTU1 shares only 40% of the amino acids positions that comprise the CCHF vOTU-Ub binding interface. This, along with the significant difference in the orientation of Ub between the CCHF vOTU-Ub and yOTU1-Ub structures, underlines the potential diversity of substrate recognition within the OTU superfamily. Although only through an intensive mutagenesis approach will the complete understanding of CCHF vOTU

substrate recognition be ultimately known, some likely candidates can be envisioned. CCHF vOTU's R80, E51, and N20 are some of these candidates. As a methionine or isoleucine in OTUB2 and yOTU1, respectively, R80 forms a salt bridge with E51 in Ub. Interestingly, E51 is also a glutamate in ISG15 but is a glutamine in NEDD8. In the case of CCHF vOTU's E78, this residue creates two salt bridges with R72 and R74 of Ub. As R74 of Ub is a leucine in NEDD8 and E78 of CCHF vOTU is a histidine in OTUB2, the presence of both of these salt bridges is not likely in CCHF vOTU-NEDD8 or in OTUB2-Ub. Last, N20 is located on CCHF vOTU's unique β1-β1a tertiary element and forms a set of polar interactions with Ub's K9 through a water molecule. This interaction should be absent completely in OTUB1/2 and yOTU1.

In addition to CCHF vOTU's N20 proposed role in mono-Ub and Ub-like recognition, its interaction with K6 of Ub suggests that CCHF vOTU may not be able to cleave K6 linked poly-Ub conjugates. Analysis of other lysine side chains in the CCHF vOTU-Ub structures also suggests that through steric hindrance, CCHF vOTU may not prefer K27- or K11-linked poly-Ub (Figure 2.7b). These side chains are buried within the CCHF vOTU-Ub interface. When CCHF vOTU-Ub is used as a scaffold for modeling CCHF vOTU-ISG15, CCHF vOTU-K63-linked di-Ub, and CCHF vOTU-K48-linked di-Ub, the results would suggest that CCHF vOTU might also have difficulty also cleaving K48-linked poly-Ub (Figure 2.7b - d). Within the CCHF vOTU-Ub structure, K48 is located near CCHF vOTU's surface, and when the K48 di-Ub NMR structure (2BGF) is overlaid, significant steric clashes are observed. Interestingly, CCHF vOTU has only a slight preference for K63-linked tetra-Ub over its K48-linked counterpart. Of course, this

is in contrast to the slight preference that OTUB1 shows for K48-linked poly-Ub over K63-linked poly-Ub[43]. Additionally, several di-Ub products are observed when CCHF vOTU cleaves K48-linked tetra-Ub, suggesting that K48-linked poly-Ub can adopt a conformation that allows vOTU access to its isopeptide bonds. CCHF vOTU's robust activity toward K63-linked poly-Ub is also intriguing, as a cysteine protease from murine cytomegalovirus shows a more distinct preference for K48-linked di-Ub over K63-linked di-Ub[74]. CCHF vOTUs cleavage of K63-linked poly-Ub protein conjugates with rates slightly greater than K48-linked tetra-Ub might be reflective of the K63-linked poly-Ub quaternary structure being similar to that of ISG15 (Figure 2.7c and d). With K63-linked poly-Ub and ISG15 activating and/or stabilizing key antiviral proteins, and K48-linked poly-Ub's proteasome-vectoring attributes, CCHF vOTU activity likely has a significant impact on these cellular activities.

Chapter 2 is in part a reprint of the material as it appears in Capodagli G. C., McKercher M. A., Baker E. A., Masters E. M., Brunzelle J. S., and Pegan S. D. (2011) *Structural analysis of a viral ovarian tumor domain protease from the Crimean-Congo hemorrhagic fever virus in complex with covalently bonded ubiquitin*. J Virol, **85(7)**: 3621-30. The dissertation author was primary researcher and author of this publication.

Chapter Three: Diversity of Ub and ISG15 Specificity among Nairoviruses' vOTU

Abstract

Nairoviruses are responsible for numerous diseases that affect both humans and animals. Recent work has implicated the viral ovarian tumor domain (vOTU) as a possible nairovirus virulence factor due to its ability to edit ubiquitin (Ub) bound to cellular proteins and, at least in the case of Crimean-Congo hemorrhagic fever virus (CCHFV), to cleave the Ub-like protein interferon-stimulated gene 15 (ISG15), a protein involved in the regulation of host immunity. The prospective roles of vOTUs in immune evasion have generated several questions concerning whether vOTUs act through a preserved specificity for Ub- and ISG15-conjugated proteins and where that specificity may originate. To gain insight into the substrate specificity of vOTUs, enzymological studies were conducted on vOTUs from Dugbe, CCHFV, and Erve nairoviruses. These studies revealed that vOTUs originating from different nairoviruses display a significant divergence in their preference toward Ub and ISG15. In addition, a recently identified vOTU from the turnip yellow mosaic tymovirus was evaluated to elucidate any possible similarities between vOTUs originating from different viral families. Although possessing a similar preference for certain polymeric Ub moieties, its activity toward Ub in general was significantly less then those of nairoviruses. Lastly, the X-ray crystallographic structure of the vOTU from the Dugbe nairovirus was obtained in complex with Ub to reveal structural commonalities of vOTUs originating from

nairoviruses. The structure suggests that divergences between nairovirus vOTUs specificity originate at the primary structural level. Comparison of this structure to that originating from CCHFV identified key residues that infer the substrate specificity of vOTUs.

Introduction

Nairoviruses are negative-sense, single-stranded RNA [ssRNA (-)] viruses responsible for numerous diseases in both humans and animals. There are 34 known viruses belonging to the genus *Nairovirus* of family *Bunyaviridae*. Of these, the tickborn Crimean-Congo hemorrhagic fever virus (CCHFV), Dugbe virus (DUGV), and Nairobi sheep disease virus (NSDV) have been the most investigated. Although these viruses share considerable genomic similarity, their effects on both humans and animals vary from mild illness to loss of life. CCHFV, the most lethal to humans, is endemic across large swaths of sub-Saharan Africa, southeast Europe, and Asia. Fatality rates for CCHFV range from 5 to 33% depending on reported and confirmed case statistics. However, some outbreaks, to include the recent ones in India and the Sudan, suggest the rates could be up to 70 to 80%[49-52, 75]. CCHFV has also been reported to infect sheep, goats, cattle, horses, and donkeys in the wild; however, the disease does not manifest in a fatal form for these animals[76]. Comparatively, infection of humans by NSDV and DUGV can cause a febrile illness but no associated fatalities [77, 78]. NSDV is found in Eastern and Central Africa, and the Asian variant Ganjam nairovirus (GANV) found in India has been observed to infect sheep with a mortality of up to 90%, generating economic distress within infected areas[78-80]. Alternatively, DUGV, which originates

from sub-Saharan Africa, has not been found to be fatal for any known species. However, DUGV can cause mild febrile illness in species beyond humans, particularly cattle that it predominantly infects[81, 82]. In addition to these human disease-causing nairoviruses, the Erve Virus (ERVEV) from northwest Europe has been implicated as a causative agent in human thunderclap headaches. ERVEV was isolated from the white-toothed shrew in 1982 and classified by indirect immunofluorescence assay (IFA) as belonging to the Nairovirus genus, ERVEV has only been recently sequenced limiting previous exploration of its proteome [83].

The genome of nairoviruses is partitioned into three RNA segments: small (S), medium (M), and large (L). Surprisingly, unlike other *Bunyaviridae* family members, the nairoviruses' L segment contains not only a RNA-dependent RNA polymerase but also a viral ovarian tumor domain protease homolog (vOTU) [39]. As ssRNA (-) viruses, no viral protease is required for nairovirus genome replication [40]. Instead, nairovirus vOTUs have been proposed to be one potential virulence factor[39, 40, 84-86]. Unlike the previously identified *Bunyaviridae* family virulence factor, nonstructural protein NSs, which blocks transcription of alpha/beta interferon (IFN-α/β) and is absent in nairoviruses, vOTUs are suggested to impair innate immunity through deubiquitinating and deISGylating activity [87, 88]. As a deubiquitinating and deISGylating protease, nairovirus vOTUs fall into one of five protease superfamilies that facilitate a myriad of cellular processes such as proteasomal degradation, cell division, and regulation of the innate immune response through reversal of post-translational modification by ubiquitin (Ub)[89]. The multitude of outcomes is achieved by Ub's ability to form polymeric Ub (poly-Ub) chains through

Ub's C-terminal glycine forming either a peptide bond via the N terminus (linear) or an isopeptide bond with one of the seven lysines (K6, -11, -27, -29, -33, -48, and -63) of a partnering Ub. Each linkage type has been implicated in acting as a specific type of cellular signal. The canonical linkages of K48 and K63 poly-Ub were the first studied and are associated with proteosomal degradation and induction of the type I IFN (IFNI) immune response, respectively[22, 23]. In the last decade the more non-canonical and less well studied linkages have been tied to lysozomal trafficking (K29), regulation of cellular division (K11), and modulation of immunological signaling pathways (K6, K27, and K33)[18-21, 90].

Recent studies have observed divergences in immunological response between human cells infected by DUGV and CCHFV underlining the differences in which the respective viruses influence cellular immunity[91, 92]. Also, this phenomenon has been observed between GANV and NSDV. Specifically, Holzer et al. recently narrowed IFN-α/β suppression to primarily the first 169 amino acids of the L-protein and suggested that the vOTU GANV may have less activity than that of CCHFV[93]. However, the use of the recombinant overexpression system limited the ability to detect the extent of variability in deubiquitinating and deISGylating activity between the vOTUs originating from these viruses. This limitation has been observed in other studies, where unnaturally high expression of vOTUs, or when generously added *in vitro*, leading to a nearly 1:1 ratio of vOTU to Ub or ISG15 substrates, likely masks their specificity for poly-Ub and ISG15 conjugates, particularly during early viral replication[39, 46, 94]. In addition, the increasing number of vOTUs being identified in ssRNA (-) and ssRNA (+) viral genomes, including

the rice stripe tenuivirus (RSV), turnip yellow mosaic tymovirus (TYMV), and arteriviruses such as porcine reproductive and respiratory syndrome (PRRSV), have spurred speculation of whether their vOTUs' specificity and subsequent role is conserved[39, 46, 47].

To gain insight into the variability of deubiquitinating and deISGylating activity, the specificity among vOTUs from nairoviruses and how they may compare to non-nairovirus vOTUs, the enzymatic parameters and specificity of vOTUs from CCHFV, DUGV, ERVEV, and TYMV in regards to Ub, poly-Ub, and ISG15 moieties were determined. Finally, the X-ray crystal structure of the vOTU from DUGV bound with Ub was obtained to assess the potential origins of any detected variability among nairovirus vOTUs implicating primary structure as the main source of substrate specificity fluctuations. By comparing the structure of vOTUs bound to Ub from DUGV and CCHFV, key amino acid positions within nairovirus vOTUs that influenced activity were identified.

Methods

I thank Keith Wilkinson for his gift of Ub expression plasmids. The Advanced Light Source is supported by the Office of Science, Office of Basic Energy Sciences, of the U.S. Department of Energy under contract DE-AC02-05CH11231. This study was supported with funding provided by National Institute of Health grants 1R03AI092249-01 and 1R03MH097507-01A1, as well as by the University of Denver's Partnership in Scholarship Program.

Construction of vOTUs and Ub-Br3 expression vectors.

The production of the vOTU expression construct harboring the 169 amino acids from the L protein in CCHFV (CCHF vOTU; GenBank accession no. AAQ98866.2) is as previously described[85]. The vOTUs from TYMV, ERVEV, and DUGV (TYM vOTU, ERVE vOTU, and DUG vOTU) were generated using the *Escherichia coli* (*E. coli*) BL21 codon optimized synthesis by GenScript, Inc. The DUG vOTU gene expression construct contained the first 169 amino acids from the L protein of DUGV (GenBank accession no. AAB18834.1). For the ERVEV vOTU expression construct, the first 171 amino acids from the L protein in ERVEV (GenBank AFH89032.1), which correspond to the first 169 amino acids of CCHF vOTU and DUG vOTU (Figure 3.1) and includes the OTU domain as described by Dilcher et al. were utilized[83]. Similarly to the CCHF vOTU construct, six histidines and a stop codon were added to ERVE vOTU and DUG vOTU constructs to generate a C-terminal histidine tag. For the TYM vOTU expression vector, the 151-amino-acid vOTU domain (residues 728 to 879) of TYMV (GenBank accession no. NP_663297.1) that included the vOTU domain as described in Chenon et al. with a six-histidine N terminus tag was synthesized[46]. DUG vOTU, TYM vOTU, and ERVE vOTU were incorporated into pET11a plasmids using NdeI and BamHI restriction sites. The vOTU constructs were introduced into *E. coli* BL21 (DE3) competent cells by heat-shock transformation. The resulting plasmids were then purified, restriction analyzed, and sequenced to verify the construct. Constructs of expression plasmids for truncated human Ub to be C-terminally modified with 3-bromopropylamine were designed according to previously established studies[43, 60].

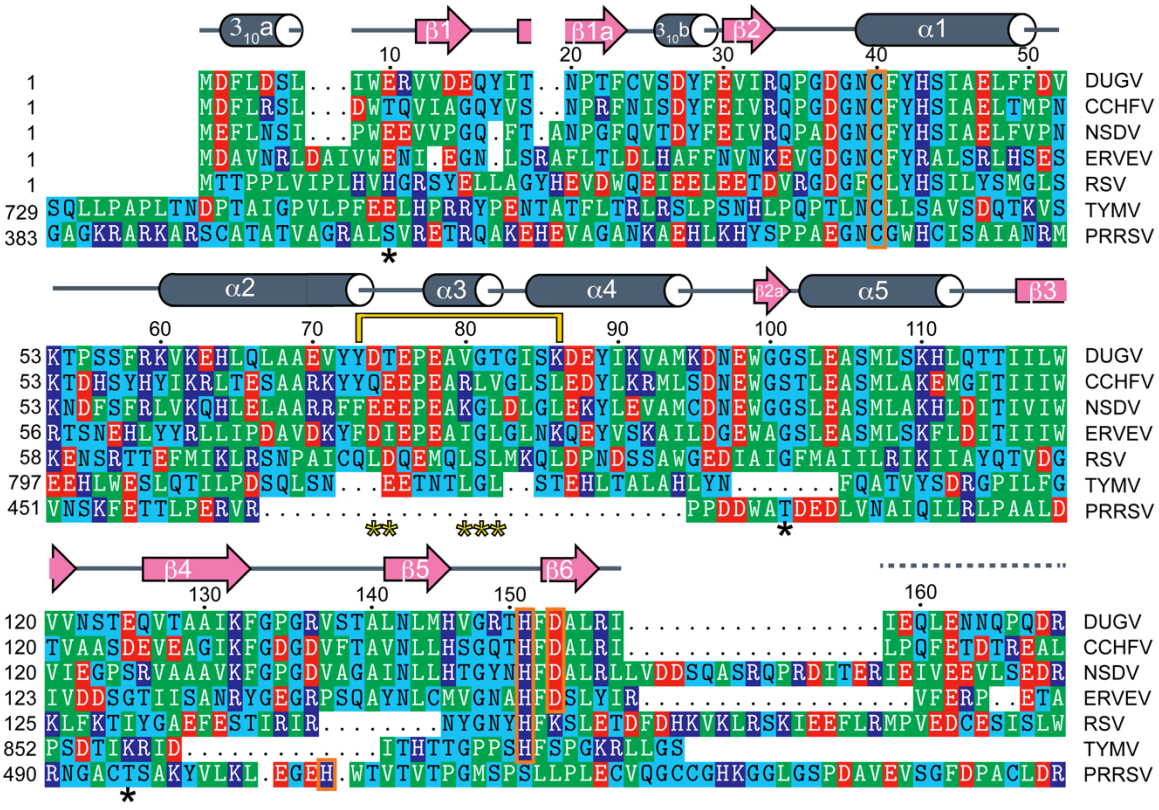

Figure 3.1. Sequence alignment of several viral OTU proteases. The vOTUs are from Dugbe virus (DUGV; GenBank accession no. AAB18834.1), Crimean-Congo hemorrhagic fever virus (CCHFV; GenBank accession no. AAQ98866.2), Nairobi sheep disease virus (NSDV; GenBank accession no. ACH99799.1), Erve virus (ERVEV; GenBank accession no. AFH89032), rice stripe virus (RSV; GenBank accession no. ABC68333), turnip yellow mosaic virus (TYMV; GenBank accession no. NP_663297.1), and porcine reproductive and respiratory virus (PRRSV; GenBank accession no. Q9WJB2). The secondary structure of DUG vOTU according to Defined Secondary Structure of Proteins (DSSP) is shown as gray cylinders (helical regions), pink arrows (β-sheets), and gray lines (loops). Hashed gray line represents residues for which electron density was not defined in the crystal structure. Breaks denote regions were DUG vOTU does not have residues. Asterisks represent amino acid residues chosen for site-directed mutation. Orange brackets indicate residues that are part of vOTUs' catalytic triad. A yellow bracket outlines residues involved in a backbone shift between CCHFV and DUGV.

Expression and production of vOTUs and Ub-Br3.

For vOTU enzymatic studies, *E. coli* strains harboring vOTUs from CCHFV, DUGV, ERVEV, and TYMV were grown at 37°C in 6 liters of Luria-Bertani broth containing 100 μg of ampicillin/mL until the optical density at 600 nm reached 0.6. Expression of the vOTU gene was induced by the addition of IPTG (isopropyl-β-D-thiogalactopyranoside) to a final concentration of 0.8 mM. The culture was further grown for 4 h at 37°C and then centrifuged at 6,000*g* for 10 min. The cells were collected and stored at -80°C until use. All vOTUs were purified according to the previously published protocol[(85)]. All final protein concentrations were determined from the absorbance at 280 nm using an experimentally determined extinction coefficient[(61)].

Truncated human Ub (1-75) was expressed according to previously established protocols with the exception that, after the IPTG induction, the culture was grown overnight at 18°C[(43, 60)]. *E. coli* BL21 (DE3)-Codon- Plus pellets containing Ub (1-75) were lysed with buffer C (25 mM HEPES [pH 6.8], 50 mM sodium acetate, 75 mM NaCl) augmented with 0.16% Triton X-100. The solution was then sonicated on ice at 30% power with pulses of 5-s durations for 10 min. Insoluble debris was removed by centrifugation at 17,000*g* for 45 min. The clarified extract was filtered with a 0.80-μm-pore-size filter and then poured over a chitin column pre-equilibrated with buffer C. The column was washed with three column volumes of buffer C, followed by resuspension in two column volumes of buffer C supplemented with 100mM sodium 2-mercaptoethanesulfonate (MESNA). The resuspension was rocked gently overnight at 4°C and eluted by filtration through a XK 26/40 GE column. The resulting Ub thioester

was then derivatized with 3-bromopropylamine hydrobromide (Ub-Br3) according to previously described methods[43, 60]. The purity of the Ub-Br3 was assessed by use of 10 to 20% Mini-Protean Tris-Tricine precast gels (Bio-Rad, CA).

Site-directed mutagenesis of the CCHF vOTU and DUG vOTU genes.

CCHF vOTU T10E, S101G, E128G, and E128T, as well as DUG vOTU E10T, G101S, T128E, and α3-chimera (D74Q/T75E/ V80R/G81L/T82V) protein mutants were created by using QuikChange site-directed mutagenesis according to the manufacturer's protocol (Agilent Technologies, Inc.). The resulting mutant plasmids were introduced into *E. coli* XL1-Blue Supercompetent cells by heat shock transformation and were then propagated, purified for sequence verification, and transformed into *E. coli* BL21 (DE3) cells for enzyme expression. The complete coding regions for all mutant enzymes were sequenced by GenScript, Inc., or Eton Bioscience, Inc.

Fluorescent vOTU deubiquitination and deISGylation assays.

All assays were performed in duplicate in buffer D (100 mM NaCl, 50 mM HEPES [pH 7.5], 0.01 mg of bovine serum albumin [BSA]/mL, 5 mM dithiothreitol [DTT]) using a Corning Costar half-volume black 96-well plate with a reaction volume of 50 μL. The rates of the reactions were observed using an Infinite M1000 series plate reader (Tecan, Inc.). Specifically, the increase in fluorescence (excitation λ, 360 nm; emission, 460 nm) of 7-amino-4-methylcourmarin (AMC) upon cleavage from Ub-AMC, human ISG15-AMC (hISG15-AMC) (Boston Biochem, MA), and ZRLRGG-AMC (Bachem) substrates was monitored for each of the vOTUs. The extinction coefficients for all three fluorescent substrates were determined by adding excess vOTU to various

concentrations of each substrate, and the reactions were allowed to run until completion. The resulting maximum fluorescence values were plotted to determine the slope and subsequently each substrate's extinction coefficient.

To calculate the turnover rates for 1 μM hISG15-AMC, 1 μM Ub-AMC, and 50 μM ZRLRGG-AMC of DUG vOTU, ERVE vOTU, and TYM vOTU, as well as mutants originating from DUG vOTU and CCHF vOTU, various enzyme concentrations were used. This was to account for the varied activities of different vOTUs toward their Ub and hISG15 substrates. For DUG vOTU and associated mutants, 2 μM, 4 nM, and 4 μM concentrations of enzyme were used against hISG15-AMC, Ub-AMC, and ZRLRGG-AMC, respectively. The enzyme concentrations for CCHF vOTU and associated mutants were the same concentrations as those of DUG vOTU with the exception of 20 nM enzyme being utilized to observe the cleavage of hISG15-AMC. Similarly, 4 nM ERVE vOTU was used to cleave Ub-AMC and hISG15-AMC, with 1 μM enzyme used to cleave 50 μM ZRLRGG-AMC. For TYM vOTU, 2.2, 1.2, and 4 μM concentrations of enzyme were used to cleave hISG15-AMC, Ub-AMC, and ZRLRGG-AMC, respectively.

To determine the DUG vOTU's V_{max} and K_M values for Ub-AMC, DUG vOTU's concentration was maintained at 4 nM enzyme while the Ub-AMC concentration was varied from 0 to 75 μM. To determine DUG vOTU's V_{max} and K_M values for hISG15-AMC, DUG vOTU's concentration was maintained at 2 μM enzyme, while the hISG15-AMC concentration was varied from 0 to 32 μM. For calculation of the V_{max} and K_M values for TYM vOTU, an enzyme concentration of 1.2 μM was used while the Ub-AMC concentration was varied from 0 to 65 μM, and an enzyme concentration of 2.2 μM was

used while the hISG15-AMC concentration was varied from 0 to 32 μM. ERVE vOTU's V_{max} and K_M values for Ub-AMC and hISG15-AMC were determined maintaining an enzyme concentration of 125 nM while the Ub-AMC concentration was varied from 0 to 51 μM, and an enzyme concentration of 4 nM was maintained while the hISG15-AMC concentration was varied from 0 to 5 μM. The initial rates were fitted to the Michaelis-Menten equation, $\nu = V_{max}/[1 / (K_M/[S])]$, using the Enzyme Kinetics module of SigmaPlot (v12.2; SPSS, Inc.). V_{max} was translated into k_{cat} using $k_{cat} = V_{max}/[E]$.

The vOTUs from CCHFV, DUGV, ERVEV, and TYMV turnover rates for di-Ub Förster resonance energy transfer (FRET) linkage substrates K11, K48, and K63 (Boston Biochem, MA) at 1 μM were determined by monitoring the increase in fluorescence (excitation λ, 544 nm; emission, 572 nm) resulting by the separation of a FRET TAMRA/QXL pair. The cleavage of three commercially available FRET TAMRA/QXL pair configurations per K48 and K63 di-Ub linkage FRET substrates was assessed. Each di-Ub FRET substrate at 1 μM was evaluated against an enzyme concentration of 2 nM (CCHF and DUG vOTU), 125 nM (ERVE vOTU), or 500 nM (TYM vOTU). For the K11 di-Ub FRET substrate, enzyme concentrations of vOTUs from CCHFV (100 nM), DUGV (100 nM), ERVEV (2.6 μM), TYMV (20 nM) were used.

Deubiquitinating gel shift assay.

Poly-Ub linked by the different isopeptide bonds (K6, K11, K27, K29, K33, K48, and K63), as well as the N-terminal peptide bond (linear), were purchased from Boston Biochem, MA. Dimeric-Ub substrates (10 μM) were incubated with each vOTU (4 nM CCHF vOTU, 4 nM DUG vOTU, 100 nM ERVE vOTU, and 6 μM TYM vOTU) in

reaction buffer F (100mM NaCl, 50mM HEPES [pH 7.5], 2mM DTT) at 37°C. The reactions were stopped at various times of 1 h by mixing 9 µL of each reaction with 2× sodium dodecyl sulfate-Tricine sample buffer, followed by boiling at 95°C for 5 min. The results were visualized on 10 to 20% Mini-Protean Tris-Tricine precast gels (Bio-Rad). For vOTU cleavage of trimeric K48 and K63 linkages, 20 µM tri-Ub substrates were tested and analyzed in the same manner as the di-Ub.

DUG vOTU-Ub complex formation and crystallization.

DUGV vOTU was combined with Ub-Br3 in equal molar ratios, incubated at 37°C for 2 h and left overnight at 4°C. Complex (DUG vOTU-Ub) formation was monitored using 10 to 20% Mini-Protean Tris-Tricine precast gels. DUG vOTU-Ub was dialyzed overnight against 1 liter of buffer G (100 mM NaCl, 50 mM Tris-HCl [pH 8.0]) and then purified using a GE Mono-Q column with a linear gradient of buffer G to buffer H (1 M NaCl, 50 mM Tris-HCl [pH 8.0]). Fractions were pooled according to the chromatogram, loaded onto an AP-1 (Waters) column packed with Superdex-75 resin pre-equilibrated with buffer I (150 mM NaCl, 5 mM HEPES [pH 7.4], 1 mM TCEP-HCl), and eluted at a flow rate of 1.0 mL/min. Resulting DUG vOTU-Ub was concentrated in a GE Vivaspin 6 10-kDa MWCO concentrator and filtered using a 0.22-µm-pore-size Costar spin filter. The initial crystal conditions for DUG vOTU-Ub were determined from high-throughput screening of Qiagen Classics I and II screens in a 96-well sitting drop format using an Art Robbins Phoenix robot. Drops contained 0.4 µL of protein solution and 0.4 µL of precipitate with a 100-µL reservoir volume. Initial screening resulted in several hits; however, a solution containing 0.25 M $LiSO_4$, 0.10 M

Bis-Tris (pH 5.5), and 29% PEG 3350 produced the most viable crystals. These crystals were optimized using the Additive HT Screen from Hampton Research. Final DUG vOTU-Ub crystals were obtained through vapor diffusion using a 500-µL reservoir with 4-µL hanging drops mixed 1:1 with protein solution and 0.25 µL of 40% (vol/vol) 1,3-butanediol.

Data collection and X-ray structural determination of DUG vOTU-Ub.

An X-ray data set was collected using a crystal mounted onto a nylon loop flash frozen in liquid nitrogen. The frozen crystal was mounted under a stream of dry N_2 at 100 K. A DUG vOTU-Ub data set with resolution to 2.85 Å was collected at the advanced light source (ALS) beam line 4.2.2 at 1.00 Å with a NOIR-1 MBC detector (NOIR-1). X-ray images were indexed, processed, integrated, and scaled using HKL2000[(62)], and phases were determined and refined using Phaser[(5)]. An initial phase solution was elucidated using a homology model based on the CCHF vOTU-Ub structure 3PRP for molecular replacement using Phaser[(5)]. The structure was refined using iterative cycles of model building and refinement using COOT and REFMAC, respectively[(5, 95)]. Water molecules were added to $2F_o$-F_c density peaks of $>1\ \sigma$ using the Find Water COOT program function. The final model was checked for structural quality using the CCP4 suite programs Procheck and Sfcheck. The data refinement statistics are shown in Table 3.1. Structure factors and coordinates have been assigned PDB code 4HXD.

	Dugbe-Ub
Data Collection	
Space Group	C2
Unit Cell Dimensions	
a, b, c (Å)	113.5, 40.0, 114.2
β (°)	97.3
Resolution (Å)	50.0 – 2.85
No. Reflections Observed	38,714
No. Unique Reflections	11,887
R_{merge} (%)[a]	5.8 (14.1)*
I/σI	18.4 (6.1)*
% Completeness	95.8 (79.0)*
Refinement	
Resolution Range	50 – 2.85
No. Reflections in Working Set	11,301
No. Reflections in Test Set	567
R_{work} (%)[b]	21.0
R_{free} (%)[b]	27.8
RMS deviation:	
Bond Lengths (Å)	0.01
Bond Angles (°)	1.2
Protein / Water Atoms	3706 /46
Average B-Factors (Å^2)	
Total	20.8
Protein	20.8
Water	12.9
Ions	41.6

* The last resolution shell is shown in parentheses. [a] $R_{merge}=\Sigma_h\Sigma_I |I_I(h) - <I(h)>| / \Sigma_h\Sigma_i I_I(h)$, where $I_I(h)$ is the i^{th} measurement and $<I(h)>$ is the weighted mean of all measurements of $I(h)$. [b] R_{work} and $R_{free} = h(|F(h)_{obs}| - |F(h)_{calc}|) / h|F(h)_{obs}|$ for reflections in the working and test sets, respectively. R.m.s., root mean square.

Table 3.1. Crystallographic data for DUG vOTU-Ub complex

Results

Comparison of nairovirus vOTUs specificity for Ub and ISG15

To assess whether nairovirus vOTUs have a conserved specificity for both Ub and hISG15 conjugates, vOTUs from CCHFV, DUGV, and ERVEV were evaluated for their ability to remove 7-amino-4-methylcourmarin (AMC) from the C terminus of 1 μM Ub-AMC, hISG15-AMC, or a peptide that contains the last five highly conserved amino of hISG15 and Ub (ZRLRGG-AMC; Figure 3.2). In addition, the recently identified vOTU from TYMV was evaluated along side the nairovirus vOTUs to determine whether the activity and specificity of negative single-stranded nairoviruses for these substrates is potentially similar to a vOTU from a positive single-stranded RNA virus. Initially, the four vOTUs were assessed against the ZRLRGG-AMC conjugate to observe their affinity for the minimal recognition component these proteases use to identify Ub and hISG15 (Figure 3.2a). The vOTUs of ERVEV and TYMV have a substantially more robust activity toward this substrate than those of CCHFV and DUGV (Figure 3.2a). As observed in our previous study, CCHF vOTU cleaves the Ub-AMC 5-fold faster than its

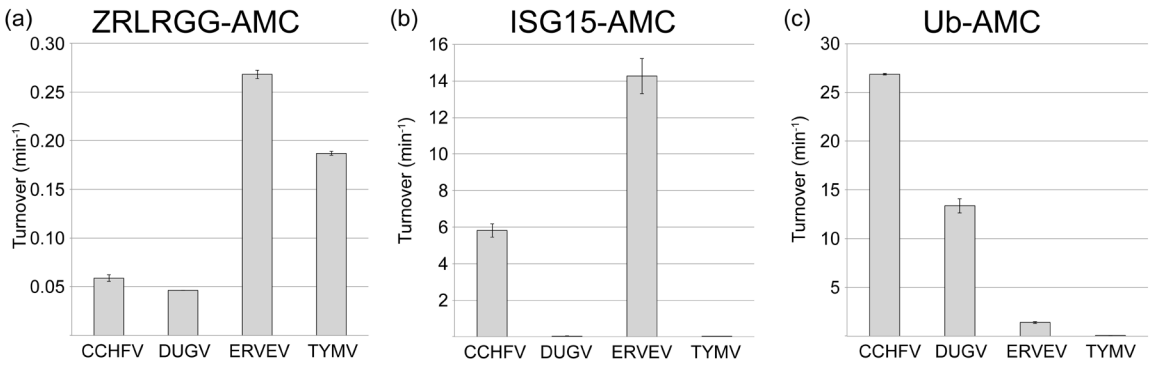

Figure 3.2. vOTU cleavage of peptide, Ub, and hISG15 AMC conjugates. The cleavage activities of vOTUs from CCHFV, DUGV, and TYMV for 50 μM ZRLRGG-AMC (a), 1 μM Ub-AMC (b), and 1 μM hISG15-AMC (c) were determined. Error bars represent standard deviations from the average.

hISG15-AMC counterpart[85]. Unexpectedly, the other three vOTUs have widely divergent activities from CCHF vOTU toward these two substrates (Figure 3.2b and c). Specifically, CCHF vOTU cleaves Ub-AMC with a turnover rate twice that of DUG vOTU, which is the second most active vOTU toward this substrate. However, DUG vOTU possesses 200-fold less activity toward hISG15-AMC, suggesting that every vOTU may not be able to robustly cleave hISG15 conjugates. Intriguingly, the vOTU from ERVEV exhibits the reverse specificity, overwhelmingly preferring hISG15 to Ub. Not surprisingly, vOTU from the plant virus TYMV lacks any appreciable activity for hISG15, for which a plant homolog has yet to be identified. However, its 3-orders-of-magnitude-lower activity for Ub-AMC was interesting since there are only three amino acid differences, which are not located on the surface, between human Ub and Ub originating from the yellow turnip, *Brassica napobrassica*. Overall, TYM vOTU has 6-fold higher activity for ZRLRGG-AMC versus Ub-AMC and 30-fold more than hISG15-AMC.

To explore the complexities in the affinities of vOTUs for Ub and hISG15, the K_M and k_{cat} values of the four vOTUs were ascertained for these substrates (Table 3.2). DUG vOTU shows a slightly higher k_{cat} than that of CCHF vOTU for Ub-AMC but with a substantially increased K_M. These results suggest that DUG vOTU can process Ub-

	Ub-AMC			ISG15-AMC		
	k_{cat} (min^{-1})	K_M (M)	k_{cat}/K_M (min^{-1} M^{-1})	k_{cat} (min^{-1})	K_M (M)	k_{cat}/K_M (min^{-1} M^{-1})
CCHFV§	208 ± 15	3.8 ± 0.8 x 10^{-6}	5.5 ± 1.2 x 10^{7}	32.5 ± 3.0	2.2 ± 0.5 x 10^{-6}	1.5 ± 0.36 x 10^{7}
DUGV	306 ± 13	35.7 ± 3.2 x 10^{-6}	8.6 ± 0.86 x 10^{6}	0.244 ± 0.014	5.21 ± 0.9 x 10^{-6}	4.7 ± 0.85 x 10^{4}
ERVEV	55.6 ± 3.1*	64.9 ± 5.6 x 10^{-6}*	8.6 ± 0.88 x 10^{5}	18.5 ± 0.98	0.66 ± 0.14 x 10^{-6}	2.8 ± 0.61 x 10^{7}
TYMV	1.79 ± 0.094*	70.2 ± 6.0 x 10^{-6}*	2.6 ± 0.3 x 10^{4}	0.092 ± 0.007	13.5 ± 2.3 x 10^{-6}	6.1 ± 1.27 x 10^{3}
§ Data from Capodagli *et al. J. Virol* (2011) **85**: 3621-3630 *Saturating conditions were not met						

Table 3.2. **Kinetic characterization of vOTUs**

AMC at rates beyond those of CCHF vOTU but appears to possess a weaker affinity for the substrate leading it to have a 6-fold reduction in Ub-AMC catalytic efficiency. For hISG15-AMC, DUG vOTU possesses 3 orders of magnitude lower k_{cat} and double the K_M for this substrate compared to CCHF vOTU. As a result, DUG vOTU's catalytic efficiency for hISG15 approaches that of the TYM vOTU, a vOTU that has likely not evolved to process this substrate. TYM vOTU's affinity for Ub-AMC does not appear to be particularly robust either, with saturating conditions of the Ub-AMC substrate beyond the maximal substrate concentrations achievable. In contrast to both the vOTUs from TYMV and DUGV, ERVE vOTU possesses a high level of ability to cleave hISG15 conjugates with a k_{cat} within the same magnitude and a K_M that was half that of CCHF vOTU. This translates into ERVE vOTU having the highest catalytic efficiency for hISG15 of any known to vOTU. Surprisingly, ERVE vOTU proves to be a poor deubiquitinating enzyme by nairovirus standards, to the point where saturating concentrations of Ub-AMC are beyond the maximal substrate concentrations currently achievable. Using the data available would suggest at least a 4-fold decrease in Ub-AMC k_{cat} compared to CCHF vOTU, as well as a K_M that is 2-fold that for DUG vOTU and an order of magnitude compared to CCHF vOTU.

Poly-Ub linkage specificity of nairovirus vOTUs

Since host cellular proteins are found to be bound to chains of ubiquitin (poly-Ub), the vOTUs of DUGV, CCHFV, and ERVEV were assessed for their ability to cleave the eight different linkage types of poly-Ub, K6, K11, K27, K33, K48, K63, and linear, side by side. In addition, TYMV vOTU was similarly evaluated to observe

whether there was a potentially conserved preference among divergent viral families. With the vOTUs of DUGV and CCHFV exhibiting robust ability to separate Ub conjugates, only nanomolar quantities were necessary to observe poly-Ub cleavage within a 60-min time frame. Conversely, vOTUs from ERVEV and TYMV, which have limited activity toward Ub conjugates, require substantial quantities of protease. In the case of TYM vOTU, almost equal molar ratios were required to observe substantial cleavage (Figure 3.3). Evaluation of the ability for the four vOTUs to sever the eight linkage forms between two Ub monomers unexpectedly revealed that all four vOTUs possess a relatively clear preference for K6 poly-Ub linkages. Also, between vOTUs of DUGV and CCHFV that were assessed at the same protease concentration, DUG vOTU appears to process K6 poly-Ub linkages at a faster rate. Interestingly, the four vOTUs have a mixed preference for their secondarily preferred poly-Ub linkage substrate. As was observed previously, CCHF vOTU appears to favor K63 poly-Ub linkage[(85)]. However, the other three vOTUs seem to favor K48 poly-Ub linkages. In addition to severing K6, K48, and K63 poly-Ub linkages, all four vOTUs shared a robust preference for K11 poly-Ub linkages. The remaining K27, K29, K33, and linear poly-Ub linkages proved to be a relatively poor substrate for each of the four vOTUs to various degrees. CCHF vOTU appears to be the most selective of the four vOTUs assessed, only preferring the aforementioned K6, K63, K48, and K11 poly-Ub linkages (Figure 3.3). Minor relative activities toward K33 and K27 poly-Ub linkages were observed for the remaining three vOTUs, with ERVE vOTU possibly having some extremely low relative preference toward K29 poly-Ub linkages.

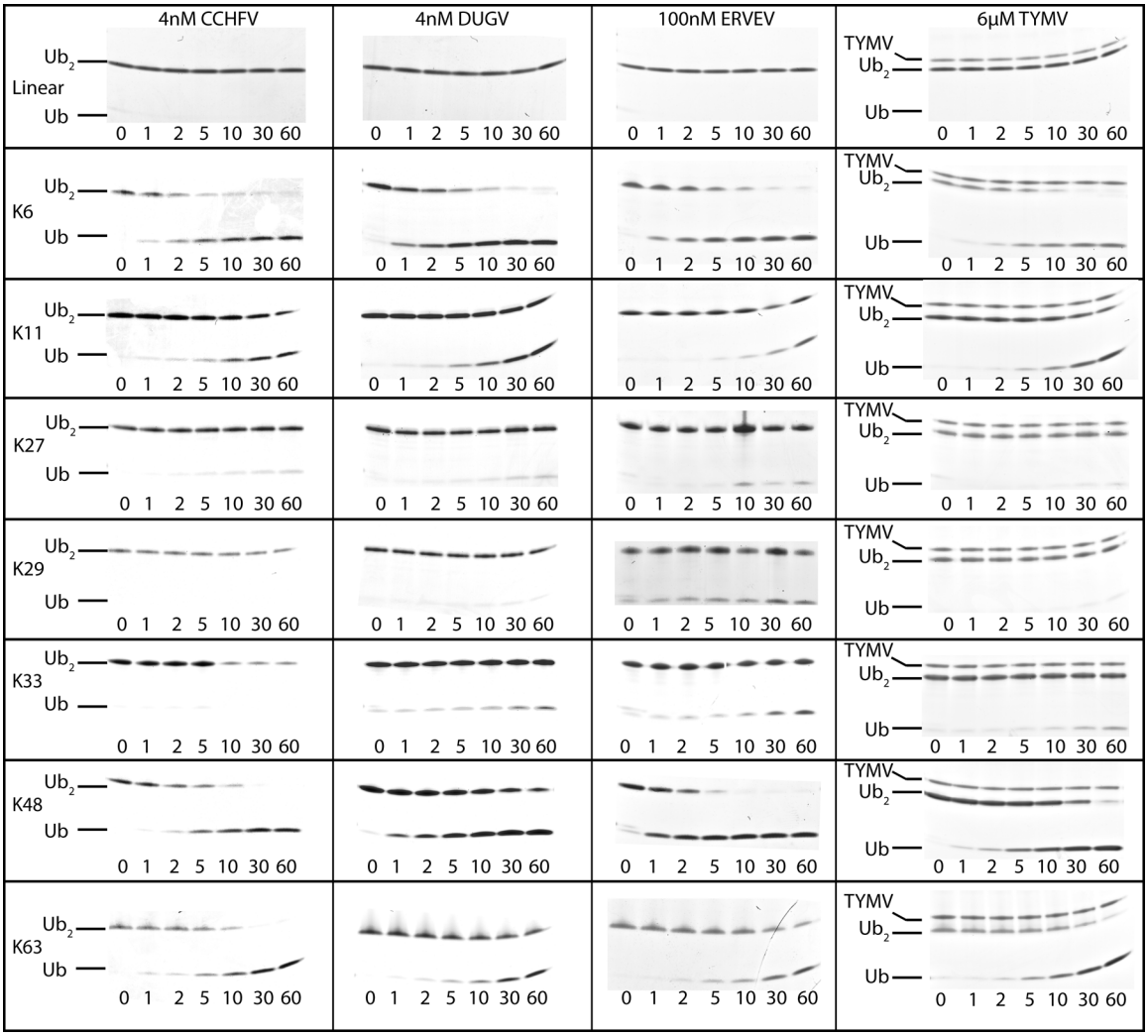

Figure 3.3. Gel shift assay of vOTU poly-Ub linkage specificity. A 10 μM concentration of each di-Ub linkage was incubated with either 4 nM CCHFV, 4 nM DUGV, 100 nM ERVEV, or 6 μM TYMV at 37°C for an hour with samples taken at the indicated time points. The samples were heat inactivated at 95°C for 5 min and then run on a 10 to 20% Mini-Protean Tris-Tricine precast gels (Bio-Rad). The bands were visualized by staining with Coomassie blue.

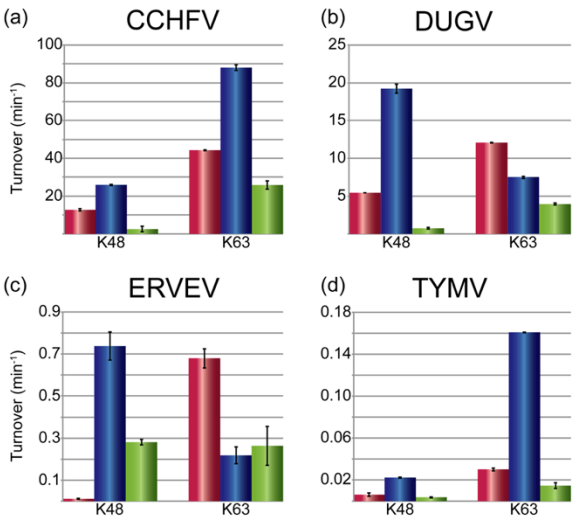

Figure 3.4. Evaluation of Di-Ub FRET Pair Positions. 1uM of each TAMRA/QXL FRET pair attached at different positions on each Ub in the dimer was tested with (a) CCHFV, (b) DUGV, (c) ERVEV, and (d) TYMV. Position 1 is shown in red, Position 2 in blue, and Position 3 in green.

Since the relative preference of vOTUs from CCHFV, DUGV, ERVEV, and TYMV appear to diverge for K63 and K48 poly-Ub linkages, a quantitative approach was used to understand the extent of the differences for these two substrates among these vOTUs. Specifically, the increase in fluorescence upon the vOTU-facilitated separation of a TAMRA/QXL FRET pair located between two Ub molecules with either K48 or K63 linkages was examined. To minimize the possibility of FRET pair interference with vOTU-Ub interactions, separation of three different FRET pair configurations for K48 and K63 FRET substrates were observed using vOTUs from CCHFV, DUGV, ERVEV, and TYMV (Figure 3.4). The rate for FRET pair configuration that is cleaved most efficiency by each vOTU for K48 and K63

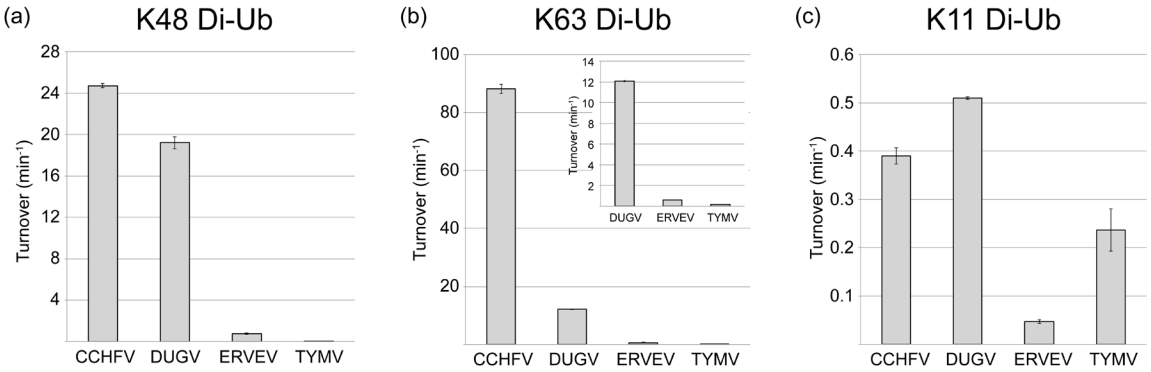

Figure 3.5. vOTU preference for FRET poly-Ub linkage substrates. (a to c) vOTU cleavage activity for K48-linked (a), K63-linked (b), or K11-linked di-Ub (c). Turnover values were determined based on the increase in emission upon cleavage of 1 μM di-Ub in the presence of the vOTU from CCHFV, DUGV, and TYMV. Error bars represent standard deviations from the average.

FRET substrates were compared side by side (Figure 3.5a to c). Although CCHF vOTU and DUG vOTU demonstrate comparable turnover rates for K48 poly-Ub linkages, CCHF vOTU severs K63 poly-Ub linkages at a rate of 7-fold that of DUG vOTU. Also, CCHF vOTU's turnover rate for the K63 FRET substrate is 3.5-fold elevated over that of Ub-AMC. DUG vOTU exhibited a similar phenomenon for its preferred K48 FRET substrate. This trend of K48 and K63 specificity was also present with the larger tri-Ub substrates (Figure 3.6). Not surprisingly, TYM vOTU and ERVE vOTU cleaved these poly-Ub linkage substrates poorly, with the two vOTUs having 2 to 3 orders of magnitude less activity than vOTUs from CCHFV and DUGV. In addition to K63 and K48 FRET substrates, a K11 FRET substrate was subsequently used to gauge the cleavage rates of the four vOTUs for K11 poly-Ub linkages. These results generally mirrored those observed in the separation of unlabeled poly-Ub linkages substrates and were all significantly below those observed for cleavage of Ub-AMC (Figure 3.3 and 3.5c).

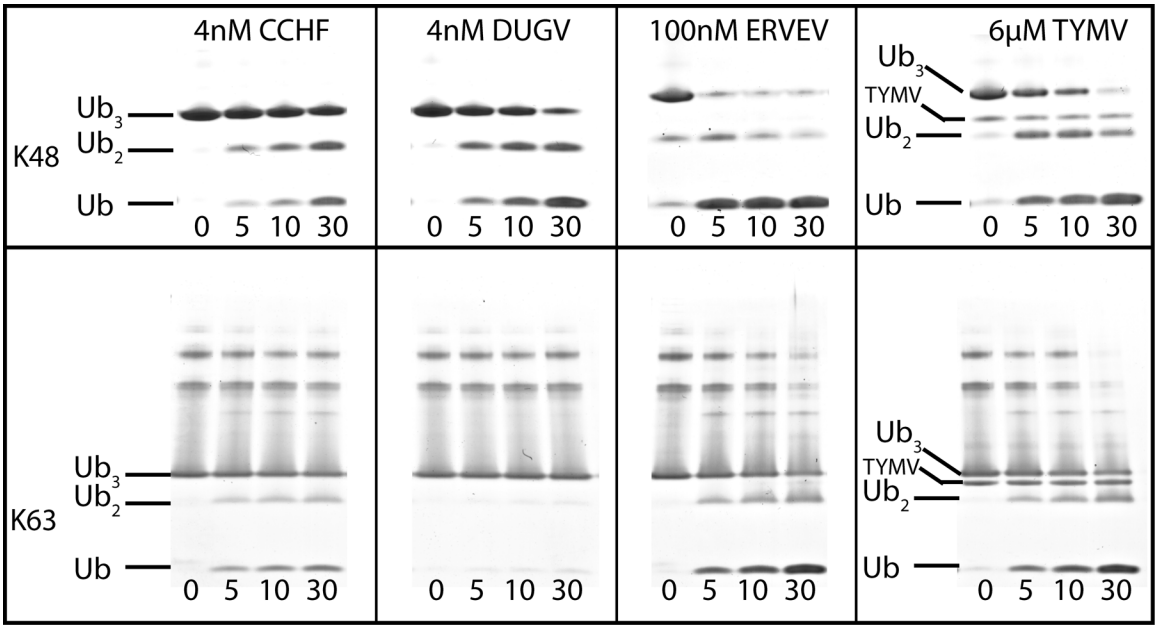

Figure 3.6. Poly-Ub linkage gel shift assay. A 20 μM concentration of each tri-Ub linkage was incubated with either 4 nM CCHF vOTU, 4 nM DUG vOTU, 100 nM ERVE vOTU, or 6 μM TYM vOTU at 37°C for an hour with samples taken at the indicated minute time points. The samples were heat inactivated at 95°C for 5 min and then run on a 10 to 20% Mini-Protean Tris-Tricine precast gels.

X-ray crystallographic elucidation of DUG vOTU-Ub complex

Previous structural elucidation of CCHF vOTU by others and our lab suggested that CCHF vOTU's ability to cleave hISG15, which was unexpected for an OTU, was primarily the result of the orientation in which CCHF vOTU bound to its Ub or hISG15 substrate[84, 85, 96]. This suggested that vOTUs might, as a class, possess deISGylating activity. However, although the vOTUs from DUGV and ERVEV have high amino acid similarity to CCHF vOTU, 79 and 68%, respectively, a significant divergence in their preference between Ub and hISG15 conjugates was observed. To investigate the potential structural origins of these partialities, a covalent complex was formed between DUG vOTU and a bromolyated C-terminal Ub. Subsequently, the DUG vOTU-Ub complex was screened against several suites of commercially available precipitant screens and further optimized via an additive screen resulting in a set of crystal conditions. The initial condition contained PEG 3350, Bis-Tris (pH 5.5), and lithium sulfate and was optimized with 1,3-butanediol, yielding a 2.85 Å data set in a C2 space group (Table 3.1).

Structural comparison of DUG vOTU and CCHF vOTU complexes

Comparison between the structures of DUG vOTU and CCHF vOTU in complex with Ub revealed that the two complexes adopted a comparable fold. Similar to CCHF vOTU, DUG vOTU is comprised of a core of seven β-sheets flanked by five α-helices and three 3_{10}-helices with an additional antiparallel sheet, β2a, formed between residues 100 to 102 of the protease and residues 73 to 75 of the Ub (Figure 3.7a and b). In addition, DUG vOTU appears to accommodate Ub in the same manner as CCHF vOTU,

suggesting that DUG vOTU employs no overtly tertiary structure rearrangement to account for its partiality between Ub and hISG15 (Figure 3.7c).

Despite their similarities, the overlay of DUG vOTU and CCHF vOTU bound to either Ub or hISG15 does highlight two variances between the vOTUs (Figure 3.7d)[85, 96]. One is the β3-4 loop, which encompasses DUG vOTU residues 121 to 126. This loop

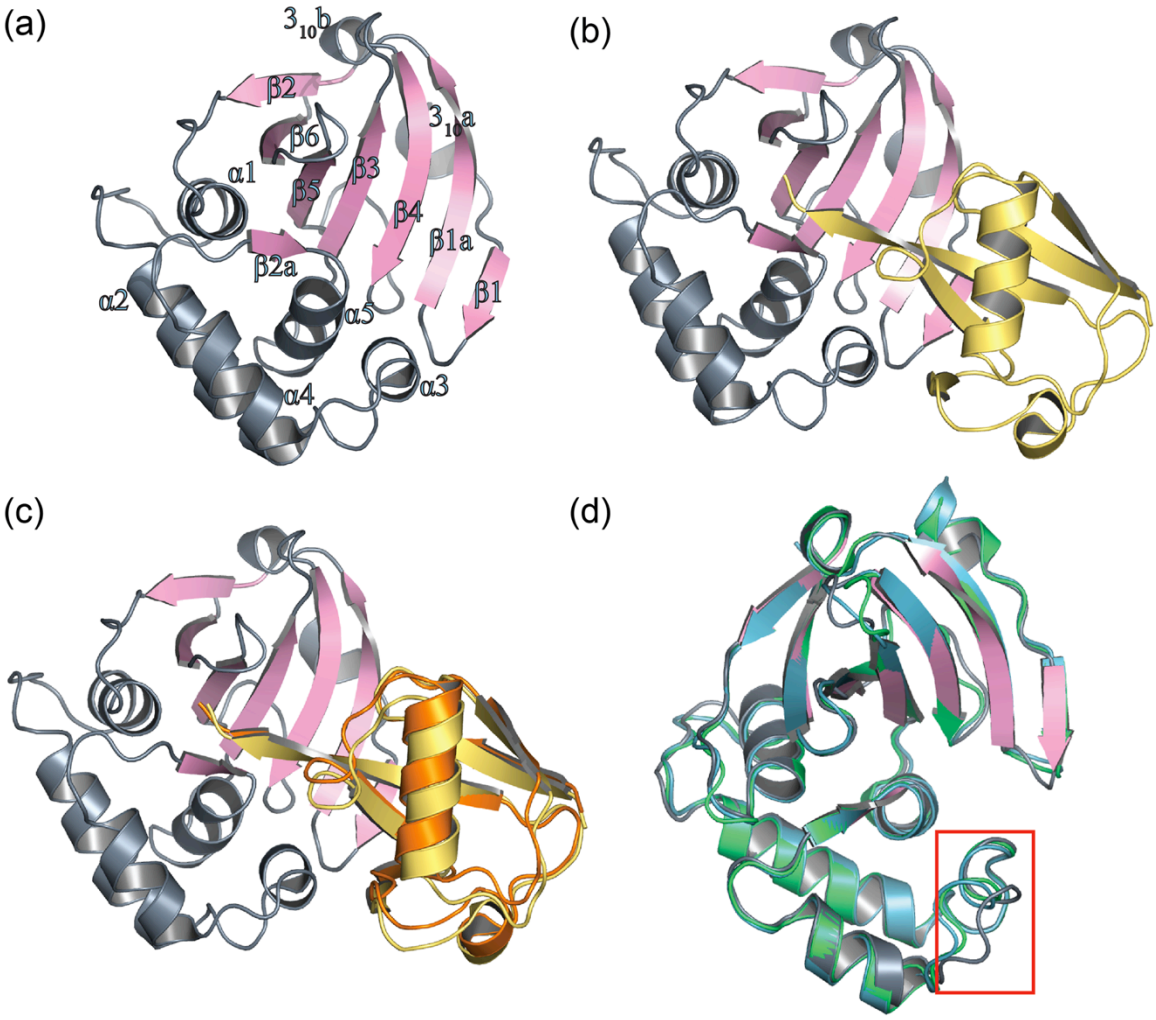

Figure 3.7. Diagram representation of DUG vOTU-Ub. (a) DUG vOTU monomer labeled and colored according to secondary structure: helices and loops are indicated in gray, and β-sheets are indicated in pink. (b) Complex of DUG vOTU rendered as in panel a, and Ub is rendered in yellow. (c) Overlay of DUG vOTU-Ub complex colored as in b, with Ub bound to CCHF vOTU (orange). (d) Overlay of DUG vOTU, CCHF vOTU bound to Ub (green, PDP code 3PRP), and CCHF vOTU bound to hISG15 (teal, PDB code 3PSE) DUG vOTU is as in panel a, with the α3 helix of each structure rendered as loops and boxed in red.

has a higher than average B-factor in both structures of vOTUs from DUGV and CCHFV and lacks any direct interaction with other parts of the vOTU, or its bound substrate, implying that the divergence observed is a result of inherent loop flexibility. This is not the case with the second dissimilar region that contains DUG vOTU residues 73 to 85, which comprises its α3 helix and surrounding residues. A clear divergence of this region in DUG vOTU can be observed compared to that of either comparable regions in CCHF vOTU-Ub or CCHF vOTU-ISG15 structures (Figure 3.7d). Interestingly, this region forms a considerable interface with Ub in the DUG vOTU structure, as well as one between CCHF vOTU bound to Ub and hISG15 (Figure 3.7c). Two driving forces readily appear to be responsible for the divergence between the two proteases' α3 helix. One is that DUG vOTU has a glycine at position 81, similar to many other vOTUs, instead of a leucine as in CCHF vOTU. The glycine results in breaking the α3 helix secondary structure, making DUG vOTU's α3 helix shorter than the one found in CCHF vOTU. The second appears to be the amino acid sequence of this region. CCHF vOTU possesses not only a leucine at position 81 but also a valine at position 82. The hydrophobic side chains of these two amino acids appear to insert into hydrophobic patches on Ub and internally on CCHF vOTU, respectively (Figure 3.8a).

Primary structural origins of Ub and ISG15 specificity between vOTUs of DUGV and CCHFV

In order to examine the influence of the α3 helix on vOTUs' ability to cleave hISG15 conjugates, several positions within DUG vOTU—Asp74, Thr75, Val80, Gly81, and Thr82—were mutated to their corresponding residues in the CCHF vOTU. The

resulting DUG vOTU α3 helix chimera has comparable activity to the wild-type DUG vOTU enzyme for the small peptide ZRLRGG-AMC, suggesting that the mutations did not impact catalytic activity. As expected, the DUG vOTU α3 helix chimera possesses a relatively significant increase of 150% activity for hISG15-AMC. Interestingly, however, the DUG vOTU α3-chimera's ability to cleave the Ub-AMC conjugate decreases significantly, suggesting other primary structural elements are necessary to confer robust deISGylating activity (Figure 3.9d to f). One such region might include Glu128, which in CCHF vOTU forms hydrogen bonds with hISG15's Asn89 and Lys90 (Figure 3.8b). However, these bonds are absent in DUG vOTU because the glutamate is replaced by a threonine. Introduction of the T128E mutation in DUG vOTU increases the activity toward Ub-AMC by 110%, hISG15-AMC by almost 2,000%, and ZRLRGG-AMC by 160%. Conversely, replacement of this glutamate in CCHF vOTU to a threonine resulted in a drop in activity of 40, 75, and 25% for Ub-AMC, hISG15-AMC, and ZRLRGG-AMC, respectively. In addition, a strain of CCHFV, UG3010, has been isolated from a patient in Uganda that contains a glycine polymorphism at position 128[(97)]. The introduction of this residue resulted in a mutant that followed the same pattern as the threonine mutation but with a greater effect. These results reveal the influence position 128 plays in determining specificity and activity within vOTUs (Figure 3.9a to c).

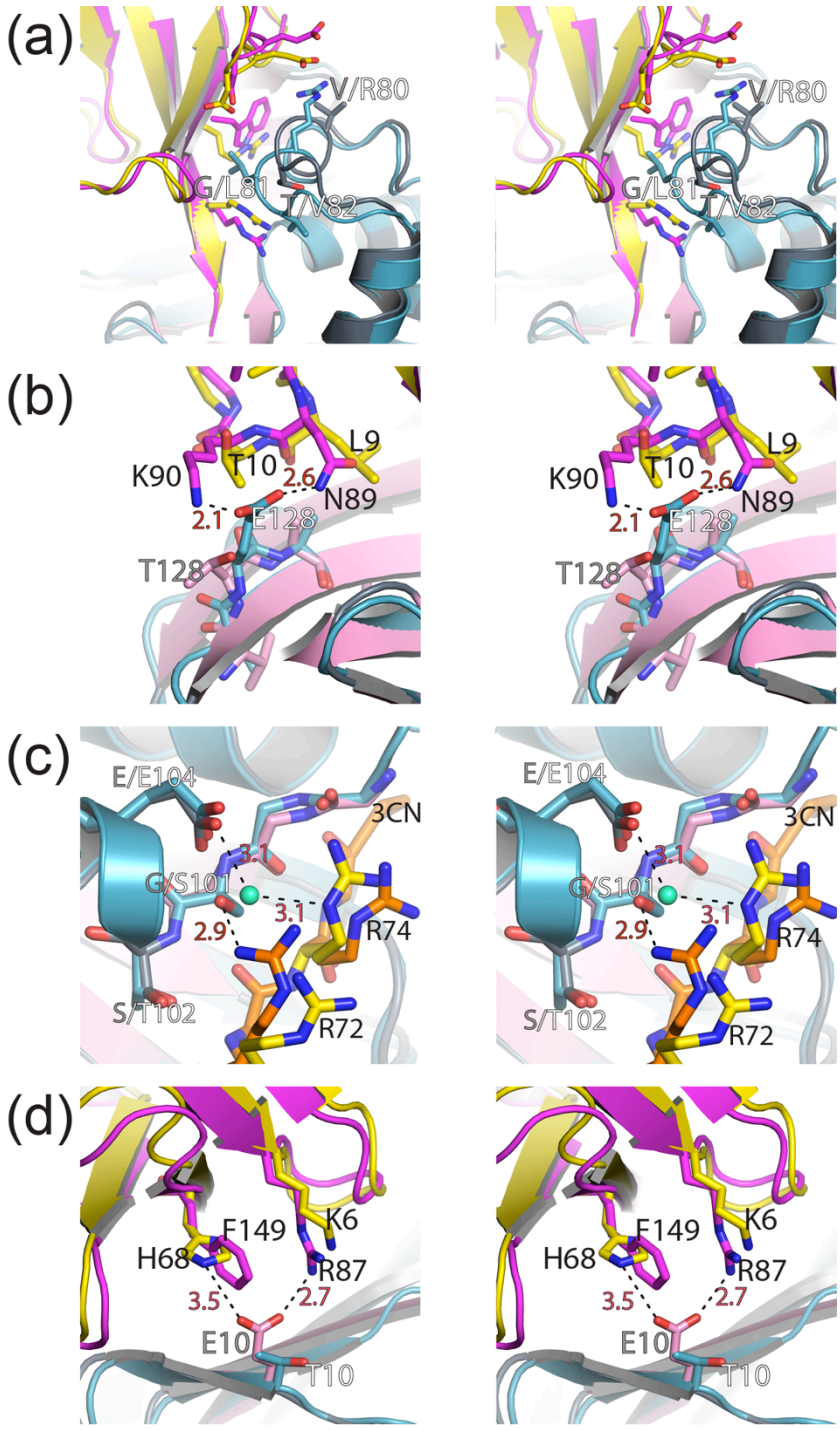

Figure 3.8. Locations of selective mutagenesis in vOTUs of CCHFV and DUGV. Wall-eyed stereo views of the interactions between DUG vOTU (gray/pink) and CCHF vOTU (teal) with Ub (yellow) and hISG15 (magenta) for the α3-chimera (a) and residues 128 (b), 100 to 102 (c), and 10 (d) are shown. Gray labels indicate CCHF vOTU residues, white labels indicate DUG vOTU residues, black labels indicate Ub and hISG15 residues, and red labels and dashed lines indicate distances. All of the distances are measured in angstroms.

Beyond position 128 in the vOTU structures of CCHFV and DUGV, position 101 was identified as a potential key residue. The serine at this position in the structure of CCHF vOTU partially comprises β2a that forms an antiparallel β-sheet with Ub. In addition, Ser101 in CCHF vOTU also forms key H-bonds with the Ub arginine residues 72 and 74 side chains. However, this position is filled by a glycine in DUG vOTU, potentially impeding DUG vOTU's ability to interact with its Ub and hISG15 substrates (Figure 3.8c). When CCHF vOTU's Ser101 was mutated to glycine, an expected drop in activity toward all assessed substrates of 60% was found. Unexpectedly, when Gly101 in DUG vOTU was mutated to serine, a reduction in activity by 90% was noticed for all substrates, while also resulting in a lower protein expression (data not shown). In vOTUs from DUGV, NSDV, and ERVEV, residue 101 is glycine and 102 is serine, whereas CCHF vOTU has a serine and threonine at these positions. Upon closer examination of CCHF vOTU's Thr102, it appears to be twisted in relation to the corresponding residue in DUGV via a surrounding hydrophobic environment created by Ile118, Ile131, and Phe133. This twist results in fixing the orientation of Ser101 in manner that the side chain points toward CCHF vOTU's bound substrate.

Unlike the structurally revealed differences in the vOTUs of CCHFV and DUGV that appear to limit DUG vOTU's ability to cleave either Ub or hISG15, DUG vOTU possesses at least one interaction that enhances deubiquitinating activity absent in CCHF vOTU. Specifically, DUG vOTU's Glu10 forms hydrogen bonds to His68 in Ub and is within hydrogen bonding range of Arg87 in hISG15 (Figure 3.8d). Not surprisingly, alteration of Glu10 to threonine in DUG vOTU causes decreases of 75 and 60% in Ub-

AMC and hISG15-AMC activity, while not affecting the overall catalytic activity of the enzyme. Also, when the T10E mutation was introduced into CCHF vOTU an increase of 50% activity toward Ub-AMC is observed.

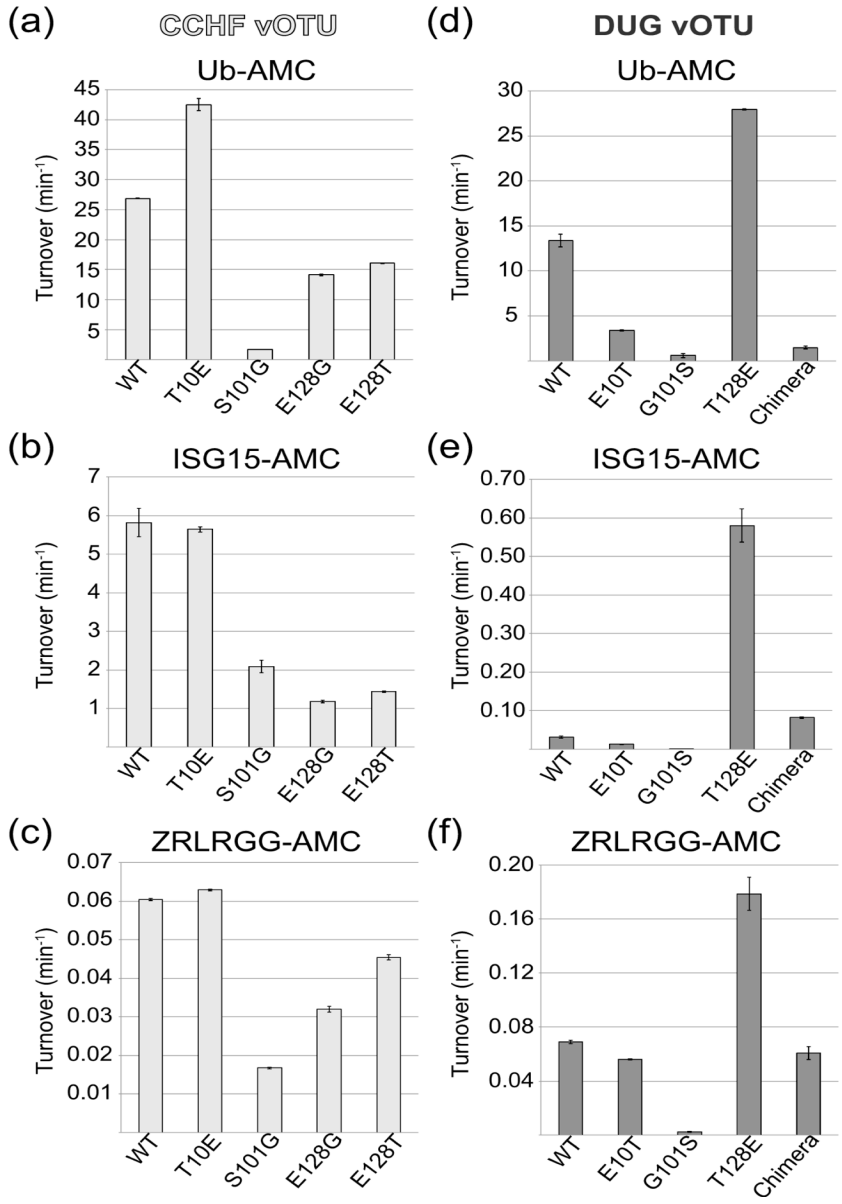

Figure 3.9. Effects of vOTU mutagenesis on vOTU activity toward peptide, Ub, and hISG15 AMC. The cleavage activity of mutants of CCHF vOTU (light gray) or DUG vOTU (dark gray) were determined at 1 μM against 1 μM Ub-AMC (a and d), 1 μM hISG15-AMC (b and e), or 50 μM ZRLRLGG-AMC (c and f). Error bars represent standard deviations from the average.

Discussion

Structural origins of nairovirus vOTU substrate specificity

The broad divergence in specificity observed between nairovirus vOTUs appears to originate predominantly from their primary structure differences. This is based on the conserved β-sheet and α-helix tertiary structural scaffold of vOTUs from DUGV and CCHFV, their sequence similarity with other nairovirus vOTUs, and the conserved manner in which Ub is bound to these two vOTUs. In addition, the DUG vOTU-Ub structure implies that although the 30° twist observed between the nairovirus vOTUs and bound Ub and other OTU superfamily members is conserved, it does not necessarily imply that a nairovirus vOTU may process ISG15 conjugates, at least not human ones[43, 85, 98]. Several key amino acids have been implicated in affecting CCHF vOTU substrate specificity. Specifically, mutation of Q16R and P77D were shown to ablate CCHF vOTU affinity for Ub and hISG15, respectively[84, 96]. However, in spite of these residues being conserved in many nairoviruses, DUG vOTU still demonstrates solely deubiquitinating activity illustrating that these conserved sites do not solely indicate substrate preference. Through the CCHF vOTU-Ub and DUG vOTU-Ub structures, plus selective cross mutagenesis between vOTUs from CCHFV and DUGV, the affinity of nairovirus vOTUs for Ub or hISG15 appears to be largely synergistic. Specifically, the sequence compositions within the α3 helix along with additional favorable amino acids, such as Glu128, or other key positions, appear necessary to confer substantial activity toward hISG15 between vOTUs from DUGV and CCHFV. Also, residues such as Thr102 in CCHF vOTU, which do not directly interact with Ub or hISG15, seem necessary for the

positive influence of serine at the preceding position. Inclusion of serine at a similar position in DUG vOTU, which lacks a threonine directly preceding it, highlights that, although affinity appears to be synergistic, single unfavorable amino acid changes within nairovirus vOTUs can have deleterious effects. An additional example of CCHF vOTU residue Glu128, which is a glycine in a CCHFV strain, UG3010, exemplifies this point by suggesting that even vOTUs that harbor polymorphisms between strains can have considerably divergent enzymatic behavior (Figure 3.9).

Understandably, with only monomeric Ub bound to DUG vOTU-Ub and CCHF vOTU-Ub, these structures have limitations in directly revealing any specifics on what may drive nairovirus vOTUs to cleave only K6, K11, K48, and K63 poly-Ub linkages or accounting for these vOTUs' greater rates of cleavage of certain linkages over those observed for Ub-AMC, such as those observed for CCHF vOTU's and DUG vOTU's cleavage of K63 and K48 poly-Ub linkages, respectively. Although the precise origins surrounding poly-Ub specificity may require additional structural studies, the tertiary structural similarities between the vOTUs of DUGV and CCHFV suggests that these differences between nairovirus vOTUs are likely primarily structural in nature.

Nairovirus vOTUs and other vOTUs

The increasing inclusion of new vOTU members originating across the viral genomes other than nairoviruses, including those of arteriviruses, tymoviruses, and tenuiviruses, has spurred speculation on whether there is possible conservation of functionality among these proteases[39, 46, 99]. Supporting this assertion has been the sequence similarity beyond the first 20 to 30 equivalent amino acids of nairoviruses and

vOTUs originating from these other viruses (Figure 3.1). However, there are substantial differences between the four groups of viruses currently known to utilize vOTUs, including the necessity for vOTUs to cleave viral polypeptides in ssRNA (-) vOTU-containing viruses, the location of viral replication complexes within the host cells, and whether the host is plant or animal. Intriguingly from a protease prospective, the vOTU from the ssRNA (+) tymovirus TYMV has a very low deubiquitinating activity—almost 3 orders of magnitude less than vOTUs from DUGV and CCHFV for Ub and poly-Ubs—suggesting that deubiquitinating activity might be secondary to polypeptide cleavage. However, TYM vOTU does prefer the same four, K6, K11, K48, and K63 poly-Ub linkages to the others, as do nairovirus vOTUs. Unfortunately, vOTUs from arteriviruses, such as PRRSV, have not been evaluated against all eight poly-Ub types of linkages, nor have their respective rates toward Ub and ISG15 been established, but they have been observed to cleave both K63 and K48 poly-Ub linkages[99]. This, with previously established sequence homology, could suggest arteriviruses may also have activity toward K6 and K11 poly-Ubs.

Potential influence of nairovirus vOTUs specificity on pathogenesis

A wide array of disease outcomes has been observed for nairovirus infections of humans and animals ranging from transient viremia and migraines to mortality[46, 93, 100]. Previous studies have proposed that vOTUs play a significant role in the ability of nairoviruses to evade host immune response through their deubiquitinating and deISGylating activities, prompting them to be considered potential virulence factors[39, 84, 85, 93, 96]. This classification suggests that a significant divergence in vOTU activity, or

specificity, possibly exists between vOTUs from different nairoviruses and potentially within species. The evaluation of deubiquitinating and deISGylating activities of vOTUs from CCHFV, DUGV, and ERVEV appears to support this assertion. Despite a reasonably high sequence similarity between three evaluated nairovirus vOTUs, orders of magnitude differences in proteolytic activity between them have been observed for different Ub moieties, as well for hISG15 conjugates. Distilling these preferences into catalytic efficiencies readily reflects that particular nairovirus vOTUs do not always possess robust dual human deubiquitinating and deISGylating functionality with a preference for ubiquitinated substrates as the previously studied vOTU from CCHFV may have proposed (Table 3.2)[84, 85, 96]. Instead, the preference of nairovirus vOTUs potentially could be either for ubiquitinated substrates, ISGylated ones, or both.

Curiously, among the nairovirus vOTUs evaluated, only the one from the often-human fatal CCHFV has coexisting robust deubiquitinating and deISGylating activities related to Ub and hISG15. The vOTUs from DUGV and ERVEV, which have currently not been observed to be fatal in humans, only possess substantial activity toward one or the other. For ERVE vOTU, the virtually complete amino acid conservation among Ub within animals suggests that ERVE vOTU predominantly acts as a deISGylase during infection, making it the first known viral protease that is incapable of effectively cleaving both monomeric and polymeric Ub conjugates while still retaining strong activity for hISG15.

This unique ability of CCHF vOTU to cleave hISG15 conjugates at relatively high rates originally had differentiated CCHF vOTUs from other members of the OTU

superfamily and likened CCHF vOTU to a virulence factor of severe acute respiratory coronavirus, papain-like protease (PLpro), which also has strong deubiquitinating and deISGylating activities[39, 85, 101]. However, the PLpro and CCHF vOTU similarities go beyond their ability to cleave both Ub and hISG15. CCHF vOTU appears to be unique among the three evaluated nairovirus vOTUs for its ability to robustly cleave K63 poly-Ub linkages, while retaining the comparable ability to cleave K48 poly-Ub, such as is the case for PLpro[102]. This is in contrast to other known viral deubiquitinases, such as herpes virus M48, or vOTUs from other nairoviruses, including DUG vOTU[74]. Also, the robust specificity for K63 poly-Ub that CCHF vOTU possesses may be of importance pathogenically since Bogunovic et al. recently suggested that ISGylation and ubiquitination might be redundant in humans for viral infections[103]. With certain host immunologically related proteins having been observed to be modified with either ISG15 or K63 poly-Ub, the removal of both by a viral protease may ensure immunosuppression. Comparison of CCHF vOTU's poly-Ub preferences and those of other vOTUs also illustrates that CCHF vOTU is also the most specific to the four poly-Ub linkages—K6, K11, K48, and K63—that the currently evaluated vOTUs prevailingly cleave (Figure 3.3). This also likely downplays the need for nairoviruses to cleave these other forms of poly-Ub moieties for successful viral evasion. Overall, the substrate preferences of the nairovirus vOTUs evaluated here suggest that a virus containing a vOTU capable of not only deubiquitinase and species-specific deISGylase activities but also robust deubiquitinase activity toward K63 poly-Ub linkages might have the best chance for viral immune evasion and pathogenesis. Naturally, the full impact of diversity in specificity

among vOTUs on viral pathogenesis can ideally be addressed when a reverse genetics system for nairoviruses is available.

Chapter 3 is in part a reprint of the material as it appears in Capodagli G. C., Deaton M. K., Baker E. A., Lumpkin R. J., and Pegan S. D. (2013) *Diversity of Ubiquitin and ISG15 Specificity among Nairoviruses' Viral Ovarian Tumor Domain Proteases.* J Virol., **87(7)**: 3815-27. The dissertation author was primary researcher and author of this publication.

Chapter Four: Summary

In the previous two chapters I have detailed our findings on the substrate specificity of the vOTU protease from several nairoviruses, as well as one tenuivirus. Here I will summarize our results and place them into the context of this new class of DUB proteases. When the vOTU from CCHF was first studied for its substrate activity, it demonstrated the ability to robustly cleave both Ub and ISG15[(39)]. As this was the first time this class of enzyme was examined, it lead to speculation as to whether all vOTUs possessed such DUB and deISGylating capacity. Our findings clearly show that this is not the case, and that even vOTUs from the same family possess unique substrate specificities. Although the DUG vOTU and ERVE vOTU maintain a high level of sequence homology to CCHF vOTU, DUG vOTU only readily cleaves Ub and ERVE vOTU only ISG15. While it is not surprising that a vOTU that would not encounter ISG15 would show practically no affinity for the substrate, such as in the case of TYMV, it is interesting that there was also limited DUB activity as the sequence homology across species of Ub is nearly identical. The ability to discriminate between substrates is even further differentiated when one compares each of the vOTUs' ability to cleave different poly-Ub moieties. Our gel shift assays demonstrate how both linkage position (lysine 48 vs lysine 63) and linkage length (dimeric vs tetrameric) are important in determining which target proteins may be affected by each vOTU's activity. Furthermore, vOTUs appear to be able to distinguish ISG15 from different species as in the case of ERVE

vOTU, which showed a shift in activity when mISG15 was introduced into the assay containing hISG15[104]. The reason for the difference in ISG15 recognition likely stems from the higher degree of sequence disparity between species, and that a vector for the ERVEV has been reported to be the white tooth shrew, whose ISG15 may share more sequence homology to mISG15 than hISG15.

To better understand the reasoning behind the varied activities of the vOTU family, two crystal structures were obtained in complex with Ub: one with CCHF vOTU and one with DUG vOTU. Although the overall folds of the proteases in these complexes share some similarities with other OTU family members, there are several points of departure that help explain the variances in substrate specificity. The addition of the β1 and β1a sheets in the vOTU structures forces a modification in how their substrates bind when compared to yOTU and OTUB1/2. Similarly, the altered binding orientation creates several different binding interactions with respect to vOTU's α3-helix and active site. Predictably, the secondary structures of both vOTUs were nearly identical when compared to each other except for their α3-helix. Recently, the structure of CCHF vOTU covalently bound to ISG15 has been solved and was shown to strongly agree with our model thus revealing which residues are also involved in ISG15 recognition (Figure 2.7)[96]. The similarity in the two vOTUs' secondary structure implicates the primary structure of each protein as the likely source for the differing proteolytic activity. Our site-directed mutagenesis studies validate this assertion as swapping out key residues involved at the Ub/ISG15 interface have been discovered to both shift the substrate preferences of the vOTUs as well as decrease overall activity. As no single mutation to

DUG vOTU brings the activity for either Ub or ISG15 to the same levels as CCHF vOTU, it is likely that there exists a synergistic effect on the part of all the residues involved in the interface between the vOTUs and their preferred substrate.

vOTUs have been suggested to be a virulence factor that help their virus evade the immune system of the host, although the exact mechanism is not fully understood. The data presented here offer credence to this theory and lend some insight as to the possible aspects involved. CCHFV has a high mortality rate in humans, yet almost none in any other mammals. Not only can its vOTU cleave hISG15 and K63-linked poly-Ub readily, it does so preferentially over mISG15 and other Ub linkages. Interestingly, the UG3010 strain of CCHFV, which has been shown to have lower mortality rates, also has a mutation we have shown reduces both ISG15 and Ub cleavage[(97)]. Likewise, DUGV only causes minor viremia in all of its hosts, and although its vOTU possesses decent mono-Ub activity, it has limited K63-poly-Ub and ISG15 activity compared to the vOTU from CCHFV. On the other hand, the ERVEV has been suggested to cause thunderclap headaches in humans without being life threatening. Although ERVE vOTU has the highest ISG15 affinity of vOTUs tested to date, it also shows less specificity than the vOTU from CCHFV, and also lacks any appreciable Ub activity. Together these data suggest that perhaps the ability to efficiently cleave both ISG15 and K63-linked poly-Ub are essential for a virus's ability to evade the host's innate immune system.

SECTION II

Chapter Five: A Noncompetitive Inhibitor for Mycobacterium tuberculosis's Class IIa Fructose 1,6-Bisphosphate Aldolase

Abstract

Class II fructose 1,6-bisphosphate aldolase (FBA) is an enzyme critical for bacterial, fungal, and protozoan glycolysis/gluconeogenesis. Importantly, humans lack this type of aldolase, having instead a class I FBA that is structurally and mechanistically distinct from class II FBAs. As such, class II FBA is considered a putative pharmacological target for the development of novel antibiotics against pathogenic bacteria such as *Mycobacterium tuberculosis*, the causative agent for tuberculosis (TB). To date, several competitive class II FBA substrate mimic-styled inhibitors have been developed; however, they lack either specificity, potency, or properties that limit their potential as possible therapeutics. Recently, through the use of enzymatic and structure-based assisted screening, we identified 8-hydroxyquinoline carboxylic acid (HCA) that has an IC_{50} of 10 ± 1 μM for the class II FBA present in *M. tuberculosis* (MtFBA). As opposed to previous inhibitors, HCA behaves in a noncompetitive manner, shows no inhibitory properties toward human and rabbit class I FBAs, and possesses anti-TB properties. Furthermore, we were able to determine the crystal structure of HCA bound to MtFBA to 2.1 Å. HCA also demonstrates inhibitory effects for other class II FBAs, including pathogenic bacteria such as methicillin-resistant *Staphylococcus aureus*. With its broad-spectrum potential, unique inhibitory characteristics, and flexibility of

functionalization, the HCA scaffold likely represents an important advancement in the development of class II FBA inhibitors that can serve as viable preclinical candidates.

Introduction

Tuberculosis (TB) is one of the most prevalent infections in the world and a leading cause of mortality in developing countries[(105)]. *Mycobacterium tuberculosis*, the causative agent for TB, infections have been estimated by the World Health Organization (WHO) at 8.7 million new cases during 2011, with 1.4 million *M. tuberculosis*-related deaths[(106)]. This brings the total number of estimated new cases and deaths over the past five years to a staggering 45.6 million and 8.1 million, respectively. Additionally, one-third of the world's population is estimated to have latent *M. tuberculosis*[(105)]. Further exacerbating the danger of TB is the considerable rise of TB co-infecting patients with HIV. Specifically, individuals infected with HIV are more than 20 times more likely to develop active TB and thus be able to rapidly spread the disease[(106, 107)]. The current treatment for TB, Directly Observed Therapy, Short Course (DOTS), relies on directly observing the administration of a four-drug cocktail over a two-month span with continuous two-drug treatments for an additional two−four months[(108)].

In recent years, the WHO has estimated that the rate of curing TB with DOTS has declined from 95 to 85%[(106)]. A significant factor in this decline, which has thwarted intensifying efforts to eliminate TB, is increasing drug resistance. Incidences of multidrug-resistant TB (MDR-TB), TB resistant to the two most efficacious TB drugs, are on the rise, with 500,000 cases reported in 2011[(106)]. Also, spreading of extensively drug-resistant TB (XDR-TB), MDR-TB with additional resistance to almost all known

TB drugs, has occurred. As of 2011, XDR-TB has appeared in 84 countries, including the United States[106]. For MDR-TB, new treatment regimens, including DOTS plus, have been initiated but require 18 months of treatment[109]. Treatment options for XDR-TB are even more limited[109]. Also, the practicality of these prolonged pharmacological treatments is largely in doubt, as patient compliance difficulties have already been encountered during the six-month DOTS treatment[109].

The absence of an effective treatment for MDR-TB and XDR-TB and the increase in the number of active TB cases among HIV patients highlight the need to explore other potential TB drug targets. One widely touted potential drug target is *M. tuberculosis's* sole fructose 1,6-bisphosphate aldolase (MtFBA, EC 4.1.2.13)[110-121]. As a class II fructose 1,6-bisphosphate aldolase, MtFBA falls into one of two classes of fructose 1,6-bisphosphate aldolases (FBAs). Both class I and class II FBAs catalyze the reversible aldol condensation of dihydroxyacetone phosphate (DHAP) with glyceraldehyde 3-phosphate (G3P) to form fructose 1,6-bisphosphate (FBP)[122]. However, the two enzyme classes differ in their mechanism of catalysis and prevalence among species, which has made class II FBAs a highly sought after bacterial target for pharmacological development. Specifically, class I FBAs utilize a lysine residue to generate a nucleophilic enamine from DHAP, whereas class II aldolases utilize a Zn (II) cation to stabilize the DHAP enolate intermediate involved in the aldol condensation reaction[119]. Also, the location of a key amino acid side chain responsible for proton extraction and addition significantly differs[119, 123, 124]. Beyond the differences in their reaction mechanisms, the two classes of FBAs distinctly differ in their distribution among species. Higher

organisms such as humans possess only class I FBAs, whereas protozoa, bacteria, fungi, and blue-green algae primarily have class II FBAs, with a few possessing both[125-127]. In other words, selective inhibitors developed for class II FBAs are unlikely to generate toxic effects through disruption of the human class I FBA.

Additionally, the essentiality of class II FBAs within bacteria has been illustrated via knockout studies of both Gram-positive and Gram-negative bacteria, including *M. tuberculosis, Escherichia coli, Streptomyces galbus, Bacillus subtilis, Pseudomonas aeruginosa, Streptococcus pneumoniae,* and *Candida albicans*[115, 119, 128-136]. Although bacteria such as *E. coli* and other autotrophic prokaryotes possess both class I and class II FBAs, class I FBAs are only conditionally expressed, with class II FBAs being essential[115, 120, 137, 138]. Beyond knockout studies and MtFBA being the only FBA in *M. tuberculosis*, MtFBA has been observed to be more abundantly produced and/or secreted by *M. tuberculosis* when placed in hypoxic conditions similar to those found within necrotic pulmonary lesions where *M. tuberculosis* resides[111, 121]. A p-blast search also illustrates that MtFBA is 100% conserved across all sequenced strains of *M. tuberculosis*, including XDR-TB strain KZN605 as well as MDR-TB strain KZN1435. Taken together, the essentiality of class II FBAs and the absence of a human homolog have placed class II FBAs among the top potential bacterial drug targets currently lacking a viable preclinical drug candidate.

Naturally, as the essentiality of class II FBAs in bacteria was revealed in 2003, efforts began in earnest to develop class II FBA inhibitors for use as treatments related to TB and other bacterial and protozoan infections[115]. The first generation of these

inhibitors began with the candidacy of a DHAP analogue, phosphoglycolohydroxymate (PGH) that was first reported in 1974[113]. Although PGH inhibits class II FBAs through competitive inhibition by mimicking DHAP, PGH is extremely promiscuous, inhibiting several mammalian enzymes, including class I FBAs[112, 139, 140]. Recent attempts to follow up on the competitive substrate mimicry approach utilized the chemical skeleton of FBP and focused on zinc−inhibitor interactions to gain greater specificity. Although low-micromolar, selective competitive inhibitors were observed for MtFBA and other bacterial class II FBAs, all of the inhibitors relied on the presence of one or two phosphate groups for selectivity and affinity[110, 112, 113, 116, 117, 125, 141]. Not surprisingly, with the presence of the highly charged phosphate moiety that likely interferes with transport across the cell membrane, only one of these substrate mimic-styled inhibitors has a measurable minimal inhibitory concentration (MIC) despite them being assessed up to 1 mM[110, 112, 113, 116, 117, 125, 141]. This sole exception is FBP analogue TD3 that possesses a 40 nM affinity for MtFBA. However, despite a recent attempt to validate or optimize TD3, no inhibitory effect on *M. tuberculosis* growth was observed, illustrating the limits of these types of inhibitors [110, 112].

Recently, we identified a chemical scaffold, 8-hydroxyquinoline- 2-carboxylic acid (HCA), through the use of enzymatic and structure-based assisted screening that allows for selective, druglike, low-micromolar, noncompetitive inhibition of *M. tuberculosis* class IIa FBA as well as those from other pathogenic bacteria. To elucidate the *in vitro* characteristics of the interaction between HCA and MtFBA, the ability of HCA to inhibit MtFBA at multiple concentrations was examined, and isothermal titration

calorimetry (ITC) was performed. Finally, an X-ray crystal structure of HCA bound with MtFBA was elucidated to 2.1 Å and compared to the apo and substrate-bound forms of MtFBA.

Methods

This research was supported in part by grants from the Professional Research Opportunities for Faculty, the Colorado Center for Drug Discovery, Cancer Center Support Grant P30CA046934, and the Regis University Research and Scholarship Council. The Advanced Light Source is supported by the Director, Office of Science, Office of Basic Energy Sciences, of the U.S. Department of Energy under Contract DE-AC02-05CH11231.

I thank Mrs. Victoria Jones for her help with determination of MICs as well as Dr. Alexander Mankin (University of Illinois, Chicago, IL) for generously providing expression vector pCA24n-*fba*A harboring the *fba*A gene from *E. coli* K-12. Also, Dr. Den R. Tolan (Boston University, Boston, MA) for generously donating the Sigma-Aldrich rabbit class I FBA.

Production and Purification of FBAs

The construction of the *M. tuberculosis* pET17b-*fba*H expression vector harboring the *fba* gene (Rv0363c) was performed as previously described[(119)]. The pET-*fba*H plasmid was introduced into *E. coli* BL21 (DE3) by heat-shock transformation for enzyme expression. The resulting plasmid was then purified, restriction analyzed, and sequenced to verify the construct. The expression system produced a C-terminal, His-tagged fusion protein, which is herein termed MtFBA. Cells containing MtFBA were

grown in 12 L of Luria Broth (LB) broth containing 100 μg/mL ampicillin until an OD at 600nm of 0.6 was reached. Expression of the *fba*H gene was induced by addition of IPTG (isopropyl-β-D-thiogalactopyranoside) to a final concentration of 0.4 mM, and the culture was grown for an additional 4−6 h at 25 °C. Following this period, the bacterial cells were isolated via centrifugation at 3000*g* for 10 min and stored at −80 °C. The cell pellets were suspended in buffer A (300 mM NaCl and 50 mM Tris [pH 8.0]) and lysed by addition of 5 mg of chicken lysozyme followed by sonication. The insoluble cell debris was separated via centrifugation for 45 min at 17000*g*. MtFBA was purified from the resulting supernatant by using a Qiagen Ni-NTA column and eluted with buffer A containing 300 mM imidazole followed by buffer exchange into buffer B (100 mM NaCl, 20 mM Tricine [pH 8.0], 2 mM dithiothreitol [DTT], and 0.1 mM $ZnCl_2$) by passage over a Superdex-S200 High Resolution column. The purified MtFBA was concentrated to 16 mg/mL via 10000 molecular weight cutoff centrifugal filter units (Millipore Cork, IRL) at 4000*g*. The final protein was then filtered through 0.22 μm Costar spin filters.

The production of the FBA expression vector for a methicillin resistant strain of *Staphylococcus aureus* (SaFBA) was generated using *E. coli* BL21 optimized synthesis by Genscript, Inc. The SaFBA expression construct encodes the 289 amino acids from UniProtKB entry Q5HE75.1 as well as six histidines and a stop codon to generate a C-terminal histidine tag and incorporated them into pET11a plasmids using NdeI and BamHI restriction sites. Transformation, expression, and purification were performed in a manner similar to that of MtFBA.

The *E. coli* K-12 class II FBA was obtained from the ASKA library in a pCA24n-*fba*A expression vector harboring the *fba*A gene[142]. Transformation, expression, and purification were performed in a manner similar to that of MtFBA with the exception that 25 μg/mL chloramphenicol was used in place of ampicillin.

FBA purified from rabbit muscle was obtained as an ammonium sulfate suspension from Sigma-Aldrich (catalog no. A8811). The suspension was spun down at 13000*g* for 10 min at 4 °C, the supernatant discarded, and the pellet resuspended in buffer B supplemented with 1 mM EDTA. The resuspended protein was centrifuged again at 3000*g* for 15 min to remove any solids that remained.

Recombinant human aldolase-A was purchased form Gen-Way Biotech, Inc., at a concentration of 1 μg/μL in buffer C (20 mM Tris-HCl [pH 8.0], 100 mM NaCl, and 20% glycerol).

All protein concentrations were determined through UV−visible spectroscopy at 280 nm using molar extinction coefficients experimentally derived by the method of Gill and von Hippel[61].

FBA Enzymatic FBP Cleavage Assays

The activity of FBAs was monitored through a fluorescence-based assay measuring the increase in fluorescence due to conversion of resazurin to resorufin via diaphorase when coupled with the oxidation of NADH to NAD^+. The assay mixture (final volume of 50 μL) contained 0.4 mM NAD^+, 8 units/mL rabbit glycerol-3-phosphate dehydrogenase (GAPDH), 0.01% (w/v) bovine serum albumin (BSA), 2 mM DTT, 15 mM NaH_2AsO_4, 100 mM Tris HCl (pH 7.8), 100 mM CH_3COOK, 180 nM MtTPI, 1

unit/μL diaphorase, and 50 μM resazurin. Triton X-100 was included at a final concentration of 0.01% in follow-up assays to identify any promiscuous inhibitors. For FBAs derived from *M. tuberculosis* and *E. coli*, a final assay concentration of 4 nM was used. For FBAs derived from *S. aureus*, rabbit, and human, a final assay concentration of 40 nM was used. The reaction was initiated via the addition of FBP at an assay concentration of 75 μM. All assays were performed at room temperature and in duplicate using Costar 96-well half-area, black flat-bottom polystyrene plates (Corning). All FBA activity assays were conducted using a TECAN M1000 plate reader by measuring the fluorescence of resorufin at 585 nm when it was excited at 535 nm. A standard curve for FBP conversion was determined by adding excess MtFBA to various concentrations of FBP and allowing the reactions to run to completion. The resulting maximal fluorescence values were plotted to determine the slope and subsequently the conversion factor.

The IC_{50} value for the inhibition of MtFBA by HCA was determined at HCA concentrations ranging from 0 to 100 μM, with the FBP concentration held constant at 75 μM. The percent inhibition (I%) was calculated using the formula $I\% = [1 - (\nu_{sample} - \nu_{negative\ control})/(\nu_{positive\ control} - \nu_{negative\ control})] \times 100$. The resulting I% values were fit via nonlinear regression to the equation $I\% = I\%_{max}/(1 + IC_{50} / [HCA])$ using the Enzyme Kinetics Module of SigmaPlot, version 12.2 (SPSS, Inc.).

To determine the mode of action of HCA, inhibition studies were conducted using HCA concentrations ranging from 0 to 25 μM with four additional concentrations of FBP ranging from 9 to 150 μM used to initiate the reaction. Initial velocity data were fit using nonlinear regression analysis to each of the equations describing partial and full models

of competitive, uncompetitive, noncompetitive, and mixed inhibition using the Enzyme Kinetics Module of SigmaPlot. On the basis of the analysis of fits through "goodness-of-fit" statistics, the full noncompetitive inhibition model was determined with the equation $v = V_{max}/[(1 + [I]/K_i) \times (1 + K_M/[S])]$, where [S] = [FBP], [I] = [HCA], and K_i is the constant for dissociation of HCA from free MtFBA.

The class II FBAs from *E. coli* (4 nM) and *S. aureus* (40 nM) as well as the class I FBAs from rabbit muscle (40 nM) and human muscle (40 nM) were tested with a final HCA concentration of 25 μM. The reaction was initiated with 75 μM FBP, and I% was calculated as previously described.

Isothermal Titration Calorimetry (ITC) Experiments

The ITC experiments were performed in duplicate using a NanoITC system (TA Instruments, Lindon, UT). MtFBA was dialyzed overnight at 4 °C against buffer D (100 mM NaCl, 20 mM Tricine [pH 8.0], and 2% Dimethyl sulfoxide [DMSO]). HCA and $ZnCl_2$ were dissolved using the buffer in which MtFBA was dialyzed to concentrations of 5 and 10 mM, respectively. To assess the interaction between HCA and free zinc (II) ion, a solution of 5 mM HCA was titrated into 0.4 mM $ZnCl_2$. To assess the interaction between HCA and MtFBA, equal portions of 5 mM HCA and 10 mM $ZnCl_2$ were mixed and the HCA/$ZnCl_2$ mixture was titrated into 0.25 mM MtFBA. ITC runs were performed at 25 °C and comprised of one injection of 1 μL followed by 24 injections of 2 μL for a total of 25 injections. Each injection was spaced 200 s apart. The average heat released for the last five injections was used to correct for the heat of dilution. Data sets were analyzed with NanoAnalyze and fit to an independent model.

Inhibitor Susceptibility Testing

MIC values in 7H9-ADC-Tween 80 broth at 37 °C against *M. tuberculosis* H37Rv (avirulent strain $mc^2$6206) were determined using the resazurin blue assay and by visually scanning for growth[(143)].

Crystallization of the MtFBA-HCA Complex

Initial crystallization conditions for the substrate-less, zinc-bound holo-MtFBA were achieved using conditions from our previously described protocols[(119)]. The final crystal was grown using hanging-drop vapor diffusion at 20 °C. Crystallization drops included 2 μL of a 16 mg/mL MtFBA protein solution containing buffer B mixed in a 1:1 ratio with 26% Polyethylene Glycol (PEG) 300, 0.1 M sodium acetate (pH 4.5), and 2% DMSO. After 4 weeks, the holo crystal was removed from the hanging drop, placed in 5 μL of a soaking solution containing 2.5 mM HCA, 26% PEG 300, 0.1 M sodium acetate (pH 4.5), and 2% DMSO for 1 h, and then flash-cooled in liquid nitrogen.

X-ray Structure of the the MtFBA−HCA Complex

An X-ray data set was collected using a crystal mounted onto a nylon loop flash-cooled in liquid nitrogen. The crystal was mounted under a stream of dry N_2 at 100 K. An MtFBA−HCA complex data set with resolution to 2.10 Å was collected at Advance Light Source (ALS) beamline 4.2.2 using a monochromic X-ray beam of 1.00 Å with a NOIR-1 MBC detector. X-ray images were indexed, processed, integrated, and scaled using HKL2000[(62)]. An initial phase solution was elucidated using holo-MtFBA [Protein Data Bank (PDB) entry 4DEF] as a starting model for molecular replacement using Phaser[(5)]. The structure was refined using iterative cycles of model building and refinement using

COOT and phenix.refine, respectively[66, 67]. Water molecules were added to $2F_o - F_c$ density peaks of $>1\sigma$ using the Find Water COOT program function. The final model was checked for structural quality using the CCP4 suite programs Procheck and Sfcheck. The data refinement statistics are listed in Table 5.1.

Modeling Missing Loops into the Structure of the MtFBA−HCA Complex

Residues 167−177 and 210−223, which were unresolved in the X-ray crystal structure of MtFBA bound to HCA, were modeled in using MODELER 9v11 under default settings and the known sequence of MtFBA[144]. Five models were generated and inspected in PyMOL, and the final model was chosen by molpdf score.

	MtFBA-HCA
Data Collection	
Space Group	I 2 2 2
Unit Cell Dimensions	
a, b, c (Å)	60.6, 118.9, 165.2
$\alpha = \beta = \gamma$ (°)	90
Resolution (Å)	50.0 – 2.10
No. Reflections Observed	145,672
No. Unique Reflections	36,003
R_{merge} (%)[a]	9.9 (28.5)*
I/σI	16.4 (3.5)*
% Completeness	98.6 (87.0)*
Refinement	
Resolution Range	50 – 2.10
No. Reflections in Working Set	35,983
No. Reflections in Test Set	1,799
R_{work} (%)[b]	16.2 (17.3)*
R_{free} (%)[b]	19.1 (20.3)*
RMS deviation:	
Bond Lengths (Å)	0.01
Bond Angles (°)	1.0
Protein / Water / Ligands Atoms	2464 / 357 / 40
Average B-Factors (Å^2)	
Total	30.8
Protein	28.9
Water	41.2
Ions	33.8
Ligands	44.6
HCA	43.4

* The last resolution shell is shown in parentheses. [a] $R_{merge}=\Sigma_h\Sigma_I |I_I(h) - \langle I(h)\rangle| / \Sigma_h\Sigma_i I_I(h)$, where $I_I(h)$ is the i^{th} measurement and $\langle I(h)\rangle$ is the weighted mean of all measurements of $I(h)$. [b] R_{work} and $R_{free} = h(|F(h)_{obs}| - |F(h)_{calc}|) / h|F(h)_{obs}|$ for reflections in the working and test sets, respectively. R.m.s., root mean square.

Table 5.1. Data Collection and Refinement Statistics for the MtFBA−HCA Complex

Results

Identification of HCA as an Inhibitor of MtFBA

Seeking an alternative to the substrate mimic-styled inhibitors that lack several qualities thus limiting their potential as viable preclinical leads for MtFBA and other class II FBAs, we adopted a fragment-based strategy. This strategy focused on enzymatically screening chemical moieties that would simulate the enolate transition state's hydroxamic acid of PGH with MtFBA's active site Zn (II) but be devoid of groups that would interfere with pharmaceutical development. This set of compounds included several heterocyclic zinc binding groups that were used to screen for matrix metalloprotease inhibitors[(145-150)].

Utilizing an assay that coupled MtFBA activity with *M. tuberculosis's* triosephosphate isomerase (TPI), rabbit glycerol-3-phosphate dehydrogenase (GAPDH), and diaphorase for a fluorescent output, 60 small molecules were screened in duplicate at a concentration of 1 mM. In addition to using a fluorophore that excited and emitted at wavelengths of >500 nm to prevent false positives, the assay also included DTT as well as BSA to ward off promiscuous inhibition[(151, 152)]. This small, low-throughput screening campaign revealed that 8-hydroxyquinoline-2-carboxylic acid (HCA) reduced MtFBA activity more than 95% at a concentration of 1 mM.

Although several measures were taken to ward off promiscuous inhibition within the screening assay and reduce false positives, additional validation steps were conducted to further support HCA as an MtFBA inhibitor. Addition of Triton X-100, a known disruptor of aggregation-based inhibition, was introduced to test for any promiscuous

inhibition, with no alteration in potency observed (Figure 5.1a)[151]. Despite the coupling enzymes already being in >40-fold excess, to further rule out the possibility that HCA was inhibiting a coupling enzyme instead of MtFBA, a 160-fold excess of each coupling enzyme was added and assessed at a HCA concentration of 25 μM (Figure 5.1a). No ablation of HCA inhibition was observed; suggesting HCA's effect on the assay was linked specifically to MtFBA inhibition. Also, as expected, no HCA-facilitated inhibition of the assay was detected when MtFBA's assay products DHAP and G3P were substituted for MtFBA. Understandably, there have been numerous reports of compounds possessing 8-hydroxyquinoline moieties acting as promiscuous chelating agents[147, 153, 154]. To test this possibility, a 2-fold increase in the level of Zn (II) was used to determine if HCA was indirectly inhibiting MtFBA activity by sequestering Zn (II) in solution. If HCA was limiting MtFBA's access to Zn (II), or stripping MtFBA of Zn (II), an increase in the level of Zn (II) should reduce the inhibitory effects of HCA on MtFBA activity. Unexpectedly, the potency of HCA for MtFBA slightly increased (Figure 5.1a). A

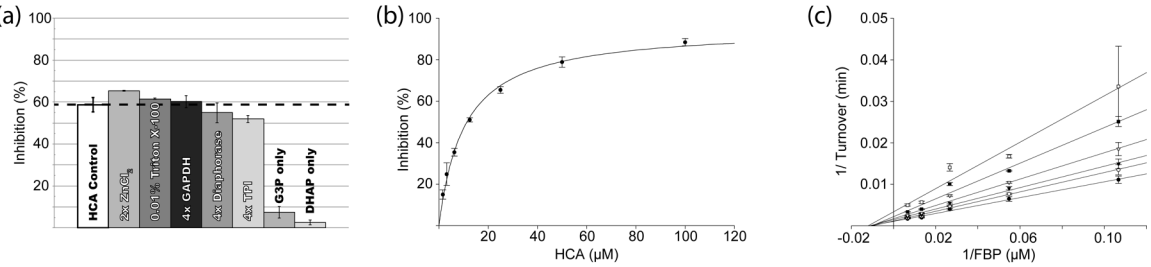

Figure 5.1. Kinetic studies of HCA's inhibition of MtFBA. (a) HCA (25 μM) was tested for its ability to inhibit MtFBA activity in the presence of 50 μM $ZnCl_2$, 0.01% Triton X-100, and a 160-fold excess of coupling enzymes GAPDH, diaphorase, and MtTPI or FBP products G3P and DHAP (75 μM). The dashed line is drawn from the control of 25 μM HCA to aid in comparison. Error bars represent the standard deviation from the average. (b) Plot of HCA concentration in the presence of a 2-fold excess of $ZnCl_2$ as the HCA concentration was varied from 0 to 100 μM using the Michaelis−Menten equation to determine the IC_{50}. (c) Lineweaver−Burke plot of inhibition of MtFBA by HCA. Concentrations of HCA in the presence of a 2-fold excess of $ZnCl_2$ were (●) 0, (○) 1.625, (▼) 3.125, (▽) 6.25, (■) 12.5, and (□) 25 μM. Data were globally fit to a pure noncompetitive inhibition model.

dose−response relationship of HCA and MtFBA conducted under these conditions yielded an IC_{50} of 10 ± 1 μM (Figure 5.1b). Importantly, HCA inhibited the growth of *M. tuberculosis* in 7H9-OADC broth at a concentration of 0.6−1.2 mM.

Biochemical and Biophysical Properties of the MtFBA−HCA Interaction

To characterize the nature of the inhibition of MtFBA by HCA, kinetic studies and ITC experiments were conducted. To understand the mechanism of inhibition of MtFBA activity by HCA, five different FBP concentrations and six different HCA concentrations were utilized to determine the kinetic response of MtFBA to varying concentrations of substrate and inhibitor. Surprisingly, only the V_{max} of MtFBA was significantly affected over a 20-fold increase in inhibitor concentration, whereas the K_M remained constant (Figure 5.1c). This along with using nonlinear regression analysis indicated that HCA acts in a noncompetitive manner against FBP with a K_i of 12 ± 1 μM, instead of a competitive manner like previously characterized class II FBA inhibitors. Next, as HCA is known to bind to zinc (II), the biophysical binding characteristics of HCA and free zinc (II) in solution were analyzed via ITC. This revealed an exothermic binding event with the following values: K_d = 9.39 ± 0.79 μM, ΔH = −26.8 ± 0.3 kJ/mol, ΔS = 6.9 ± 0.9 J mol^{-1} K^{-1}, and n = 1.86 ± 0.10 (Figure 5.2a). The binding stoichiometry of HCA and free zinc (II) in solution determined by ITC matches current X-ray crystallography data for the structure of HCA bound to free zinc (II), which also showed HCA and zinc (II) interacting in a ratio of 2:1[(153)]. Intriguingly, the data from the enzymatic assay showed that HCA's inhibitory effects against MtFBA are not reduced in the presence of a 2-fold excess of $ZnCl_2$. Therefore, to assess the thermodynamic factors

that may favor HCA's interaction with MtFBA versus free zinc (II), HCA was first combined with a 3-fold excess of $ZnCl_2$ required for the formation of the HCA−free zinc (II) complex and then titrated into MtFBA. As Pegan et al. and de la Paz Santangelo et al. recently reported that zinc (II) has to be in solution for the active site of MtFBA to be fully occupied, the presence of excess zinc (II) ensured full occupancy[111, 118]. In addition, the excess zinc allows for the observation of thermodynamic contributions outside of HCA−zinc (II) binding events whether with free zinc (II) in solution or the active site zinc of MtFBA. Interestingly, the binding profile of HCA with excess $ZnCl_2$ in MtFBA differed from that of HCA and free zinc (II), resulting in the following values: $K_d = 70.8 \pm 2.7$ μM, $\Delta H = -66.0 \pm 1.0$ kJ/mol, $\Delta S = -141.9 \pm 3.2$ J mol^{-1} K^{-1}, and $n = 0.96 \pm 0.01$ (Figure 5.2b). This suggests that additional enthalpic forces are present within the interaction between HCA and MtFBA and may be responsible for HCA's ability to inhibit MtFBA in a direct manner.

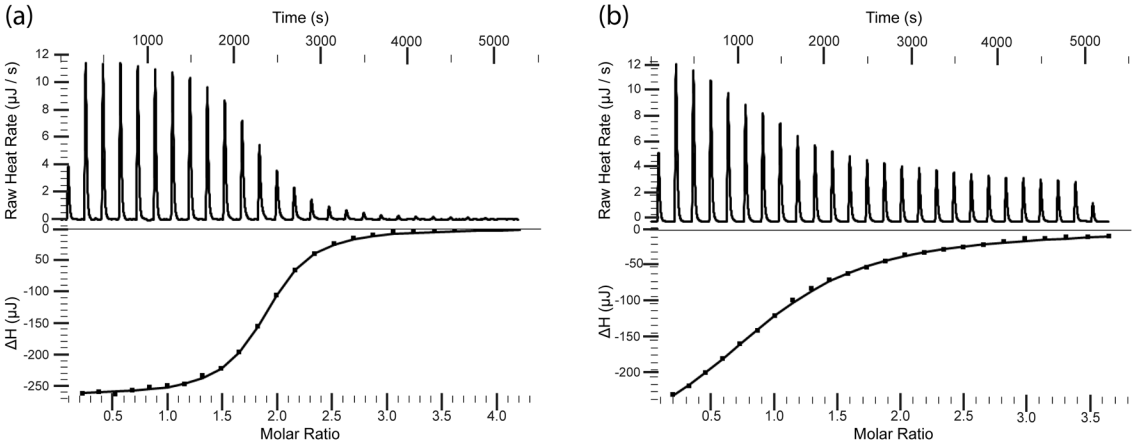

Figure 5.2. ITC binding of MtFBA with HCA. The top panel represents the raw heat data from 25 injections at 25 °C, and the bottom panel shows the integrated heat peak areas plotted vs the molar ratio of (a) HCA to $ZnCl_2$ or (b) HCA in the presence of excess $ZnCl_2$ to MtFBA. The last five data points were averaged for the heat of dilution and subtracted from the rest of the data. The lines represent the best fits to an independent mode. This figure was generated using the NanoAnalyze software provided by TA Instruments.

Determination of the Structure of HCA Bound to MtFBA

With the biochemical data proposing that HCA acts in a manner unlike that of current class II inhibitors of MtFBA, the X-ray crystallographic structure of HCA bound to MtFBA (MtFBA−HCA) was sought. Utilizing previous techniques to generate MtFBA in its zinc (II)-bound but substrate-less (holo-MtFBA) form, these crystals were soaked in HCA[118]. A crystal structure of these HCA-soaked crystals was subsequently resolved to 2.1 Å (Table 5.1). Not surprisingly, the single monomer in the asymmetric unit globally mirrored the TIM barrel fold of previous MtFBA structures and formed a tetrameric biological assembly with monomers from adjoining asymmetric units (Figures 5.3 and 5.4a). However, unlike the fully elucidated MtFBA−PGH structure that possessed density for the entire protein, two regions lacked electron density in the MtFBA−HCA structure (Figure 5.4a,b). One of these regions is the highly flexible active site loop comprised of amino acids 167−177, which contains Glu169 required for the deprotonation−protonation step of the MtFBA-facilitated reaction[118]. The absence of this loop was not particularly shocking as it has been resolved in only one class II FBA structure, that of MtFBA bound to PGH[118]. Conversely, the second region of MtFBA missing electron density, which encompassed the β6α6 loop containing residues 210−223, was unusual. This loop forms part of the substrate pocket and contains His212, whose imidazole side chain is involved in coordinating the active site Zn (II) ion and can be considered the zinc binding loop [Z-loop (Figure 5.4c)][118].

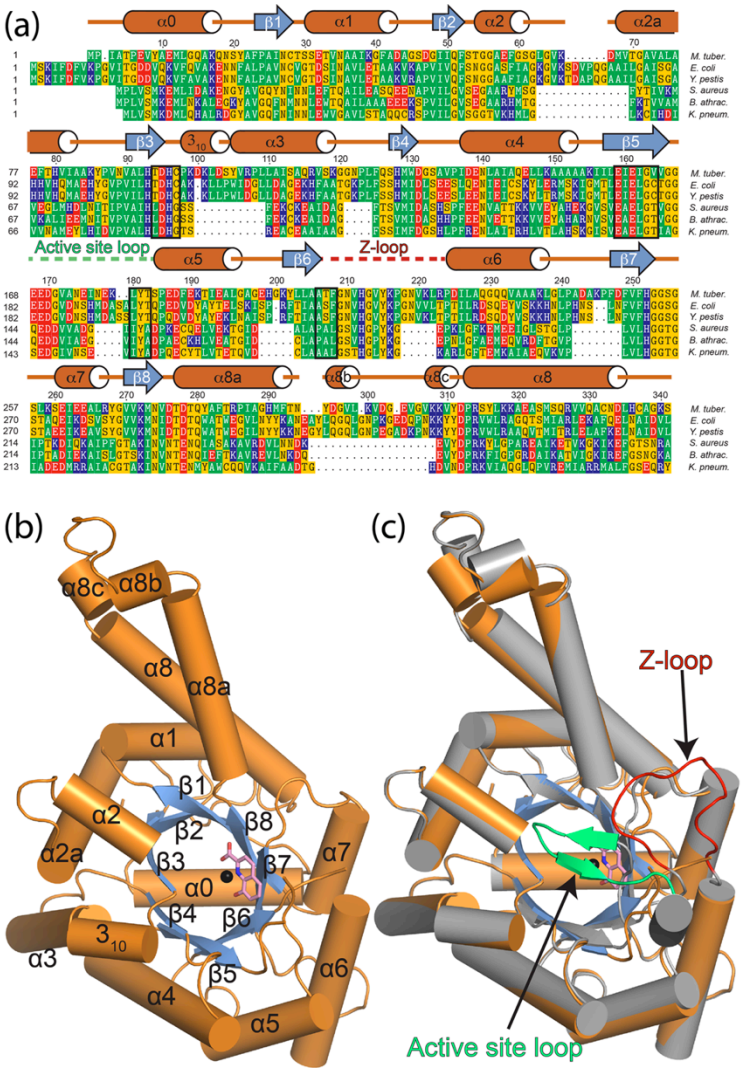

Figure 5.3. Sequence alignment of class II FBAs and X-ray structure of MtFBA in complex with HCA. (a) FBAs are from M. tuberculosis (*M. tuber*; NP_334786), *E. coli* (*E. coli*; PDB entry 1B57_A), *Yersinia pestis* (*Y. pestis*; ZP_04518851), *S. aureus* (*S. aureus*; Q5HE75), *Bacillus anthracis* (*B. anthrac*; PDB entry 3Q94_A), and *Klebsiella pneumoniae* (*K. pneum*; ZP_14594173). The secondary structure of the MtFBA−HCA complex according to Defined Secondary Structure of Proteins (DSSP) is shown as orange cylinders (helical regions), blue arrows (β-sheets), and orange lines (loops). Dashed lines represent residues for which electron density was not defined in the crystal structure. Breaks denote regions where MtFBA does not have residues. Black brackets indicate residues that are part of MtFBA's active site. (b) Cartoon rendering of the MtFBA−HCA protomer. Helical regions are represented as cylinders and β-strands as arrows. Helices and loops are colored orange and β-strands blue; HCA is shown as pink sticks, and zinc ion is shown as a black sphere. (c) Same MtFBA−HCA complex shown in panel b but overlaid with the MtFBA−PGH complex (PDB entry 4DEL) colored gray. Residues 167−177 (green) and 210−223 (red) for which density is observed in the MtFBA−PGH structure but not in the MtFBA−HCA structure.

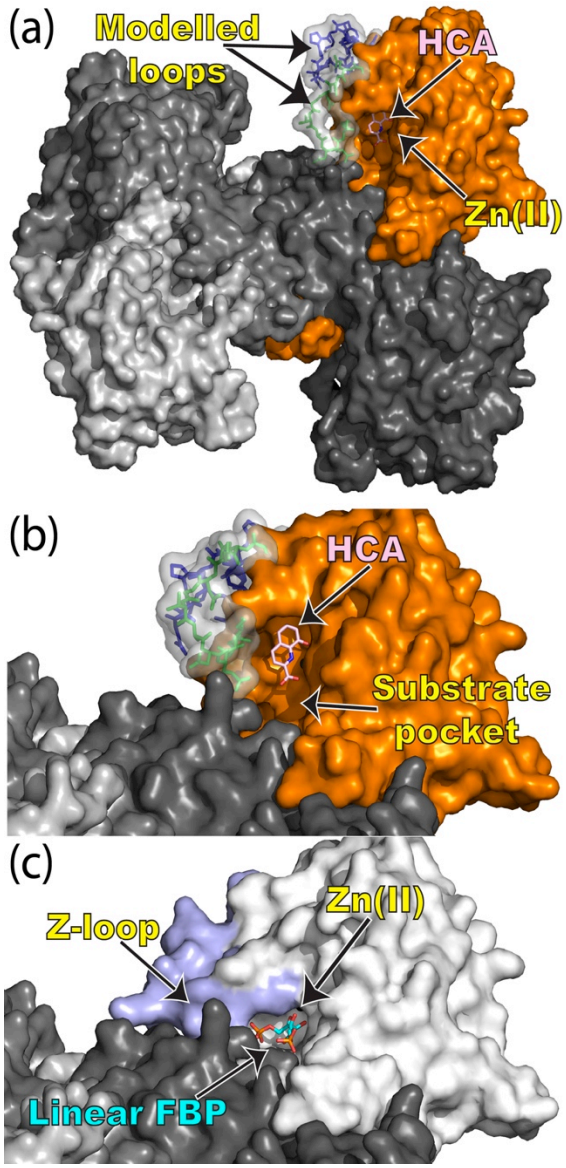

Figure 5.4. Rearrangement of the substrate pocket caused by HCA binding. (a) Surface rendering of the MtFBA−HCA complex as its tetrameric biological assembly with one MtFBA protomer colored orange, the rest colored various shades of gray, and HCA rendered as pink sticks. Loops that were modeled in due to a lack of electron density are shown as transparent surfaces and either green sticks (residues 167−177) or blue sticks (residues 210−223). (b) Close-up of the substrate binding pocket of the MtFBA−HCA complex. (c) Close-up of the substrate binding pocket for MtFBA (white) bound with linear fructose 1,6-bisphosphate (cyan sticks; PDB entry 3ELF), in which residues 210−223 are colored light blue. In all cases, the zinc ions are rendered as a black sphere.

Subsequently, closer inspection of the region where the Z-loop would typically reside, as well as the active site, readily revealed $F_o - F_c$ density of HCA coordinating the MtFBA's active site Zn(II) in a trident manner (Figure 5.5a and 5.6). Intriguingly, instead of accessing the active site Zn (II) through the highly polar and narrow substrate pocket of MtFBA, HCA appears to alter the active site. Specifically, it displaces the His212's imidazole side chain for the bound Zn (II). This creates a hydrophobic pocket that accommodates the bicyclic structure of HCA (Figure 5.5b). In addition to the displacement of His212, Val165, which is located on the flexible active site β5α5 loop, is also supplanted by HCA (Figure 5.5b)[118]. Although the X-ray data showed clear density for Val165, its position was shifted away from the active site. Beyond these alterations with the MtFBA active site, HCA forms three coordination bonds with Zn (II). As observed in previous MtFBA structures, two additional coordination bonds are formed between Zn (II) and histidine residues located at positions 96 and 252. Together, these interactions yield a coordination number of 5 (T_5) for the active site Zn similar to that of the PGH bound and different from the T_6 coordination found in the FBP structure (Figure 5.5a−c)[119]. In addition to the Zn(II)−HCA interactions, HCA forms a hydrogen bond (H-bond) with Glu161 of MtFBA as well as a network of H-bonds through water to Asp95 that further drives HCA stabilization within the altered active site (Figure 5.5a).

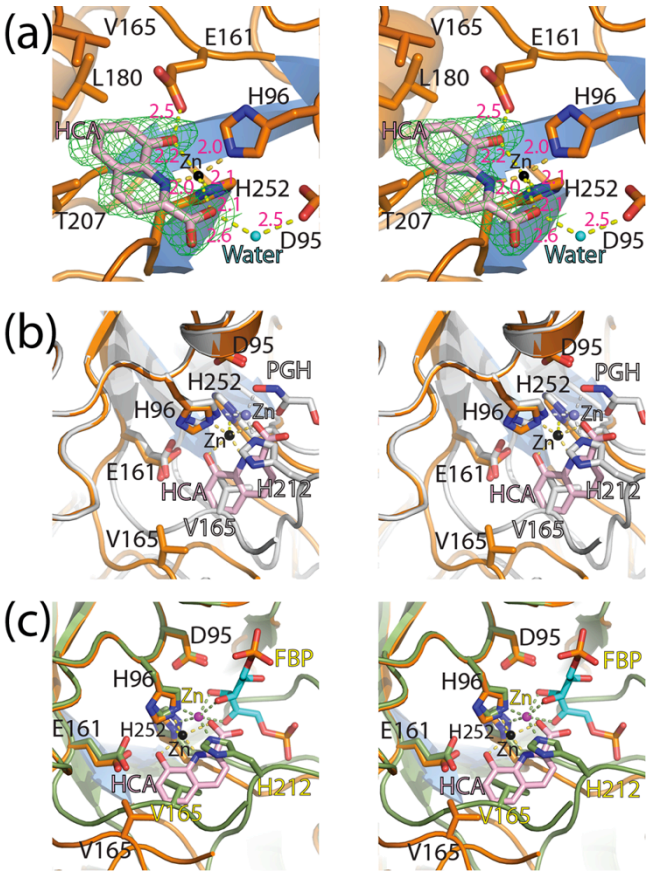

Figure 5.5. Comparison of the active sites of class II FBAs. (a) Wall-eyed stereoview close-up of HCA interacting with MtFBA and zinc. Green mesh represents $F_o - F_c$ density scaled to 3σ; black labels indicate MtFBA residues, and hot pink labels and dashed lines indicate distances measured in angstroms. (b) Wall-eyed stereoview of MtFBA (orange) bound to HCA (pink) interacting with Zn (black) overlaid with MtFBA interacting with PGH (gray; PDB entry 4DEL) and Zn (purple), with dashed lines indicating bonding interactions. (c) Wall-eyed stereoview of MtFBA bound to HCA interacting with Zn colored as in panel b overlaid with MtFBA (green) interacting with FBP (cyan; PDB entry 3ELF) and Zn (magenta) with dashed lines indicating bonding interactions.

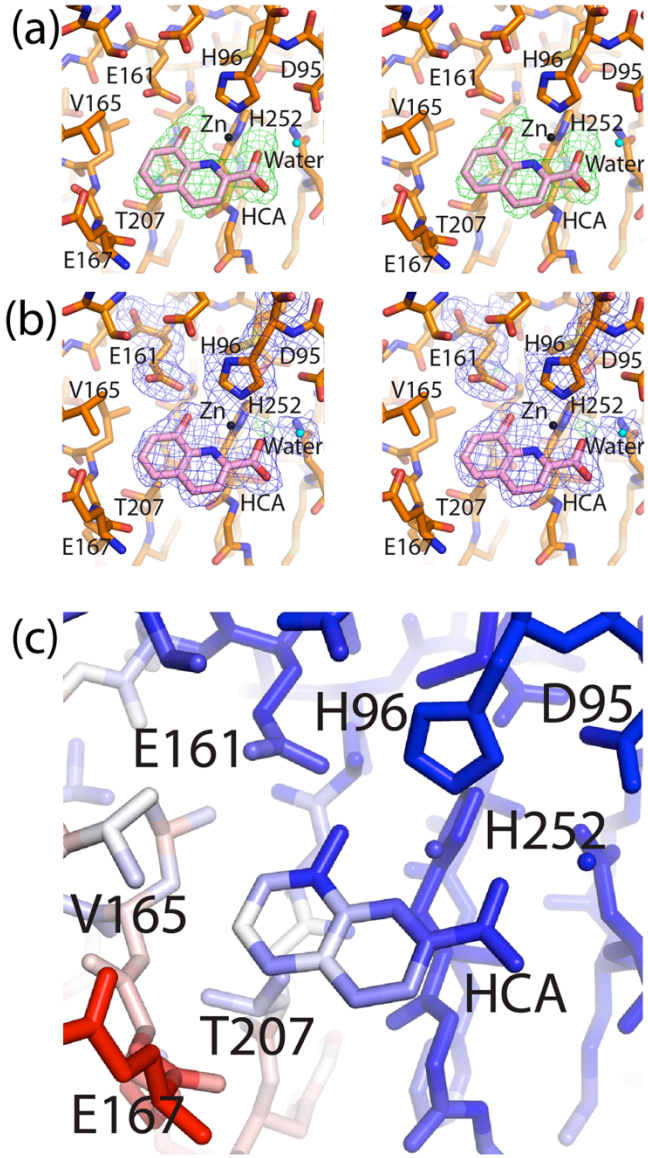

Figure 5.6. Omit maps and B-factors of atoms near HCA. (a) Wall-eyed stereo view close-up of MtFBA (orange) bound to HCA (pink) interacting with Zn (black). Green mesh represents a simulated annealing omit F_o-F_c map scaled to 3 σ. (b) Same as in (a) except blue mesh represents final $2F_o$-F_c map of HCA and adjacent residues scaled to 1.25 σ and green mesh represents final F_o-F_c map scaled to 3 σ. (c) B-factors of HCA and nearby atoms ranging from 25 (dark blue) to 75 (red).

Examining HCA's Specificity for Class I and II FBAs

As class II FBAs share considerable sequence similarity (Figure 5.3a), HCA's potential as a class II FBA broad-spectrum inhibitor was examined. A single concentration of HCA of 25 μM was tested for the inhibition of class II FBAs isolated from *E. coli* and methicillin-resistant *S. aureus* (MRSA). HCA demonstrated 42.2 ± 2.8% inhibition against *E. coli* and 64.3 ± 0.6% inhibition against MRSA (Figure 5.7). Conversely, class I FBAs are markedly different in sequence from class II FBAs and do not utilize a zinc (II) ion to perform their mechanistic function. Therefore, to investigate HCA's specificity for class II FBAs over class I FBAs, the class I FBAs isolated from both rabbit and human muscle were tested against HCA. Unlike class II FBAs, HCA showed no inhibitory effects against either class I FBA even at concentrations as high as 1 mM (Figure 5.7).

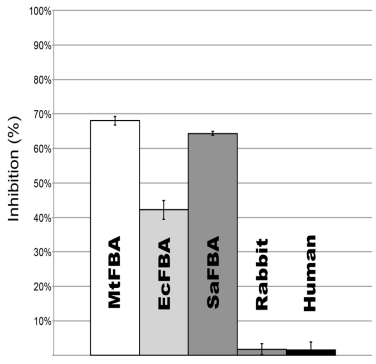

Figure 5.7. Effectiveness of HCA against class I FBAs and other class II FBAs. HCA at 25 μM was tested for its ability to inhibit class II FBAs from *E. coli* and MRSA as well as class I FBAs isolated from either rabbit or human muscle. Error bars represent the standard deviations from the average.

Discussion

HCA as a Noncompetitive MtFBA Inhibitor

The alignment of the MtFBA−HCA structure with those of MtFBA bound with FBP, or PGH, illustrates that HCA does not intrude into the substrate pocket itself (Figure 5.5b,c). Instead, incorporation of HCA into MtFBA appears to displace the Z-loop and in doing so blocks access of MtFBA substrates to an empty pocket (Figure 5.5b,c). The proximity of a noncompetitive inhibitor to a substrate pocket has been previously observed with a noncompetitive inhibitor, PD184352, of MAP kinase kinase 1 (MEK1)[155]. The noncompetitive nature of inhibition outlined by the mode of inhibition experiments combined with the structural data suggests that the MtFBA−HCA structure may be reflective of an EI complex found in the third model for noncompetitive inhibition (Figure 5.8a)[156]. In this model, the inhibitor binds next to the substrate-binding site with or without the substrate bound. When the substrate is absent, the inhibitor sterically hinders access of substrates to an empty site comparable to that observed in the structure of the MtFBA−HCA complex (Figure 5.8a). Also, the myriad of coordination bonds and H-bonds that HCA forms with MtFBA pulls the Zn (II) away from the substrate binding pocket. This would likely eliminate its availability for catalysis in an ESI complex in line with the third model of noncompetitive inhibition.

Use of HCA as a Scaffold for Future MtFBA Inhibitor Development

The persistence of tuberculosis along with the rise of many forms of drug resistant bacteria has supported the interest in identifying inhibitors for class II FBAs that may

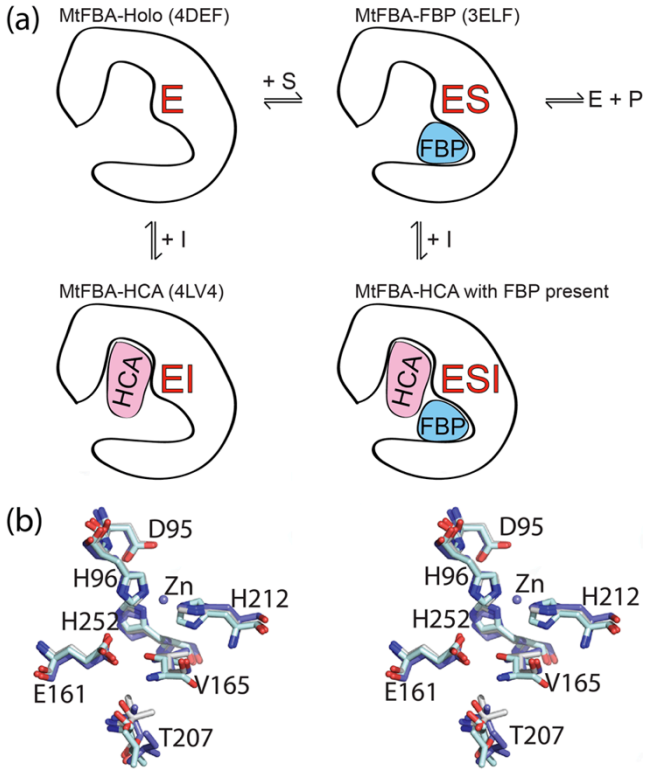

Figure 5.8. Proposed model of inhibition of HCA for MtFBA and applicability to other class II FBAs. (a) Cartoon adaptation of HCA's inhibition of MtFBA according to the third model for noncompetitive inhibition. (b) Wall-eyed stereoview of the overlay of FBAs from *M. tuberculosis* (gray; PDB entry 4DEL), *B. anthracis* (blue; PDB entry 3Q94), and *E. coli* (teal; PDB entry 1B57). Black labels indicate MtFBA residues.

serve as viable preclinical candidates for further development as antibiotic and antiparasitic treatments[110-113, 116-118, 141]. Although previous class II FBA inhibitor development efforts have been able to deliver potent substrate-based analogs selective for class II over class I FBAs, the recurring theme throughout studies utilizing class II FBA substrates as a scaffold is the necessity of these inhibitors to possess highly charged phosphate groups[112, 117, 141]. As phosphorylation of glycolytic intermediates is a method for cells to retain these intermediates within the cytosol, their inclusion into class II FBA inhibitors has been problematic[157]. In addition, the active site of class II FBA, which has evolved to interact with class II FBA's highly polar substrates, is itself highly polar, lacking appreciable potential for hydrophobic interactions. As this form of interaction typically dominates protein−drug interactions, targeting the class II FBA active site has proved to be daunting.

HCA sidesteps both of these issues through its distinct low-micromolar noncompetitive mode of inhibiting MtFBA. Specifically, HCA appears to take advantage of the previously overlooked fragility of the coordination of His212 of MtFBA of with Zn (II) along with the structural dependence of the Z-loop on that interaction to facilitate hydrophobic and hydrophilic contacts. At first glance, the substrate- and Zn (II)-bound MtFBA structures of Pegan et al., as well as the Zn(II)-bound holo-MFBA structure of Pegan et al., might have suggested that a stable interaction between His212 and an active site Zn (II) potentially existed[118, 119]. In addition, a zinc-less MtFBA apo structure of de la Paz Santangelo et al. illustrates that the ordered structure of the Z-loop depends on the presence of Zn (II) within the active site[111]. However, the MtFBA−HCA structure

suggests that even when Zn (II) is bound to the MtFBA active site, the interaction between His212 and the bound Zn (II) is still in flux. This flux allows HCA to supplant His212 with a trident coordination of the metal or a HCA−Zn(II) complex to replace the active site Zn (II). Naturally, additional experiments will likely be necessary to tease out which event is more likely. However, the MtFBA−HCA structure along with the biochemical and biophysical experiments illustrates that HCA prefers to be bound to MtFBA's active site Zn (II) and that this Zn (II) prefers HCA over His212.

From the MtFBA−HCA structure, this preference appears to be driven by not only a H-bond network formed by bonds from HCA to Asp95 and Glu161 of MtFBA that pulls Zn (II) away from the active site, but also hydrophobic interactions caused by the creation of a hydrophobic pocket that accommodates HCA's bicyclic ring structure (Figure 5.5b). As hydrophobic interactions are usually sought for protein−drug interactions and are a largely insignificant factor in the affinity of previous inhibitors for class II FBAs, the presence of this feature in MtFBA−HCA interactions is particularly noteworthy. In addition to HCA's distinct mode of inhibition, HCA possesses several features that make the compound attractive from a medicinal chemistry perspective. First, the compound has a low molecular mass of 189 Da and contains minimal structural features. Furthermore, functionality can be added at a variety of places on HCA while still likely maintaining druglike properties[152, 158, 159]. Also, HCA appears via the MtFBA−HCA structure to capitalize on the unique mechanistic difference between class I and class II FBAs by interacting with MtFBA active site zinc and residues immediately surrounding it. These residues along with Zn^{2+} do not exist in class I FBAs. This

combined with the lack of measurable inhibition of mammalian class I FBAs suggests the HCA scaffold could represent a significant leap forward in class II FBA preclinical inhibitor development.

Broad-Spectrum Potential of HCA

Interestingly, class II FBAs can be broken down into two families (a and b) whose distribution among bacteria is independent of Gram staining-determined phylogenetic groups. Naturally, all class II FBAs have an evolutionary need to maintain an effective active site that binds Zn (II) and a common set of substrates. As a result, the structural differences between these two subfamilies are predominantly distal from their respective active sites and are involved in determining the diverse oligomeric states adopted by class II FBAs[(119)]. This phenomenon is well represented upon comparison of residues that comprise the HCA-induced pocket (Figure 5.8b). Structural alignments of class IIa FBAs from *M. tuberculosis* and *E. coli* along with that of *B. anthracis's* class IIb FBA reinforce the potentially conserved nature of the HCA-induced pocket (Figure 5.8b). The ability of HCA to significantly inhibit both the class IIa FBA from *E. coli* and a class IIb FBA from MRSA further supports the potential use of the HCA scaffold for these bacteria. Of course, additional experiments with these or other class II FBAs will have to be conducted to fully confirm HCA is acting in a manner similar to that observed in MtFBA. However, the initial evidence bodes well for the broad-spectrum potential of the HCA scaffold in further class II FBA preclinical inhibitor design efforts.

Chapter 5 is in part a reprint of the material as it appears in Capodagli G. C., Sedhom W. G., Jackson M., Ahrendt, K. A., and Pegan S. D. (2014) *A Noncompetitive*

Inhibitor for Mycobacterium tuberculosis's Class IIa Fructose 1,6-Bisphosphate Aldolase. Biochemistry, **53**: 202-13. The dissertation author was primary researcher and author of this publication.

References

1. Baker, N. A., Sept, D., Joseph, S., Holst, M. J., and McCammon, J. A. (2001) Electrostatics of nanosystems: application to microtubules and the ribosome, *Proceedings of the National Academy of Sciences of the United States of America 98*, 10037-10041.

2. Schrodinger, LLC. (2010) The AxPyMOL Molecular Graphics Plugin for Microsoft PowerPoint, Version 1.0.

3. Schrodinger, LLC. (2010) The JyMOL Molecular Graphics Development Component, Version 1.0.

4. Schrodinger, LLC. (2010) The PyMOL Molecular Graphics System, Version 1.3r1.

5. Bailey, S. (1994) The Ccp4 Suite - Programs for Protein Crystallography, *Acta Crystallogr D 50*, 760-763.

6. van Dijk, A. D., Fushman, D., and Bonvin, A. M. (2005) Various strategies of using residual dipolar couplings in NMR-driven protein docking: application to Lys48-linked di-ubiquitin and validation against 15N-relaxation data, *Proteins 60*, 367-381.

7. Weeks, S. D., Grasty, K. C., Hernandez-Cuebas, L., and Loll, P. J. (2009) Crystal structures of Lys-63-linked tri- and di-ubiquitin reveal a highly extended chain architecture, *Proteins 77*, 753-759.

8. Deshaies, R. J., and Joazeiro, C. A. (2009) RING domain E3 ubiquitin ligases, *Annu Rev Biochem 78*, 399-434.

9. Schulman, B. A., and Harper, J. W. (2009) Ubiquitin-like protein activation by E1 enzymes: the apex for downstream signalling pathways, *Nat Rev Mol Cell Biol 10*, 319-331.

10. Ye, Y., and Rape, M. (2009) Building ubiquitin chains: E2 enzymes at work, *Nat Rev Mol Cell Biol 10*, 755-764.

11. Bergink, S., and Jentsch, S. (2009) Principles of ubiquitin and SUMO modifications in DNA repair, *Nature 458*, 461-467.

12. Haglund, K., Di Fiore, P. P., and Dikic, I. (2003) Distinct monoubiquitin signals in receptor endocytosis, *Trends Biochem Sci 28*, 598-603.

13. Hicke, L. (2001) Protein regulation by monoubiquitin, *Nat Rev Mol Cell Biol 2*, 195-201.

14. Passmore, L. A., and Barford, D. (2004) Getting into position: the catalytic mechanisms of protein ubiquitylation, *Biochem J 379*, 513-525.

15. Haglund, K., Sigismund, S., Polo, S., Szymkiewicz, I., Di Fiore, P. P., and Dikic, I. (2003) Multiple monoubiquitination of RTKs is sufficient for their endocytosis and degradation, *Nature cell biology 5*, 461-466.

16. Komander, D., Clague, M. J., and Urbe, S. (2009) Breaking the chains: structure and function of the deubiquitinases, *Nat Rev Mol Cell Biol 10*, 550-563.

17. Xu, P., Duong, D. M., Seyfried, N. T., Cheng, D., Xie, Y., Robert, J., Rush, J., Hochstrasser, M., Finley, D., and Peng, J. (2009) Quantitative proteomics reveals the function of unconventional ubiquitin chains in proteasomal degradation, *Cell 137*, 133-145.

18. Matsumoto, M. L., Wickliffe, K. E., Dong, K. C., Yu, C., Bosanac, I., Bustos, D., Phu, L., Kirkpatrick, D. S., Hymowitz, S. G., Rape, M., Kelley, R. F., and Dixit, V. M. (2010) K11-linked polyubiquitination in cell cycle control revealed by a K11 linkage-specific antibody, *Mol Cell 39*, 477-484.

19. Arimoto, K., Funami, K., Saeki, Y., Tanaka, K., Okawa, K., Takeuchi, O., Akira, S., Murakami, Y., and Shimotohno, K. (2010) Polyubiquitin conjugation to NEMO by triparite motif protein 23 (TRIM23) is critical in antiviral defense, *Proceedings of the National Academy of Sciences of the United States of America 107*, 15856-15861.

20. Shang, F., Deng, G., Liu, Q., Guo, W., Haas, A. L., Crosas, B., Finley, D., and Taylor, A. (2005) Lys6-modified ubiquitin inhibits ubiquitin-dependent protein degradation, *J Biol Chem 280*, 20365-20374.

21. Zucchelli, S., Codrich, M., Marcuzzi, F., Pinto, M., Vilotti, S., Biagioli, M., Ferrer, I., and Gustincich, S. (2010) TRAF6 promotes atypical ubiquitination of mutant DJ-1 and alpha-synuclein and is localized to Lewy bodies in sporadic Parkinson's disease brains, *Hum Mol Genet 19*, 3759-3770.

22. Herrmann, J., Lerman, L. O., and Lerman, A. (2007) Ubiquitin and ubiquitin-like proteins in protein regulation, *Circ Res 100*, 1276-1291.

23. Pickart, C. M., and Cohen, R. E. (2004) Proteasomes and their kin: proteases in the machine age, *Nat Rev Mol Cell Biol 5*, 177-187.

24. Versteeg, G. A., and Garcia-Sastre, A. (2010) Viral tricks to grid-lock the type I interferon system, *Current opinion in microbiology 13*, 508-516.

25. Weber, F., and Mirazimi, A. (2008) Interferon and cytokine responses to Crimean Congo hemorrhagic fever virus; an emerging and neglected viral zonoosis, *Cytokine Growth Factor Rev 19*, 395-404.

26. Zhao, C., Denison, C., Huibregtse, J. M., Gygi, S., and Krug, R. M. (2005) Human ISG15 conjugation targets both IFN-induced and constitutively expressed proteins functioning in diverse cellular pathways, *Proceedings of the National Academy of Sciences of the United States of America 102*, 10200-10205.

27. Ha, B. H., and Kim, E. E. (2008) Structures of proteases for ubiqutin and ubiquitin-like modifiers, *BMB Rep 41*, 435-443.

28. Morales, D. J., and Lenschow, D. J. (2013) The antiviral activities of ISG15, *J Mol Biol 425*, 4995-5008.

29. Petroski, M. D., and Deshaies, R. J. (2005) Function and regulation of cullin-RING ubiquitin ligases, *Nat Rev Mol Cell Biol 6*, 9-20.

30. Kamitani, T., Kito, K., Nguyen, H. P., and Yeh, E. T. (1997) Characterization of NEDD8, a developmentally down-regulated ubiquitin-like protein, *J Biol Chem 272*, 28557-28562.

31. Eletr, Z. M., and Wilkinson, K. D. (2014) Regulation of proteolysis by human deubiquitinating enzymes, *Biochim Biophys Acta 1843*, 114-128.

32. Komander, D., Reyes-Turcu, F., Licchesi, J. D., Odenwaelder, P., Wilkinson, K. D., and Barford, D. (2009) Molecular discrimination of structurally equivalent Lys 63-linked and linear polyubiquitin chains, *EMBO reports 10*, 466-473.

33. Basters, A., Geurink, P. P., El Oualid, F., Ketscher, L., Casutt, M. S., Krause, E., Ovaa, H., Knobeloch, K. P., and Fritz, G. (2014) Molecular characterization of ubiquitin-specific protease 18 reveals substrate specificity for interferon-stimulated gene 15, *The FEBS journal 281*, 1918-1928.

34. Bremm, A., Freund, S. M., and Komander, D. (2010) Lys11-linked ubiquitin chains adopt compact conformations and are preferentially hydrolyzed by the deubiquitinase Cezanne, *Nature structural & molecular biology 17*, 939-947.

35. Winborn, B. J., Travis, S. M., Todi, S. V., Scaglione, K. M., Xu, P., Williams, A. J., Cohen, R. E., Peng, J., and Paulson, H. L. (2008) The deubiquitinating enzyme ataxin-3, a polyglutamine disease protein, edits Lys63 linkages in mixed linkage ubiquitin chains, *J Biol Chem 283*, 26436-26443.

36. Yao, T., and Cohen, R. E. (2002) A cryptic protease couples deubiquitination and degradation by the proteasome, *Nature 419*, 403-407.

37. Edelmann, M. J., Iphofer, A., Akutsu, M., Altun, M., di Gleria, K., Kramer, H. B., Fiebiger, E., Dhe-Paganon, S., and Kessler, B. M. (2009) Structural basis and specificity of human otubain 1-mediated deubiquitination, *Biochem J 418*, 379-390.

38. Kayagaki, N., Phung, Q., Chan, S., Chaudhari, R., Quan, C., O'Rourke, K. M., Eby, M., Pietras, E., Cheng, G., Bazan, J. F., Zhang, Z., Arnott, D., and Dixit, V. M. (2007) DUBA: a deubiquitinase that regulates type I interferon production, *Science 318*, 1628-1632.

39. Frias-Staheli, N., Giannakopoulos, N. V., Kikkert, M., Taylor, S. L., Bridgen, A., Paragas, J., Richt, J. A., Rowland, R. R., Schmaljohn, C. S., Lenschow, D. J., Snijder, E. J., Garcia-Sastre, A., and Virgin, H. W. t. (2007) Ovarian tumor domain-containing viral proteases evade ubiquitin- and ISG15-dependent innate immune responses, *Cell host & microbe 2*, 404-416.

40. Bergeron, E., Albarino, C. G., Khristova, M. L., and Nichol, S. T. (2010) Crimean-Congo hemorrhagic fever virus-encoded ovarian tumor protease activity is dispensable for virus RNA polymerase function, *Journal of virology 84*, 216-226.

41. Komander, D., and Barford, D. (2008) Structure of the A20 OTU domain and mechanistic insights into deubiquitination, *Biochem J 409*, 77-85.

42. Nanao, M. H., Tcherniuk, S. O., Chroboczek, J., Dideberg, O., Dessen, A., and Balakirev, M. Y. (2004) Crystal structure of human otubain 2, *EMBO reports 5*, 783-788.

43. Messick, T. E., Russell, N. S., Iwata, A. J., Sarachan, K. L., Shiekhattar, R., Shanks, J. R., Reyes-Turcu, F. E., Wilkinson, K. D., and Marmorstein, R. (2008) Structural basis for ubiquitin recognition by the Otu1 ovarian tumor domain protein, *J Biol Chem 283*, 11038-11049.

44. Clementz, M. A., Chen, Z., Banach, B. S., Wang, Y., Sun, L., Ratia, K., Baez-Santos, Y. M., Wang, J., Takayama, J., Ghosh, A. K., Li, K., Mesecar, A. D., and Baker, S. C. (2010) Deubiquitinating and interferon antagonism activities of coronavirus papain-like proteases, *Journal of virology 84*, 4619-4629.

45. Zhao, C., Hsiang, T. Y., Kuo, R. L., and Krug, R. M. (2010) ISG15 conjugation system targets the viral NS1 protein in influenza A virus-infected cells, *Proceedings of the National Academy of Sciences of the United States of America 107*, 2253-2258.

46. Chenon, M., Camborde, L., Cheminant, S., and Jupin, I. (2011) A viral deubiquitylating enzyme targets viral RNA-dependent RNA polymerase and affects viral infectivity, *EMBO J 31*, 741-753.

47. Zhang, H. M., Yang, J., Sun, H. R., Xin, X., Wang, H. D., Chen, J. P., and Adams, M. J. (2007) Genomic analysis of rice stripe virus Zhejiang isolate shows the presence of an OTU-like domain in the RNA1 protein and a novel sequence motif conserved within the intergenic regions of ambisense segments of tenuiviruses, *Arch Virol 152*, 1917-1923.

48. Morikawa, S., Saijo, M., and Kurane, I. (2007) Recent progress in molecular biology of Crimean-Congo hemorrhagic fever, *Comparative immunology, microbiology and infectious diseases 30*, 375-389.

49. World_Health_Organization. (2001) Crimean-Congo haemorrhagic fever, (Organization, W. H., Ed.), WHO Media Centre.

50. Karti, S. S., Odabasi, Z., Korten, V., Yilmaz, M., Sonmez, M., Caylan, R., Akdogan, E., Eren, N., Koksal, I., Ovali, E., Erickson, B. R., Vincent, M. J., Nichol, S. T., Comer, J. A., Rollin, P. E., and Ksiazek, T. G. (2004) Crimean-Congo hemorrhagic fever in Turkey, *Emerging infectious diseases 10*, 1379-1384.

51. Ozkaya, E., Dincer, E., Carhan, A., Uyar, Y., Ertek, M., Whitehouse, C. A., and Ozkul, A. (2010) Molecular epidemiology of Crimean-Congo hemorrhagic fever virus in Turkey: Occurrence of local topotype, *Virus research*.

52. World_Health_Organization. (2003) Crimean-Congo haemorrhagic fever (CCHF) in Mauritania - Update, In *Disease Outbreak Report*, World Health Organization.

53. Sadler, A. J., and Williams, B. R. (2008) Interferon-inducible antiviral effectors, *Nat Rev Immunol 8*, 559-568.

54. Lenschow, D. J., Lai, C., Frias-Staheli, N., Giannakopoulos, N. V., Lutz, A., Wolff, T., Osiak, A., Levine, B., Schmidt, R. E., Garcia-Sastre, A., Leib, D. A., Pekosz, A., Knobeloch, K. P., Horak, I., and Virgin, H. W. t. (2007) IFN-stimulated gene 15 functions as a critical antiviral molecule against influenza, herpes, and Sindbis viruses, *Proceedings of the National Academy of Sciences of the United States of America 104*, 1371-1376.

55. Al-Hakim, A. K., Zagorska, A., Chapman, L., Deak, M., Peggie, M., and Alessi, D. R. (2008) Control of AMPK-related kinases by USP9X and atypical Lys(29)/Lys(33)-linked polyubiquitin chains, *Biochem J 411*, 249-260.

56. Chastagner, P., Israel, A., and Brou, C. (2006) Itch/AIP4 mediates Deltex degradation through the formation of K29-linked polyubiquitin chains, *EMBO reports 7*, 1147-1153.

57. Sun, L., and Chen, Z. J. (2004) The novel functions of ubiquitination in signaling, *Current opinion in cell biology 16*, 119-126.

58. Arguello, M. D., and Hiscott, J. (2007) Ub surprised: viral ovarian tumor domain proteases remove ubiquitin and ISG15 conjugates, *Cell host & microbe 2*, 367-369.

59. Lessel, U., and Schomburg, D. (1994) Similarities between Protein 3-D Structures, *Protein Eng 7*, 1175-1187.

60. Wilkinson, K. D., Gan-Erdene, T., and Kolli, N. (2005) Derivitization of the C-terminus of ubiquitin and ubiquitin-like proteins using intein chemistry: methods and uses, *Methods Enzymol 399*, 37-51.

61. Gill, S. C., and von Hippel, P. H. (1989) Calculation of protein extinction coefficients from amino acid sequence data, *Analytical biochemistry 182*, 319-326.

62. Otwinowski, Z., and Minor, W. (1997) Processing of X-ray diffraction data collected in oscillation mode, *Macromolecular Crystallography, Pt A 276*, 307-326.

63. Grosse-Kunstleve, R. W., and Adams, P. D. (2003) Substructure search procedures for macromolecular structures, *Acta crystallographica. Section D, Biological crystallography 59*, 1966-1973.

64. McCoy, A. J., Grosse-Kunstleve, R. W., Adams, P. D., Winn, M. D., Storoni, L. C., and Read, R. J. (2007) Phaser crystallographic software, *Journal of applied crystallography 40*, 658-674.

65. Terwilliger, T. C., Adams, P. D., Read, R. J., Mccoy, A. J., Moriarty, N. W., Grosse-Kunstleve, R. W., Afonine, P. V., Zwart, P. H., and Hung, L. W. (2009) Decision-making in structure solution using Bayesian estimates of map quality: the PHENIX AutoSol wizard, *Acta Crystallogr D 65*, 582-601.

66. Adams, P. D., Afonine, P. V., Bunkoczi, G., Chen, V. B., Davis, I. W., Echols, N., Headd, J. J., Hung, L. W., Kapral, G. J., Grosse-Kunstleve, R. W., McCoy, A. J., Moriarty, N. W., Oeffner, R., Read, R. J., Richardson, D. C., Richardson, J. S., Terwilliger, T. C., and Zwart, P. H. (2010) PHENIX: a comprehensive Python-based system for macromolecular structure solution, *Acta Crystallogr D 66*, 213-221.

67. Emsley, P., and Cowtan, K. (2004) Coot: model-building tools for molecular graphics, *Acta Crystallogr D 60*, 2126-2132.

68. Murshudov, G. N., Vagin, A. A., and Dodson, E. J. (1997) Refinement of macromolecular structures by the maximum-likelihood method, *Acta Crystallogr D 53*, 240-255.

69. Datta, A. B., Hura, G. L., and Wolberger, C. (2009) The structure and conformation of Lys63-linked tetraubiquitin, *J Mol Biol 392*, 1117-1124.

70. Snijder, E. J., Wassenaar, A. L., Spaan, W. J., and Gorbalenya, A. E. (1995) The arterivirus Nsp2 protease. An unusual cysteine protease with primary structure similarities to both papain-like and chymotrypsin-like proteases, *J Biol Chem 270*, 16671-16676.

71. Duh, D., Nichol, S. T., Khristova, M. L., Saksida, A., Hafner-Bratkovic, I., Petrovec, M., Dedushaj, I., Ahmeti, S., and Avsic-Zupanc, T. (2008) The complete genome sequence of a Crimean-Congo hemorrhagic fever virus isolated from an endemic region in Kosovo, *Virology journal 5*, 7.

72. Anagnostou, V., and Papa, A. (2009) Evolution of Crimean-Congo Hemorrhagic Fever virus, *Infection, genetics and evolution : journal of molecular epidemiology and evolutionary genetics in infectious diseases 9*, 948-954.

73. Meissner, J. D., Seregin, S. S., Seregin, S. V., Vyshemirskii, O. I., Samokhvalov, E. I., Lvov, D. K., Netesov, S. V., and Petrov, V. S. (2006) A variable region in the Crimean-Congo hemorrhagic fever virus L segment distinguishes between strains isolated from different geographic regions, *Journal of medical virology 78*, 223-228.

74. Schlieker, C., Weihofen, W. A., Frijns, E., Kattenhorn, L. M., Gaudet, R., and Ploegh, H. L. (2007) Structure of a herpesvirus-encoded cysteine protease reveals a unique class of deubiquitinating enzymes, *Mol Cell 25*, 677-687.

75. Mishra, A. C., Mehta, M., Mourya, D. T., and Gandhi, S. (2011) Crimean-Congo haemorrhagic fever in India, *Lancet 378*, 372.

76. Nalca, A., Whitehouse, C. A., Ergonul, O., and Whitehouse, C. A., (Eds.) (2007) *Crimean-Congo Hemorrhagic Fever*, Springer Netherlands, Dordrecht.

77. Burt, F. J., Spencer, D. C., Leman, P. A., Patterson, B., and Swanepoel, R. (1996) Investigation of tick-borne viruses as pathogens of humans in South Africa and evidence of Dugbe virus infection in a patient with prolonged thrombocytopenia, *Epidemiol Infect 116*, 353-361.

78. Dandawate, C. N., Work, T. H., Webb, J. K., and Shah, K. V. (1969) Isolation of Ganjam virus from a human case of febrile illness: a report of a laboratory infection and serological survey of human sera from three different states of India, *Indian J Med Res 57*, 975-982.

79. Marczinke, B. I., and Nichol, S. T. (2002) Nairobi sheep disease virus, an important tick-borne pathogen of sheep and goats in Africa, is also present in Asia, *Virology 303*, 146-151.

80. Sudeep, A. B., Jadi, R. S., and Mishra, A. C. (2009) Ganjam virus, *Indian J Med Res 130*, 514-519.

81. Sang, R., Onyango, C., Gachoya, J., Mabinda, E., Konongoi, S., Ofula, V., Dunster, L., Okoth, F., Coldren, R., Tesh, R., da Rossa, A. T., Finkbeiner, S., Wang, D., Crabtree, M., and Miller, B. (2006) Tickborne arbovirus surveillance in market livestock, Nairobi, Kenya, *Emerging infectious diseases 12*, 1074-1080.

82. Steele, G. M., and Nuttall, P. A. (1989) Difference in vector competence of two species of sympatric ticks, Amblyomma variegatum and Rhipicephalus appendiculatus, for Dugbe virus (Nairovirus, Bunyaviridae), *Virus research 14*, 73-84.

83. Dilcher, M., Koch, A., Hasib, L., Dobler, G., Hufert, F., and Weidmann, M. (2012) Genetic characterization of Erve virus, a European Nairovirus distantly related to Crimean-Congo hemorrhagic fever virus, *Virus Genes*, 1-7.

84. Akutsu, M., Ye, Y., Virdee, S., Chin, J. W., and Komander, D. (2010) Molecular basis for ubiquitin and ISG15 cross-reactivity in viral ovarian tumor domains, *Proceedings of the National Academy of Sciences of the United States of America 108*, 2228-2233.

85. Capodagli, G. C., McKercher, M. A., Baker, E. A., Masters, E. M., Brunzelle, J. S., and Pegan, S. D. (2011) Structural analysis of a viral ovarian tumor domain protease from the Crimean-Congo hemorrhagic fever virus in complex with covalently bonded ubiquitin, *Journal of virology 85*, 3621-3630.

86. Edelmann, M. J., and Kessler, B. M. (2008) Ubiquitin and ubiquitin-like specific proteases targeted by infectious pathogens: Emerging patterns and molecular principles, *Biochim Biophys Acta 1782*, 809-816.

87. Bridgen, A., Weber, F., Fazakerley, J. K., and Elliott, R. M. (2001) Bunyamwera bunyavirus nonstructural protein NSs is a nonessential gene product that contributes to viral pathogenesis, *Proceedings of the National Academy of Sciences of the United States of America 98*, 664-669.

88. Giorgi, C., Accardi, L., Nicoletti, L., Gro, M. C., Takehara, K., Hilditch, C., Morikawa, S., and Bishop, D. H. (1991) Sequences and coding strategies of the S RNAs of Toscana and Rift Valley fever viruses compared to those of Punta Toro, Sicilian Sandfly fever, and Uukuniemi viruses, *Virology 180*, 738-753.

89. Komander, D., and Rape, M. (2012) The ubiquitin code, *Annu Rev Biochem 81*, 203-229.

90. Huang, H., Jeon, M. S., Liao, L., Yang, C., Elly, C., Yates, J. R., 3rd, and Liu, Y. C. (2010) K33-linked polyubiquitination of T cell receptor-zeta regulates proteolysis-independent T cell signaling, *Immunity 33*, 60-70.

91. Peyrefitte, C. N., Perret, M., Garcia, S., Rodrigues, R., Bagnaud, A., Lacote, S., Crance, J. M., Vernet, G., Garin, D., Bouloy, M., and Paranhos-Baccala, G. (2010) Differential activation profiles of Crimean-Congo hemorrhagic fever virus- and Dugbe virus-infected antigen-presenting cells, *The Journal of general virology 91*, 189-198.

92. Rodrigues, R., Paranhos-Baccala, G., Vernet, G., and Peyrefitte, C. N. (2012) Crimean-Congo hemorrhagic fever virus-infected hepatocytes induce ER-stress and apoptosis crosstalk, *PLoS One 7*, e29712.

93. Holzer, B., Bakshi, S., Bridgen, A., and Baron, M. D. (2011) Inhibition of interferon induction and action by the nairovirus Nairobi sheep disease virus/Ganjam virus, *PLoS One 6*, e28594.

94. Bakshi, S., Holzer, B., Bridgen, A., McMullan, G., Quinn, D. G., and Baron, M. D. (2013) Dugbe virus ovarian tumour domain interferes with ubiquitin/ISG15-regulated innate immune cell signalling, *The Journal of general virology 94*, 298-307.

95. Emsley, P., and Cowtan, K. (2004) Coot: model-building tools for molecular graphics, *Acta crystallographica. Section D, Biological crystallography 60*, 2126-2132.

96. James, T. W., Frias-Staheli, N., Bacik, J. P., Levingston Macleod, J. M., Khajehpour, M., Garcia-Sastre, A., and Mark, B. L. (2011) Structural basis for the removal of ubiquitin and interferon-stimulated gene 15 by a viral ovarian tumor domain-containing protease, *Proceedings of the National Academy of Sciences of the United States of America 108*, 2222-2227.

97. Deyde, V. M., Khristova, M. L., Rollin, P. E., Ksiazek, T. G., and Nichol, S. T. (2006) Crimean-Congo hemorrhagic fever virus genomics and global diversity, *Journal of virology 80*, 8834-8842.

98. Huang, O. W., Ma, X., Yin, J., Flinders, J., Maurer, T., Kayagaki, N., Phung, Q., Bosanac, I., Arnott, D., Dixit, V. M., Hymowitz, S. G., Starovasnik, M. A., and Cochran, A. G. (2012) Phosphorylation-dependent activity of the deubiquitinase DUBA, *Nature structural & molecular biology 19*, 171-175.

99. van Kasteren, P. B., Beugeling, C., Ninaber, D. K., Frias-Staheli, N., van Boheemen, S., Garcia-Sastre, A., Snijder, E. J., and Kikkert, M. (2012) Arterivirus and nairovirus ovarian tumor domain-containing Deubiquitinases

target activated RIG-I to control innate immune signaling, *Journal of virology 86*, 773-785.

100. Treib, J., Dobler, G., Haass, A., von Blohn, W., Strittmatter, M., Pindur, G., Froesner, G., and Schimrigk, K. (1998) Thunderclap headache caused by Erve virus?, *Neurology 50*, 509-511.

101. Barretto, N., Jukneliene, D., Ratia, K., Chen, Z., Mesecar, A. D., and Baker, S. C. (2005) The papain-like protease of severe acute respiratory syndrome coronavirus has deubiquitinating activity, *Journal of virology 79*, 15189-15198.

102. Ratia, K. (2008) Structure, function, and inhibition of the papain-like protease from SARS coronavirus, pp xx, 231 leaves.

103. Bogunovic, D., Byun, M., Durfee, L. A., Abhyankar, A., Sanal, O., Mansouri, D., Salem, S., Radovanovic, I., Grant, A. V., Adimi, P., Mansouri, N., Okada, S., Bryant, V. L., Kong, X. F., Kreins, A., Velez, M. M., Boisson, B., Khalilzadeh, S., Ozcelik, U., Darazam, I. A., Schoggins, J. W., Rice, C. M., Al-Muhsen, S., Behr, M., Vogt, G., Puel, A., Bustamante, J., Gros, P., Huibregtse, J. M., Abel, L., Boisson-Dupuis, S., and Casanova, J. L. (2012) Mycobacterial disease and impaired IFN-gamma immunity in humans with inherited ISG15 deficiency, *Science 337*, 1684-1688.

104. Capodagli, G. C., Deaton, M. K., Baker, E. A., Lumpkin, R. J., and Pegan, S. D. (2013) Diversity of ubiquitin and ISG15 specificity among nairoviruses' viral ovarian tumor domain proteases, *Journal of virology 87*, 3815-3827.

105. World Health Organization. (2008) *Global tuberculossis control -surveillance, planning, financing*, World Health Organization, Geneva, Switzerland.

106. World Health Organization. (2012) *Global tuberculosis report 2012 (in IRIS)*, World Health Organization, Geneva.

107. World Health Organization., UNAIDS., and UNICEF. (2011) *Global HIV/AIDS response : epidemic update and health sector progress towards universal access : progress report 2011*, World Health Organization, Geneva.

108. World Health Organization. (2008) *Implementing the Stop TB Strategy: a handbook for national tuberculosis*, World Health Organization, Geneva, Switzerland.

109. World Health Organization. (2008) *Tuberculosis MDR-TB & XDR-TB*, World Health Organization, Geneva, Switzerland.

110. Daher, R., Coincon, M., Fonvielle, M., Gest, P. M., Guerin, M. E., Jackson, M., Sygusch, J., and Therisod, M. (2010) Rational design, synthesis, and evaluation of

new selective inhibitors of microbial class II (zinc dependent) fructose bis-phosphate aldolases, *Journal of medicinal chemistry 53*, 7836-7842.

111. de la Paz Santangelo, M., Gest, P. M., Guerin, M. E., Coincon, M., Pham, H., Ryan, G., Puckett, S. E., Spencer, J. S., Gonzalez-Juarrero, M., Daher, R., Lenaerts, A. J., Schnappinger, D., Therisod, M., Ehrt, S., Sygusch, J., and Jackson, M. (2011) Glycolytic and non-glycolytic functions of Mycobacterium tuberculosis fructose-1,6-bisphosphate aldolase, an essential enzyme produced by replicating and non-replicating bacilli, *J Biol Chem 286*, 40219-40231.

112. Fonvielle, M., Coincon, M., Daher, R., Desbenoit, N., Kosieradzka, K., Barilone, N., Gicquel, B., Sygusch, J., Jackson, M., and Therisod, M. (2008) Synthesis and biochemical evaluation of selective inhibitors of class II fructose bisphosphate aldolases: towards new synthetic antibiotics, *Chemistry 14*, 8521-8529.

113. Fonvielle, M., Weber, P., Dabkowska, K., and Therisod, M. (2004) New highly selective inhibitors of class II fructose-1,6-bisphosphate aldolases, *Bioorg Med Chem Lett 14*, 2923-2926.

114. Galkin, A., Li, Z., Li, L., Kulakova, L., Pal, L. R., Dunaway-Mariano, D., and Herzberg, O. (2009) Structural insights into the substrate binding and stereoselectivity of giardia fructose-1,6-bisphosphate aldolase, *Biochemistry 48*, 3186-3196.

115. Gerdes, S. Y., Scholle, M. D., Campbell, J. W., Balazsi, G., Ravasz, E., Daugherty, M. D., Somera, A. L., Kyrpides, N. C., Anderson, I., Gelfand, M. S., Bhattacharya, A., Kapatral, V., D'Souza, M., Baev, M. V., Grechkin, Y., Mseeh, F., Fonstein, M. Y., Overbeek, R., Barabasi, A. L., Oltvai, Z. N., and Osterman, A. L. (2003) Experimental determination and system level analysis of essential genes in Escherichia coli MG1655, *J Bacteriol 185*, 5673-5684.

116. Labbe, G., Krismanich, A. P., de Groot, S., Rasmusson, T., Shang, M., Brown, M. D., Dmitrienko, G. I., and Guillemette, J. G. (2012) Development of metal-chelating inhibitors for the Class II fructose 1,6-bisphosphate (FBP) aldolase, *Journal of inorganic biochemistry 112*, 49-58.

117. Li, Z., Liu, Z., Cho, D. W., Zou, J., Gong, M., Breece, R. M., Galkin, A., Li, L., Zhao, H., Maestas, G. D., Tierney, D. L., Herzberg, O., Dunaway-Mariano, D., and Mariano, P. S. (2011) Rational design, synthesis and evaluation of first generation inhibitors of the Giardia lamblia fructose-1,6-biphosphate aldolase, *Journal of inorganic biochemistry 105*, 509-517.

118. Pegan, S. D., Rukseree, K., Capodagli, G. C., Baker, E. A., Krasnykh, O., Franzblau, S. G., and Mesecar, A. D. (2013) Active site loop dynamics of a class IIa fructose 1,6-bisphosphate aldolase from Mycobacterium tuberculosis, *Biochemistry 52*, 912-925.

119. Pegan, S. D., Rukseree, K., Franzblau, S. G., and Mesecar, A. D. (2009) Structural basis for catalysis of a tetrameric class IIa fructose 1,6-bisphosphate aldolase from Mycobacterium tuberculosis, *J Mol Biol 386*, 1038-1053.

120. Ramsaywak, P. C., Labbe, G., Siemann, S., Dmitrienko, G. I., and Guillemette, J. G. (2004) Molecular cloning, expression, purification, and characterization of fructose 1,6-bisphosphate aldolase from Mycobacterium tuberculosis--a novel Class II A tetramer, *Protein Expr Purif 37*, 220-228.

121. Rosenkrands, I., Slayden, R. A., Crawford, J., Aagaard, C., Barry, C. E., 3rd, and Andersen, P. (2002) Hypoxic response of Mycobacterium tuberculosis studied by metabolic labeling and proteome analysis of cellular and extracellular proteins, *J Bacteriol 184*, 3485-3491.

122. Rutter, W. J. (1964) Evolution of Aldolase, *Fed Proc 23*, 1248-1257.

123. Lorentzen, E., Siebers, B., Hensel, R., and Pohl, E. (2005) Mechanism of the Schiff base forming fructose-1,6-bisphosphate aldolase: structural analysis of reaction intermediates, *Biochemistry 44*, 4222-4229.

124. Zgiby, S., Plater, A. R., Bates, M. A., Thomson, G. J., and Berry, A. (2002) A functional role for a flexible loop containing Glu182 in the class II fructose-1,6-bisphosphate aldolase from Escherichia coli, *J Mol Biol 315*, 131-140.

125. Galkin, A., Kulakova, L., Melamud, E., Li, L., Wu, C., Mariano, P., Dunaway-Mariano, D., Nash, T. E., and Herzberg, O. (2007) Characterization, kinetics, and crystal structures of fructose-1,6-bisphosphate aldolase from the human parasite, Giardia lamblia, *J Biol Chem 282*, 4859-4867.

126. Izard, T., and Sygusch, J. (2004) Induced fit movements and metal cofactor selectivity of class II aldolases: structure of Thermus aquaticus fructose-1,6-bisphosphate aldolase, *J Biol Chem 279*, 11825-11833.

127. Marsh, J. J., and Lebherz, H. G. (1992) Fructose-bisphosphate aldolases: an evolutionary history, *Trends Biochem Sci 17*, 110-113.

128. Baba, T., Ara, T., Hasegawa, M., Takai, Y., Okumura, Y., Baba, M., Datsenko, K. A., Tomita, M., Wanner, B. L., and Mori, H. (2006) Construction of Escherichia coli K-12 in-frame, single-gene knockout mutants: the Keio collection, *Mol Syst Biol 2*, 2006 0008.

129. Giaever, G., Chu, A. M., Ni, L., Connelly, C., Riles, L., Veronneau, S., Dow, S., Lucau-Danila, A., Anderson, K., Andre, B., Arkin, A. P., Astromoff, A., El-Bakkoury, M., Bangham, R., Benito, R., Brachat, S., Campanaro, S., Curtiss, M., Davis, K., Deutschbauer, A., Entian, K. D., Flaherty, P., Foury, F., Garfinkel, D. J., Gerstein, M., Gotte, D., Guldener, U., Hegemann, J. H., Hempel, S., Herman,

Z., Jaramillo, D. F., Kelly, D. E., Kelly, S. L., Kotter, P., LaBonte, D., Lamb, D. C., Lan, N., Liang, H., Liao, H., Liu, L., Luo, C., Lussier, M., Mao, R., Menard, P., Ooi, S. L., Revuelta, J. L., Roberts, C. J., Rose, M., Ross-Macdonald, P., Scherens, B., Schimmack, G., Shafer, B., Shoemaker, D. D., Sookhai-Mahadeo, S., Storms, R. K., Strathern, J. N., Valle, G., Voet, M., Volckaert, G., Wang, C. Y., Ward, T. R., Wilhelmy, J., Winzeler, E. A., Yang, Y., Yen, G., Youngman, E., Yu, K., Bussey, H., Boeke, J. D., Snyder, M., Philippsen, P., Davis, R. W., and Johnston, M. (2002) Functional profiling of the Saccharomyces cerevisiae genome, *Nature 418*, 387-391.

130. Jacobs, M. A., Alwood, A., Thaipisuttikul, I., Spencer, D., Haugen, E., Ernst, S., Will, O., Kaul, R., Raymond, C., Levy, R., Chun-Rong, L., Guenthner, D., Bovee, D., Olson, M. V., and Manoil, C. (2003) Comprehensive transposon mutant library of Pseudomonas aeruginosa, *Proceedings of the National Academy of Sciences of the United States of America 100*, 14339-14344.

131. Kobayashi, K., Ehrlich, S. D., Albertini, A., Amati, G., Andersen, K. K., Arnaud, M., Asai, K., Ashikaga, S., Aymerich, S., Bessieres, P., Boland, F., Brignell, S. C., Bron, S., Bunai, K., Chapuis, J., Christiansen, L. C., Danchin, A., Debarbouille, M., Dervyn, E., Deuerling, E., Devine, K., Devine, S. K., Dreesen, O., Errington, J., Fillinger, S., Foster, S. J., Fujita, Y., Galizzi, A., Gardan, R., Eschevins, C., Fukushima, T., Haga, K., Harwood, C. R., Hecker, M., Hosoya, D., Hullo, M. F., Kakeshita, H., Karamata, D., Kasahara, Y., Kawamura, F., Koga, K., Koski, P., Kuwana, R., Imamura, D., Ishimaru, M., Ishikawa, S., Ishio, I., Le Coq, D., Masson, A., Mauel, C., Meima, R., Mellado, R. P., Moir, A., Moriya, S., Nagakawa, E., Nanamiya, H., Nakai, S., Nygaard, P., Ogura, M., Ohanan, T., O'Reilly, M., O'Rourke, M., Pragai, Z., Pooley, H. M., Rapoport, G., Rawlins, J. P., Rivas, L. A., Rivolta, C., Sadaie, A., Sadaie, Y., Sarvas, M., Sato, T., Saxild, H. H., Scanlan, E., Schumann, W., Seegers, J. F., Sekiguchi, J., Sekowska, A., Seror, S. J., Simon, M., Stragier, P., Studer, R., Takamatsu, H., Tanaka, T., Takeuchi, M., Thomaides, H. B., Vagner, V., van Dijl, J. M., Watabe, K., Wipat, A., Yamamoto, H., Yamamoto, M., Yamamoto, Y., Yamane, K., Yata, K., Yoshida, K., Yoshikawa, H., Zuber, U., and Ogasawara, N. (2003) Essential Bacillus subtilis genes, *Proceedings of the National Academy of Sciences of the United States of America 100*, 4678-4683.

132. Liberati, N. T., Urbach, J. M., Miyata, S., Lee, D. G., Drenkard, E., Wu, G., Villanueva, J., Wei, T., and Ausubel, F. M. (2006) An ordered, nonredundant library of Pseudomonas aeruginosa strain PA14 transposon insertion mutants, *Proceedings of the National Academy of Sciences of the United States of America 103*, 2833-2838.

133. Rodaki, A., Young, T., and Brown, A. J. (2006) Effects of depleting the essential central metabolic enzyme fructose-1,6-bisphosphate aldolase on the growth and

viability of Candida albicans: implications for antifungal drug target discovery, *Eukaryotic cell 5*, 1371-1377.

134. Sassetti, C. M., Boyd, D. H., and Rubin, E. J. (2003) Genes required for mycobacterial growth defined by high density mutagenesis, *Molecular microbiology 48*, 77-84.

135. Song, J. H., Ko, K. S., Lee, J. Y., Baek, J. Y., Oh, W. S., Yoon, H. S., Jeong, J. Y., and Chun, J. (2005) Identification of essential genes in Streptococcus pneumoniae by allelic replacement mutagenesis, *Molecules and cells 19*, 365-374.

136. Wehmeier, U. F. (2001) Molecular cloning, nucleotide sequence and structural analysis of the Streptomyces galbus DSM40480 fda gene: the S. galbus fructose-1,6-bisphosphate aldolase is a member of the class II aldolases, *FEMS microbiology letters 197*, 53-58.

137. Scamuffa, M. D., and Caprioli, R. M. (1980) Comparison of the mechanisms of two distinct aldolases from Escherichia coli grown on gluconeogenic substrates, *Biochim Biophys Acta 614*, 583-590.

138. Stribling, D., and Perham, R. N. (1973) Purification and characterization of two fructose diphosphate aldolases from Escherichia coli (Crookes' strain), *Biochem J 131*, 833-841.

139. Collins, K. D. (1974) An activated intermediate analogue. The use of phosphoglycolohydroxamate as a stable analogue of a transiently occurring dihydroxyacetone phosphate-derived enolate in enzymatic catalysis, *J Biol Chem 249*, 136-142.

140. Dreyer, M. K., and Schulz, G. E. (1996) Catalytic mechanism of the metal-dependent fuculose aldolase from Escherichia coli as derived from the structure, *J Mol Biol 259*, 458-466.

141. Gavalda, S., Braga, R., Dax, C., Vigroux, A., and Blonski, C. (2005) N-Sulfonyl hydroxamate derivatives as inhibitors of class II fructose-1,6-diphosphate aldolase, *Bioorg Med Chem Lett 15*, 5375-5377.

142. Kitagawa, M., Ara, T., Arifuzzaman, M., Ioka-Nakamichi, T., Inamoto, E., Toyonaga, H., and Mori, H. (2005) Complete set of ORF clones of Escherichia coli ASKA library (a complete set of E. coli K-12 ORF archive): unique resources for biological research, *DNA research : an international journal for rapid publication of reports on genes and genomes 12*, 291-299.

143. Martin, A., Camacho, M., Portaels, F., and Palomino, J. C. (2003) Resazurin microtiter assay plate testing of Mycobacterium tuberculosis susceptibilities to

second-line drugs: rapid, simple, and inexpensive method, *Antimicrobial agents and chemotherapy 47*, 3616-3619.

144. Sali, A., and Blundell, T. L. (1993) Comparative Protein Modeling by Satisfaction of Spatial Restraints, *J Mol Biol 234*, 779-815.

145. Agrawal, A., Johnson, S. L., Jacobsen, J. A., Miller, M. T., Chen, L. H., Pellecchia, M., and Cohen, S. M. (2010) Chelator fragment libraries for targeting metalloproteinases, *ChemMedChem 5*, 195-199.

146. Agrawal, A., Romero-Perez, D., Jacobsen, J. A., Villarreal, F. J., and Cohen, S. M. (2008) Zinc-binding groups modulate selective inhibition of MMPs, *ChemMedChem 3*, 812-820.

147. Jacobsen, J. A., Fullagar, J. L., Miller, M. T., and Cohen, S. M. (2011) Identifying chelators for metalloprotein inhibitors using a fragment-based approach, *Journal of medicinal chemistry 54*, 591-602.

148. Puerta, D. T., Griffin, M. O., Lewis, J. A., Romero-Perez, D., Garcia, R., Villarreal, F. J., and Cohen, S. M. (2006) Heterocyclic zinc-binding groups for use in next-generation matrix metalloproteinase inhibitors: potency, toxicity, and reactivity, *Journal of biological inorganic chemistry : JBIC : a publication of the Society of Biological Inorganic Chemistry 11*, 131-138.

149. Puerta, D. T., Lewis, J. A., and Cohen, S. M. (2004) New beginnings for matrix metalloproteinase inhibitors: identification of high-affinity zinc-binding groups, *Journal of the American Chemical Society 126*, 8388-8389.

150. Rouffet, M., de Oliveira, C. A., Udi, Y., Agrawal, A., Sagi, I., McCammon, J. A., and Cohen, S. M. (2010) From sensors to silencers: quinoline- and benzimidazole-sulfonamides as inhibitors for zinc proteases, *Journal of the American Chemical Society 132*, 8232-8233.

151. Feng, B. Y., and Shoichet, B. K. (2006) A detergent-based assay for the detection of promiscuous inhibitors, *Nat Protoc 1*, 550-553.

152. Lipinski, C. A., Lombardo, F., Dominy, B. W., and Feeney, P. J. (2001) Experimental and computational approaches to estimate solubility and permeability in drug discovery and development settings, *Advanced Drug Delivery Reviews 46*, 3-26.

153. McDonald, F. C., Applefield, R. C., Halkides, C. J., Reibenspies, J. H., and Hancock, R. D. (2008) A thermodynamic and crystallographic study of complexes of the highly preorganized ligand 8-hydroxyquinoline-2-carboxylic acid, *Inorg Chim Acta 361*, 1937-1946.

154. Sobke, A., Klinger, M., Hermann, B., Sachse, S., Nietzsche, S., Makarewicz, O., Keller, P. M., Pfister, W., and Straube, E. (2012) The urinary antibiotic 5-nitro-8-hydroxyquinoline (Nitroxoline) reduces the formation and induces the dispersal of Pseudomonas aeruginosa biofilms by chelation of iron and zinc, *Antimicrobial agents and chemotherapy 56*, 6021-6025.

155. Ohren, J. F., Chen, H., Pavlovsky, A., Whitehead, C., Zhang, E., Kuffa, P., Yan, C., McConnell, P., Spessard, C., Banotai, C., Mueller, W. T., Delaney, A., Omer, C., Sebolt-Leopold, J., Dudley, D. T., Leung, I. K., Flamme, C., Warmus, J., Kaufman, M., Barrett, S., Tecle, H., and Hasemann, C. A. (2004) Structures of human MAP kinase kinase 1 (MEK1) and MEK2 describe novel noncompetitive kinase inhibition, *Nature structural & molecular biology 11*, 1192-1197.

156. Segel, I. H. (Enzyme kinetics: Behavior and analysis of rapid equilibrium and steady state enzyme systems) *1975*, Wiley, New York.

157. Lehninger, A. L., Nelson, D. L., and Cox, M. M. (2008) *Lehninger principles of biochemistry*, 5th ed., W.H. Freeman, New York.

158. Rees, D. C., Congreve, M., Murray, C. W., and Carr, R. (2004) Fragment-based lead discovery, *Nature reviews. Drug discovery 3*, 660-672.

159. Veber, D. F., Johnson, S. R., Cheng, H. Y., Smith, B. R., Ward, K. W., and Kopple, K. D. (2002) Molecular properties that influence the oral bioavailability of drug candidates, *Journal of medicinal chemistry 45*, 2615-2623.